Politecnico di Torino

&

KTH Royal Institute of Technology

Double Master's Degree in Energy and Nuclear Engineering
Track: Design and Management of Energy Systems

March 2024

Thermal modelling for ITER First Wall Heat Load Control

Supervisors:

Ing. Giuseppe Francesco Nallo (Polito)
Salvatore Guccione (KTH)
Federico Pesamosca (ITER)

Candidate:

Mattia Erroi

To my parents,
my pillar and reference point.

Abstract

The International Thermonuclear Experimental Reactor (ITER) plays a pivotal role in energy fusion research based on tokamak technology and will magnetically confine a hot toroidal plasma, whose heat exhausted will impact the internal surface of the tokamak chamber closest to the plasma itself, namely the First Wall (FW), potentially leading to accidental conditions. The FW will be protected in real-time (RT) by the First Wall Heat Load Controller (FWHLC), which evaluates its surface temperature through a combination of measurements from infrared (IR) cameras and reconstruction of the impacting heat load thanks to the coupling with a thermal model, which is the focus of this thesis.

This work has been at the center of a research and development process as ITER is presently undergoing a re-baseline involving a series of proposals, including the installation of inertially cooled First Wall Panels (FWPs) in an early operation phase called Augmented First Plasma (AFP). Thermal models present in the literature lack the necessary flexibility to cope with the FW design evolution imposed by the re-baseline. Moreover, the literature lacks a systematic approach to identify a trade-off between accuracy and running time requirements for RT applications. Finally, no FW temperature map data are presently available in the ITER database, which are needed for the planned development of IR cameras' synthetic diagnostics. In light of these research gaps, this work aims first at finding the most suitable thermal model for the FWHLC in the AFP phase in terms of a trade-off between accuracy and running time requirements for RT response, secondly analysing the thermal response of the FW in the AFP phase, and thirdly finding a simple yet reliable thermal model for IR cameras' synthetic diagnostics.

The first two aims have been fulfilled by developing a control-oriented model kept flexible enough to adapt to evolving FW geometries and either active or inertial cooling. Numerical heat transfer simulations have been carried out in MATLAB with a focus on individual fingers composing FWPs. Simulations included fingers' 1D and 2D models, considering both constant and temperature-dependent properties. A comparative assessment between these simulations allowed to find models at the same time simple and accurate. Additionally, 2D models have been validated against higher fidelity simulations to test their accuracy. The comparative assessment has shown that a 1D model is suitable for actively cooled FWPs while, in the case of inertially cooled panels, a 2D model is recommended. Also, the assumption of constant thermal properties for the temperature range of interest has been verified. Furthermore, a convergence analysis has been carried out to find time steps and computational grid sizes suitable for RT applications. Finally, realistic heat load data coming from simulations including plasma dynamics have been employed to investigate FW thermal response time scales essential for the controller design, which resulted in the order of seconds. The third aim has been fulfilled by developing a simple steady-state 1D model for actively cooled FWPs. The problem allows an analytical solution, which also considers the volumetric heat generated by neutrons produced by fusion reactions. Results show that for most of the FWPs the expected surface temperature is lower than IR cameras' lower detection threshold and that volumetric heat generation is negligible.

Keywords

Nuclear fusion, ITER, first wall, heat load real-time control, control-oriented modeling, numerical heat transfer, thermal modelling, infrared cameras' synthetic diagnostics

Sammanfattning

Den International Thermonuclear Experimental Reactor (ITER) spelar en central roll inom energifusionsforskning på tokamak-teknologin och kommer magnetiskt att begränsa ett varmt toroidplasma, vars värme som förbrukas kommer att påverka inre yta av tokamakammaren närmast själva plasman, nämligen First Wall (FW), vilket potentiellt leder till oavsiktliga förhållanden. FW kommer att skyddas i real-time (RT) av First Wall Heat Load Controller (FWHLC), som utvärderar dess yttemperatur genom en kombination av mätningar från infraröda (IR) kameror och rekonstruktion av den påverkande värmebelastningen tack vare kopplingen med en termisk modell, som är fokus för denna avhandling.

Detta arbete har stått i centrum för en forsknings- och utvecklingsprocess eftersom ITER för närvarande genomgår en ny baslinje involverar en rad förslag, inklusive installation av tröghetskylda First Wall Panels (FWP) i en tidig driftfas som kallas Augmented First Plasma (AFP). Termiska modeller som finns i litteraturen saknar det nödvändiga flexibilitet för att klara av FW-designutvecklingen som påtvingas av re-baseline. Dessutom saknar litteraturen en systematisk metod för att identifiera en kompromiss mellan krav på noggrannhet och drifttid för RT-applikationer. Slutligen, ingen FW temperaturkartdata finns för närvarande tillgängliga i ITER-databasen, som behövs för den planerade utvecklingen av IR-kameror syntetisk diagnostik. Mot bakgrund av dessa forskningsluckor syftar detta arbete först till att hitta den mest lämpliga termisk modell för FWHLC i AFP-fasen i termer av avvägning mellan noggrannhet och körtidskrav för RT-svar, för det andra att analysera det termiska svaret av FW i AFP-fasen, och för det tredje hitta en enkel ändå pålitlig termisk modell för IR-kameror syntetisk diagnostik.

De två första målen har uppfyllts genom att utveckla en kontrollorienterad modell som hålls tillräckligt flexibel för att anpassa sig till utvecklingen FW-geometrier och antingen aktiv eller tröghetskylning. Numeriska värmeöverförings-simuleringar har genomförts i MATLAB med fokus på enskilda fingrar som komponerar FWP. Simuleringarna inkluderade fingrarnas 1D- och 2D-modeller, med hänsyn till både konstanta och temperaturberoende egenskaper. En jämförande bedömning mellan dessa simuleringar tillåts hitta modeller på samma gång enkelt och korrekt. Dessutom har 2D-modeller validerats mot simuleringar med högre kvalitet för att testa deras noggrannhet. Den jämförande bedömningen har visat att en 1D-modell är lämplig för aktivt kylda FWP:er medan, för tröghetskylda paneler, en 2D-modell rekommenderas. Också antagandet konstanta termiska egenskaper för temperaturområdet av intresse har verifierats. Dessutom en konvergens analys har utförts för att hitta tidssteg och beräkningsnätstorlekar som är lämpliga för RT-tillämpningar. Till sist, realistiska värmebelastningsdata från simuleringar inklusive plasmadynamik har använts för att undersöka FW termiska svarstidsskalor som är viktiga för styrenhetens design, vilket resulterade i storleksordningen sekunder. Den tredje Målet har uppfyllts genom att utveckla en enkel steady-state 1D-modell för aktivt kylda FWP. Problemet tillåter en analytisk lösning, som också tar hänsyn till den volymetriska värmen som genereras av neutroner som produceras av fusionsreaktioner. Resultaten visar att för de flesta FWP:er är den förväntade yttemperaturen lägre än IR-kameror lägre detektion tröskeln och att volymetrisk värmealstring är försumbar.

Nyckelord

Kärnfusion, ITER, första vägg, värmebelastning i realtid, kontrollorienterad modellering, numerisk värmeöverföring, termisk modellering, infraröda kameror syntetisk diagnostik

Acknowledgements

I would like to express my gratitude to Federico Pesamosca, my supervisor at ITER Organization, for the great opportunity to join ITER and for the freedom and trust he expressed in my regard during this project. His constant support and guidance allowed me to carry out this work consistently, smoothly, and with high scientific accuracy.

I would also like to express my gratitude to my university supervisors, Salvatore Guccione on the KTH side and Ing. Giuseppe Francesco Nallo on the PoliTo side, for their insightful and remarkably valuable support throughout this work. Their precious pieces of advice allowed me to successfully structure this work from an academic standpoint and combine scientific accuracy and communicative effectiveness.

I am grateful to Matic Brank, and to Quentin Deliege and Lei Chen of ITER Blanket section, whose simulations and data were essential for this work.

I am grateful and honored to have met the scientists belonging to the ITER Experiments and Plasma Operation section, in particular Richard Pitts, Timo Ravensbergen, Luca Zabeo, and Sunwoo Moon, who contributed to this work through their valuable suggestions.

This thesis constitutes the culmination and final point of an entire journey, fundamental for my professional and personal development. Therefore, may I be permitted to briefly interrupt the rigorously scientific aspect of this work to genuinely express my thoughts about this experience. I remember extremely well the day I left my beloved Lecce and set foot for the first time on the "legendary" Lecce-Turin train to start my studies in Turin. At that time, I was a very young boy, full of dreams, ambitions, and fears. If I could go back in time and talk to that young boy, he would probably not believe me if I told him what he would have experienced. I would have never believed that, despite countless difficulties and several challenging moments, I could undertake a path so full of satisfaction, a path that allowed me, in just over two years, to live in three different countries, Italy, Sweden, and France, contributing not only to discovering different cultures but above all to discovering myself. One of the most important lessons I can draw from this wonderful journey is the importance of believing in oneself, never underestimating oneself, and facing with bravery and determination the various challenges life presents us, always bearing in mind that, quoting Seneca, *multa non quia non audemus difficilia sunt, sed quia non audemus sunt difficilia.*

This wonderful journey would not have been possible without the people I was lucky enough to meet, who offered authentic support and unforgettable memories, and from whom I learned so much. I would particularly like to thank my long-standing friends from Lecce, Giorgio, Gigi, and Luca, whose long and authentic friendship seems, quite magically to me, to never change. I also thank my friends from Turin, in particular Malik, and the guys of the "2° floor A4" of the "residenza Borsellino" I shared several nice moments with, especially Mattia, Simone, Patrick, Roberto, Federica, and Virginia. I would also like to thank my colleagues at Politecnico di Torino, with whom I shared challenges but also several joyful moments, in particular Roberto, Enrico, and above all Aldo, a true and special friend. I would also like to thank the people I was lucky enough to meet in Stockholm, in particular Vittoria, a precious friend and great source of inspiration, Giacomo, a true friend and Swedish adventures fellow, and Simone, with whom I was lucky enough to share one of the most adventurous experiences of my life such as trekking in Kungsleden. I also thank the "Wander Buddys", in particular Loïc and Peter, with whom I had the pleasure of sharing another wonderful experience such as the trip to the cold Kiruna in northern Sweden. Thanks also to Alice and Anthony, whom I hope to maintain a lasting friendship with, and Salvatore, who besides being the supervisor of this thesis, is also a friend and a source of inspiration from a personal and professional point of view. I would also like to thank those I had the pleasure of discovering France and sharing nice moments with, in particular Lisa, Francesco, Eleonora, Sofia, Henri, Beppe, Salvatore, Michele, Martín, and Tom. Finally, I would like to thank the Italian State and the Erasmus+ program for giving me the opportunity to study and financially supporting my international experiences in Sweden and France.

The most important acknowledgments go to my family, for their unconditional love towards me, in particular to my aunt Emanuela, my sister Sofia, my grandmother Rosetta who unfortunately I can no longer hug, and above all to my parents. Mom and Dad, you are my pillar and my point of reference, my greatest strength. It's almost impossible to put into words the love I feel for you. Mom, thank you for all the teachings you gave me but especially thanks for teaching me the values of humility, the spirit of sacrifice, honesty, loyalty, and perseverance. Dad, thank you for all the teachings you gave me, but thanks especially for constituting for me the example of the man I want to be, a humble, curious, assertive, honest, calm, dependable, and respectful man like you. I am proud to be your son.

Ringraziamenti

Vorrei esprimere la mia gratitudine a Federico Pesamosca, il mio supervisore presso ITER Organization, per la grande opportunità di entrare a far parte di ITER e per la libertà e la fiducia che mi ha concesso durante lo svolgimento di questo progetto. Il suo costante supporto e la sua guida mi hanno permesso di svolgere questo lavoro in modo costante, senza ostacoli e con elevata accuratezza scientifica.

Vorrei anche esprimere la mia gratitudine ai miei supervisori universitari, Salvatore Guccione lato KTH e all'Ing. Giuseppe Francesco Nallo lato PoliTo, per il loro supporto sagace e straordinariamente prezioso. I loro consigli mi hanno permesso di strutturare con successo questo lavoro dal punto di vista accademico e di coniugare rigore scientifico ed efficacia comunicativa.

Sono grato a Matic Brank, e a Quentin Deliege e Lei Chen della sezione ITER Blanket, le cui simulazioni e dati sono stati essenziali per questo lavoro.

Sono grato e onorato di aver incontrato gli scienziati appartenenti alla sezione ITER Experiments and Plasma Operation, in particolare Richard Pitts, Timo Ravensbergen, Luca Zabeo e Sunwoo Moon, che hanno contribuito a questo lavoro attraverso i loro preziosi suggerimenti.

Questa tesi costituisce il culmine e il punto finale di un intero percorso, fondamentale per il mio sviluppo professionale e personale. Mi sia quindi concesso di interrompere brevemente il carattere rigorosamente scientifico di questa tesi per esprimere sinceramente i miei pensieri riguardo a questa esperienza. Ricordo estremamente bene il giorno in cui lasciai la mia amata terra e misi piede per la prima volta sul "leggendario" treno Lecce-Torino per avviare i miei studi. All'epoca, ero un ragazzo giovanissimo, pieno di sogni, ambizioni e paure. Se potessi tornare indietro nel tempo e parlare con quel giovane ragazzo, penso non mi crederebbe se gli raccontassi ciò che lo avrebbe aspettato. Non avrei mai creduto di poter essere in grado, nonostante innumerevoli difficoltà e numerosi momenti difficili, di intraprendere un percorso così ricco di soddisfazioni, un percorso che mi ha consentito, in poco più di due anni, di vivere in tre paesi diversi, Italia, Svezia e Francia, contribuendo non soltanto alla scoperta di culture diverse, ma soprattutto alla scoperta di me stesso. Una delle lezioni più importanti che posso trarre da questo meraviglioso viaggio è l'importanza di credere in sé stessi, non sottovalutarsi mai, e affrontare con coraggio e determinazione le varie sfide che la vita ci pone davanti, tenendo sempre a mente che, citando Seneca, *multa non quia non audemus difficilia sunt, sed quia non audemus sunt difficilia*.

Questo meraviglioso viaggio non sarebbe stato possibile senza le persone che ho avuto la fortuna di incontrare, le quali hanno offerto autentico supporto e momenti indimenticabili di condivisione, e dalle quali ho imparato tanto. Desidero in particolare ringraziare i miei amici di sempre di Lecce, Giorgio, Gigi e Luca, la cui lunga e autentica amicizia sembra, quasi magicamente ai miei occhi, non cambiare mai. Ringrazio anche i miei amici di Torino, in particolare Malik, e i ragazzi del "2° piano A4" della residenza Borsellino, specialmente Mattia, Simone, Patrick, Roberto, Federica e Virginia, con i quali ho condiviso numerosi momenti di risate e spensieratezza. Vorrei anche ringraziare i miei colleghi del Politecnico di Torino, con i quali ho condiviso sfide ma anche momenti di gioia, in particolare Roberto, Enrico e soprattutto Aldo, un amico vero e speciale. Vorrei inoltre ringraziare le persone che ho avuto la fortuna di conoscere a Stoccolma, in particolare Vittoria, un'amica preziosa e grande fonte di ispirazione, Giacomo, autentico amico e compagno di avventure svedesi, e Simone, con il quale ho avuto la fortuna di condividere una delle esperienze più avventurose della mia vita quale il Kungsleden. Ringrazio anche i "Wander Buddys", in particolare Loïc e Peter, con i quali ho avuto il piacere di condividere un'altra esperienza meravigliosa quale la gita nel nord della Svezia nella fredda Kiruna. Grazie anche ad Alice ed Anthony, con i quali spero di mantenere un'amicizia duratura e Salvatore, che oltre ad essere il supervisore di questa tesi, è anche un amico e una fonte di ispirazione dal punto di vista personale e professionale. Desidero anche ringraziare coloro con i quali ho avuto il piacere di scoprire la Francia e condividere momenti di risate e spensieratezza, in particolare Lisa, Francesco, Eleonora, Sofia, Henri, Beppe, Salvatore, Michele,

Martín e Tom. Infine, vorrei ringraziare lo Stato italiano e il programma Erasmus+ per avermi dato la possibilità di studiare e di sostenere finanziariamente le mie esperienze internazionali in Svezia e Francia.

Il ringraziamento più importante va alla mia famiglia, per il loro amore incondizionato nei miei confronti, in particolare a mia zia Emanuela, a mia sorella Sofia, a mia nonna Rosetta che purtroppo non posso più abbracciare e soprattutto ai miei genitori. Mamma, papà, voi siete il mio pilastro e il mio punto di riferimento, la mia forza più grande. È quasi impossibile esprimere a parole l'amore che provo nei vostri confronti. Mamma, grazie per tutti gli insegnamenti che mi hai dato, ma grazie soprattutto per avermi insegnato i valori di umiltà, spirito di sacrificio, onestà, lealtà e perseveranza. Papà, grazie per tutti gli insegnamenti che mi hai dato, ma grazie soprattutto per costituire per me l'esempio dell'uomo che voglio essere, un uomo umile, curioso, assertivo, onesto, calmo, affidabile e rispettoso come te. Sono orgoglioso di essere vostro figlio.

Contents

List of Figures

List of Tables

List of Abbreviations

ADI	Alternating Direction Implicit
AFP	Augmented First Plasma
BE	Backwards Euler
BM	Blanket Module
CCUS	Carbon Capture, Utilization and Storage
CV	Control Volume
EHF	Enhanced Heat Flux
ELM	Edge Localized Modes
EPO	Experiments and Plasma Operation Section
FC	Frozen Coefficient
FE	Forward Euler
FEM	Finite Element Method
FV	Finite Volumes
FW	First Wall
FWHLC	First Wall Heat Load Controller
FWP	First Wall Panels
HFS	High-Field Side
HTC	Heat Transfer Coefficient
HTS	High-Temperature Superconductors
ICF	Inertial Confinement Fusion
ITER	International Thermonuclear Experimental Reactor
JET	Joint European Torus
LFS	Low-Field Side
LTS	Low-Temperature Superconductors
MCF	Magnetic Confinement Fusion
NHF	Normal Heat Flux
ODE	Ordinary Differential Equation
PCS	Plasma Control System

PCSSP	Plasma Control System Simulation Platform
PDE	Partial Differential Equation
PFC	Plasma Facing Component
POD	the Proper Orthogonal Decomposition (POD) method
RT	Real Time
SB	Shield Block
SCD	Science Division
SCOD	Controls and Operation Department
SOL	Scrape-off Layer
TFW	Temporary First Wall
VDE	Vertical Displacement Event

Chapter 1

Introduction

While this thesis is being written, climate change is a major concern for humanity. Consequences of climate change such as wildfires, droughts, floods, and sea-level rise are clearly evident and are seriously threatening the existing ecosystems, besides undermining the socio-economic human structures [European Commission, n.d.]. Climate change is caused by greenhouse gases, especially carbon dioxide, mainly emitted by burning fossil fuels (coal, oil, and natural gas), responsible for 75% of global greenhouse gas emissions [United Nations, n.d.]. Despite this, as depicted in figure 1.1, not only humanity has largely relied on fossil fuels consumption in recent history, but still today fossil fuels dominate with nearly 77% of total primary energy consumption. Therefore, the urgency of the climate crisis requires a rapid "energy transition" towards carbon-free energy sources. On top of that, the combination of the expected increase in world energy demand and the limited available fossil fuel resources on Earth may cause an energy shortfall in the coming decades at the present rate of fossil fuels consumption [Lee and Saw, 2011]. As depicted in figure 1.2, the direct consequence is the need for abundant energy sources alternative to fossil fuels. Another important point is the need for energy security, namely the "uninterrupted availability of energy sources at an affordable price", related both to long-term and short-term energy supply, with the latter dealing with "timely investments to supply energy in line with economic developments and environmental needs" and the former with "the ability of the energy system to react promptly to sudden changes in the supply-demand balance" [IEA, n.d.b]. From the standpoint of long-term energy security, being particularly concentrated in specific areas in the world, fossil fuels often represented and still today represent a source of geopolitical tensions and conflicts, undermining their continuous availability. It would be hypocritical not to mention that fossil fuels have been a key to the development of human societies, resulting in the present social and economic wealth that characterizes most of the countries in the world. Nevertheless, in light of the above, humanity needs alternative energy sources to fossil fuels, in particular having the following characteristics: carbon-free, abundant, and secure.

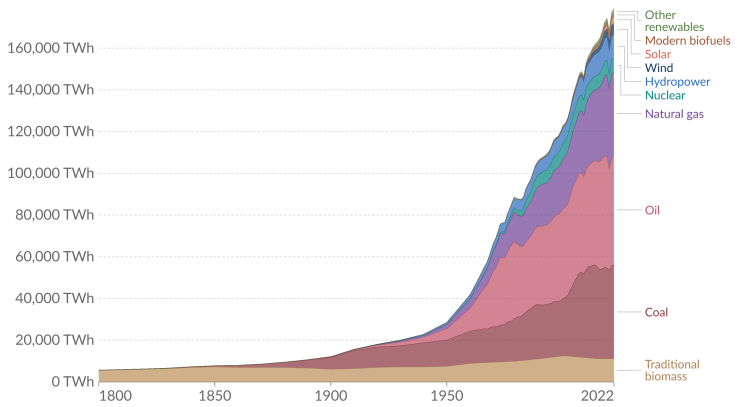

Figure 1.1: Global primary energy consumption by source measured in TWh [Ritchie et al., 2020].

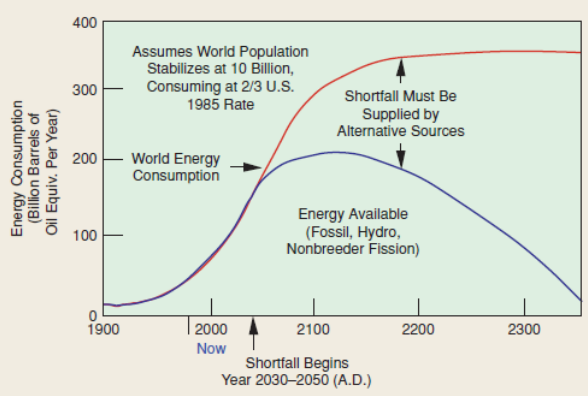

Figure 1.2: Projected energy shortfall [Ritchie et al., 2020]. As the beginning of the shortfall may considerably vary because of significant uncertainty both on the future energy demand and on fossil fuels reserves, this chart is meant to be qualitative.

In this venture of finding alternative energy sources, some suitable candidates are: fossil fuels combined with carbon capture, utilization and storage (CCUS); renewable energy sources; nuclear fission; nuclear fusion. CCUS consists of capturing carbon dioxide mainly from quite large facilities such as power plants or industries, utilizing it in industrial processes and/or storing it typically in geological reservoirs [IEA, n.d.a]. CCUS is currently under development, representing a valid alternative for the energy transition, particularly in hard-to-abate sectors, like heavy industry and chemicals, besides possibly offsetting unavoidable emissions from sectors like transportation and agriculture [Dziejarski et al., 2023]. However, despite being a possible short-term answer to the climate crisis when combined with CCUS, fossil fuels do not represent a long-term energy solution because of their inherent limited abundance. Renewable energy sources like solar, wind, hydro, geothermal, and bioenergy are carbon-free, abundant, and long-term secure. However, renewable energies have insufficient energy density to cope with the entire global energy demand alone [Pironti and Walker, 2005], therefore an excessive increase in renewables penetration may cause environmental issues related to land use, such as threatening food security and biodiversity conservation [Capellán-Pérez et al., 2017]. Furthermore, some renewable energy sources like solar and wind are non-dispatchable, i.e., are intrinsically intermittent, posing a problem of energy security in the short-term, therefore they need to be complemented with frequency reserves and energy storage. Nuclear fission is based on fission reactions, which involve the splitting of nuclei with high atomic numbers. Nuclear fission reactors constitute a mature technology and have the advantage of assuring a carbon-free and secure energy supply. On the other hand, due to large up-front costs, severe safety requirements, and high-level waste management, nuclear fission often lacks public acceptance and competitiveness with other technologies [IEA, n.d.c]. Additionally, the risk of proliferation further exacerbates public acceptance. Nuclear fusion is instead based on fusion reactions, which involve the merging of nuclei with low atomic numbers. Unlike fission, nuclear fusion is currently in an early stage of development, and has many advantages:

- carbon-free. The most promising fusion reaction, namely the one having deuterium (D) and tritium (T) as reactants, has a neutron and helium as by-products, the latter being an inert and non-toxic gas. No greenhouse gases are produced [ITER Organization, n.d.a]
- abundant. As fusion reactions release tremendous amounts of energy, fuel consumption is relatively small. Deuterium can be extracted from water at a very low cost while tritium, despite not being present in nature because of its relatively short half-life of just 12.3 years, can be produced from nuclear reactions involving lithium. Reserves of lithium on Earth are enough to produce energy for 1000 years from fusion reactors [ITER Organization, n.d.a]
- secure (long-term). Deuterium and tritium are so abundant and cheap to ensure a reduced energy dependency [Ongena, 2016]
- high energy density. In terms of land requirements, fusion power plants are expected to be of the same order of magnitude as conventional power plants such as thermoelectric plants ($20 - 1000$ m^2/MW), contrarily to renewable power plants' quite large land requirements ($4000 - 90,000$ m^2/MW) [Schleisner et al., 2001]
- inherent safety. Unlike fission, fusion does not involve neutron chain reaction: the main safety issue for a nuclear fission reaction. i.e. core meltdown, can not physically happen. In case of undesired and unpredicted disturbances, a fusion reactor can be safely stopped within seconds [ITER Organization, n.d.a]

- absence of high-level waste. Fusion reactors will produce more waste than fission reactors, but low-level and intermediate-level waste, thus avoiding the need for long-term radioactive waste storage. The level of radioactivity is foreseen to drop significantly in 100 years time [De Vicente et al., 2022]

- limited risks of proliferation. Fusion does not involve the direct production of materials that could be employed to produce nuclear weapons [ITER Organization, n.d.a].

Nuclear fusion has obviously some drawbacks, including scientific complexity, engineering challenges, and economic competitiveness with other energy sources [Freidberg, 2008]. Scientific complexity is linked to the astonishing high temperatures required for fusion to happen, i.e., 150 million K for a deuterium-tritium (D-T) reaction, 10 times hotter than the core of the sun. The temperature is so high that deuterium and tritium become a fully ionized gas, namely a plasma, whose macroscopic fluid behavior is characterized by complex nonlinear dynamics. Moreover, in order to have fusion reactions, a sufficient amount of charged particles has to be held together for a sufficient time, i.e., the plasma must be confined. As a consequence, the requirement of maintaining a desired quantity of plasma sufficiently hot and confined makes fusion extremely challenging from a scientific standpoint. Engineering challenges range from developing suitable materials to withstand neutron and heat loads, realizing efficient heating systems to reach such extremely high temperatures, ensuring effective confinement, and also producing and managing tritium. Economic competitiveness is linked to the inherent complexity of nuclear fusion power plants, resulting in large up-front costs. Today it is quite hard to predict whether fusion reactors will be able to compete with other energy sources in the future energy mix, given nuclear fusion's early stage of development. However, focusing on electricity generation, in the context of a significant future renewable penetration in the energy mix, as can be expected given the current trend of increasing renewable generation, fusion reactors could benefit from the premiums deriving from reliable and steady electricity generation [Kembleton, 2023]. Indeed, fusion reactors can be designed to provide a constant power supply acting as base load, reducing the need for frequency reserves and storage. Additionally, fusion reactors could provide also thermal energy, which could be useful for district heating, desalination, and other industrial processes. Therefore, if the challenges mentioned are overcome, nuclear fusion represents an outstanding alternative energy source, with fusion reactors capable of providing carbon-free, abundant, secure, high-density, and safe energy supply, thus being integrated as base-load generation in the energy mix in combination with renewables.

Nuclear fusion research is fundamentally categorized into magnetic confinement and inertial confinement, with the former being more promising for base-load electricity generation [Lerede et al., 2023]. Currently, there are ongoing projects on various configurations but research is mainly focused on machines named tokamaks [Lee and Saw, 2011]. In this context, the International Thermonuclear Experimental Reactor (ITER) plays a pivotal role. ITER is an international project located in the south of France involving 35 countries including the US, South Korea, Russia, Japan, India, the European Union, and China and it will be the largest tokamak on Earth [ITER Organization, n.d.c]. Its primary aim is obtaining an energy gain of $Q = 10$, meaning that the output power from fusion needs to be at least ten times more than the input power absorbed by the plasma. Indeed, ITER will be equipped with 50 MW of auxiliary heating to produce 500 MW from fusion reactions, and it will not produce electricity. Basically, ITER constitutes the bridge between small experimental reactors and demonstration fusion power reactors such as DEMO [Federici et al., 2019], therefore paving the way for the commercialization of fusion energy, expected in the second half of the present century [Lerede et al., 2023]. ITER will also integrate and test components and technologies which will be used in future fusion reactors.

At the time of this thesis finalization, there is an ongoing re-baseline process at ITER [Loarte A., 2023]. For the scope of this thesis, the two main takeaways are the new proposed first wall (FW) material and the new ITER operation plan. According to the original ITER design, the FW material was beryllium while, according to the re-baseline, the new proposal is tungsten. Tungsten, with respect to beryllium, has a higher melting point and lower surface erosion [Pitts R., 2024]. On top of that, not only beryllium is toxic thus posing some issues from the operation and licensing standpoint, but has also the issue of trapping the tritium fuel in the case of erosion. On the other hand, tungsten dissipates more plasma energy, therefore lower plasma contamination can be tolerated. Concerning ITER research plan, with the re-baseline it is currently envisaged to divide ITER operation into three main phases:

- Augmented First Plasma (AFP): during this phase, the machine is operated at low-risk conditions, allowing the commissioning of the necessary systems. It is envisaged to employ non-active cooling of the FW, namely inertial cooling. Inertial cooling is a novelty, as before the re-baseline it has always been assumed to use active cooling

- DT-1: in this phase, the FW is actively cooled and additional heating power is installed

- DT-2: in this phase, ITER reaches "its final configuration in terms of tokamak components and auxiliary systems. The objective will then be to produce long-lived plasmas" [Loarte A., 2023]

The work presented herein is carried out in collaboration with ITER Organization, in particular within Controls and Operation Department (SCOD), Science Division (SCD), Experiments and Plasma Operation Section (EPO). Some of the works cited in this thesis constitute an ITER internal documentation which, as such, is not publicly accessible.

1.1 Motivation of the study

Due to transport in tokamak plasma, charged particles and fusion-generated neutrons continuously escape the magnetic confinement, eventually interacting with plasma-facing components (PFCs) with the generation of heat and particle fluxes [Freidberg, 2008]. For this reason, ITER is equipped with a divertor, a PFC having the specific aim of managing most of the heat exhausted from the plasma in steady-state conditions, resulting in approximately 10 MW/m^2, comparable to a taking-off rocket [Pitts et al., 2011]. Consequently, the rest of PFCs, namely the FW, receive relatively low thermal fluxes in steady-state conditions [ITER Organization, n.d.b]. However, during nominal and off-nominal transient events, the FW can receive heat fluxes exceeding the steady-state limit and be subjected to a great amount of deposited energy [Mitteau et al., 2010]. That being the case, a first line of defense is given by the First Wall Heat Load Controller (FWHLC) whose role is to avoid the development of undesired heat fluxes on the FW by acting in feedback on the plasma [Ravensbergen et al., 2023]. The FWHLC, which is part of the broader Plasma Control System (PCS) and currently under development at ITER, will be designed following a model-based approach, involving a plasma model, a thermal model, a series of actuators, and finally several synthetic diagnostics, the main one being infrared (IR) cameras [Pesamosca et al., 2023]. In particular, this work is focused on the thermal model for ITER FW, whose objective is evaluating the surface temperature evolution of the PFCs impacted by the heat flux dictated by the plasma equilibrium and power balance, considering the wall geometry. This model has three main applications which will dictate the requirements for its development:

- model-based control design, i.e., modelling the FW thermal dynamics during the controller design phase to correctly include the characteristic time for heat diffusion
- active control, i.e., allowing real-time (RT) simulations of the temperature evolution in the PFCs to enable predictive control when combined with IR camera measurements
- development of IR cameras' synthetic diagnostics, i.e., benchmarking the surface temperature distribution computed through the thermal model with the values measured by IR cameras

In this framework, several thermal models of the FW or, more generally, of PFCs, are available in the literature, both for control and design purposes. In fusion research, the reference thermal model is the RACLETTE code [Raffray and Federici, 1997], a relatively simple but thorough 1D transient heat transfer model developed for actively cooled plasma plasma-facing components (PFCs) simulating various key heat transfer phenomena occurring on their surface including evaporation, melting, and radiation. That being the case, the RACLETTE code is particularly suitable in case of large heat fluxes or accidental situations, where the key heat transfer phenomena just mentioned play a significant role in the heat transfer dynamics. Besides that, other 1D transient heat transfer models have been developed for the heat load control in RT for actively-cooled PFCs, for instance, the ones employed in the experimental tokamaks Joint European Torus (JET) in the UK [Valcárcel et al., 2014] and DIII-D in the US [Anand et al., 2021]. A similar 1D thermal model for RT applications, more specific for ITER and for the FW in the case of active cooling, has also been developed [Pesamosca et al., 2023]. Besides 1D simulations, 3D transient simulations of the FW have been performed, particularly by ITER Blanket Section [Hunt, 2023]. The Blanket Section is currently developing models for design purposes, therefore they are extremely accurate taking into account both thermal and electromagnetic loads for thermo-mechanical stability of the FW, thus they are not suitable as control-oriented models which inherently have a reduced complexity. Additionally, concerning 3D simulations, [Brank et al., 2019] proposed to employ 3D geometries of the FW to perform thermal simulations in steady-state conditions with the finite element method (FEM) in the case of active cooling, with the possibility of integrating such thermal models with the field line tracing environment SMITER software package, which computes the heat flux impacting the PFCs for a given plasma equilibrium and FW geometry [Kos et al., 2019]. Being this thermal model 3D and being developed in steady-state conditions, and thus not suitable as a control-oriented model (which instead should be simple and dynamic), it can be applied to accurately evaluate the FW temperature maps as inputs to optical simulations of IR cameras' response.

Nevertheless, for the purpose of model-based control design, the thermal models available in the literature lack a

fundamental requirement, i.e., the necessary flexibility to cope with the FW design evolution imposed by the ongoing re-baseline process. Therefore, this thesis work introduces novel thermal models capable of considering either beryllium or tungsten as FW material, either active or inertial cooling, and evolving FW geometries for the sake of FWHLC design.

For the purpose of active control, the thermal models available in the literature do not provide a systematic approach to identify the most suitable model for simulating transient heat transfer phenomena in the FW in a sufficiently accurate way yet compliant with the RT requirements of the PCS. Therefore, this thesis work aims to fill this research gap through quantitative analyses on the trade-off between accuracy and computational cost for the FWHLC operation in RT.

For the purpose of IR cameras' synthetic diagnostic, despite the recent development of [Brank et al., 2019], SMITER does not yet include a simplified but reliable way to generate FW temperature maps for IR cameras' synthetic diagnostics. Therefore, this thesis work has also the goal of integrating the present workflow in the case of active cooling of the FW by providing a complementary and simpler thermal model.

1.2 Aim of the study

The aim of this study is: to find the most representative thermal model for the FWHLC in terms of a compromise between accuracy and running time requirements for RT response; to analyze the thermal response of the FW of ITER; to find the simplest yet reliable thermal model for IR cameras' synthetic diagnostics. The specific goal is to develop two types of thermal models, the first one for the design and operation in RT of the FWHLC (thus being applicable for model-based control design and active control), and the second one for IR cameras' synthetic diagnostics.

The first model must fulfill the following requirements:

- be control-oriented, i.e., dynamic and capable of handling time-dependent inputs. As said, the FWHLC comes into play during transient conditions, therefore the model shall be capable of addressing transient heat transfer phenomena. Also, in the case of FW inertial cooling, heat transfer phenomena are intrinsically time-dependent
- be computationally efficient and run in real-time
- be implemented in MATLAB in order to ease its integration in the PCS, which is designed in MATLAB/Simulink [Ravensbergen et al., 2023]
- be general, i.e., be applicable to the entire FW, which is characterized by a complex three-dimensional toroidal geometry
- be as flexible as possible. Indeed, as said, the design of the FW is currently an ongoing process, therefore it is desirable to have a model flexible enough to accommodate potential modifications in their geometry and materials

The second model has instead the following requirements:

- be steady-state and as simple as possible. Indeed, as said, this approach aims to be complementary to the steady state 3D simulations developed by [Brank et al., 2019] but simpler
- be general
- be as flexible as possible (for the same reason as above)

As a consequence of the flexibility requirements, the models are coded from scratch in MATLAB without using external libraries.

1.3 Scope of the study

This work has the following scopes:

- the models developed are applied to the FW only, thus excluding the divertor, which involves much more complex physics and control [Ravensbergen et al., 2021]
- the analyses are carried out having tungsten as plasma facing material. However, the thermal models are kept flexible enough to change potentially, in the future, the material
- the RT thermal model for FWHLC is developed for the AFP phase only. It is still not clear if in the AFP phase the FW will be partially or exclusively inertially cooled. In any case, the models developed are flexible enough to account for either inertial cooling or active cooling
- as addressed more in detail in section 2.4, the FWHLC is applied in the case of nominal conditions and off-nominal conditions potentially leading to accidental events, leaving disruptions aside. Indeed, disruptions may take place at a much shorter time, thus requiring a different approach from the thermal modelling standpoint
- the thermal model for IR cameras' diagnostics is developed for the DT phase only, where the FW is foreseen to be actively cooled

1.4 Research questions

The research questions of this thesis can be formulated as such:

1. What is the most suitable thermal model in terms of a trade-off between accuracy and computational cost for the design and RT operation of the FWHLC in the AFP phase?
2. What is the transient thermal response of the entire ITER FW in the AFP phase?
3. What is the simplest but reliable model to generate temperature maps for IR cameras' synthetic diagnostics in the DT phase?

In this thesis, research questions are addressed starting with a theoretical background in chapter 2, followed by the methodology in chapter 3. Results and discussions are provided in chapter 4, followed by conclusions in chapter 5.

Chapter 2

Theoretical background

This chapter provides the theoretical foundation for this thesis work. It starts by giving a general overview of nuclear fusion in section 2.1, both in terms of underlying physical principles and tokamak technology, with a particular focus on the ITER project and its main components. Section 2.2 addresses the part of ITER object of this work, namely the Blanket system, followed by section 2.3 in which the transients occurring during ITER operation, for which a heat load controller is needed, are detailed. Section 2.4 introduces the FWHLC. The last two sections 2.5 and 2.6 provide the theoretical background needed for the development of the thermal models by presenting respectively the energy balance equations employed and numerical methods applied in this work.

2.1 Nuclear fusion

2.1.1 Physical principles

The idea of employing nuclear fusion for energy production comes from the intent of imitating what powers the Sun and the stars. A fusion reaction is a nuclear reaction, meaning that it involves the interaction between reactants' nuclei. These nuclei need to be close enough for the reaction to happen, therefore it is necessary to win the electrostatic repulsion between the positive charges composing the nuclei [Freidberg, 2008]. This can be achieved by reaching high temperatures so that particles acquire sufficient thermal energy to overcome the electrostatic repulsion. The combination of gravitational confinement and quantum tunneling effect allows the proton-proton reaction to take place in the Sun, whose core temperature reaches 15 million K. In order to realize fusion reactions on Earth, where gravitational confinement cannot be achieved for obvious reasons, other reactions are considered. On Earth, most experiments rely on the D-T reaction, in which D and T need to reach 150 millions K (corresponding to an energy of $10 - 20$ keV), 10 times more than in the core of the Sun, for a high reaction probability when they collide (as shown in figure 2.1b). At this temperature, a D and T mixture becomes a plasma, i.e., an ionized gas characterized by high conductivity which results globally neutral, but not locally. Additionally, as shown in figure 2.1, the D-T reaction has a lower energy threshold and a higher reaction rate for a given temperature than other fusion reactions.

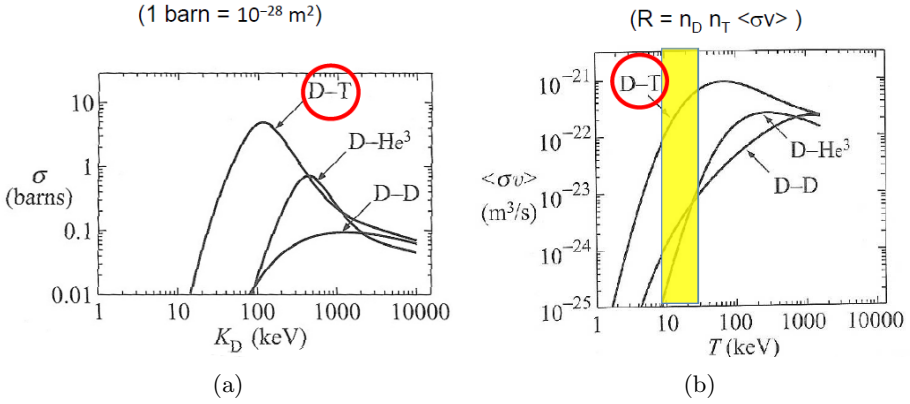

Figure 2.1: Comparison between D-T reaction and other fusion reactions: (a) fusion cross-section as a function of deuterium kinetic energy (the cross-section σ measures the probability of a reaction per square meter); (b) reaction rate σv weighted on the velocity distribution as a function of the temperature. Adapted from [Freidberg, 2008].

The D-T reaction is the following:

$$^2H +^3 H \rightarrow^4 He + n + 17.6 \text{ MeV} \tag{2.1}$$

where ^2H is deuterium, ^3H tritium, ^4He helium, and n a neutron. By looking at the binding energy per nucleon curve depicted in figure 2.2, namely the energy released when a nucleus is formed, it is possible to conclude that the reaction is exothermic. Indeed, there is a mass defect between products and reactants which translates into energy following Einstein's relation $E = mc^2$: the difference between the binding energy of ^4He and that of the reactants corresponds to the energy released by the reaction, approximately 17.6 MeV, released as kinetic energy. As a consequence of momentum and energy conservation, kinetic energy is divided among the products: the neutron receives 14.1 MeV, while the alpha particle (a nucleus of ^4He) the remaining 3.5 MeV.

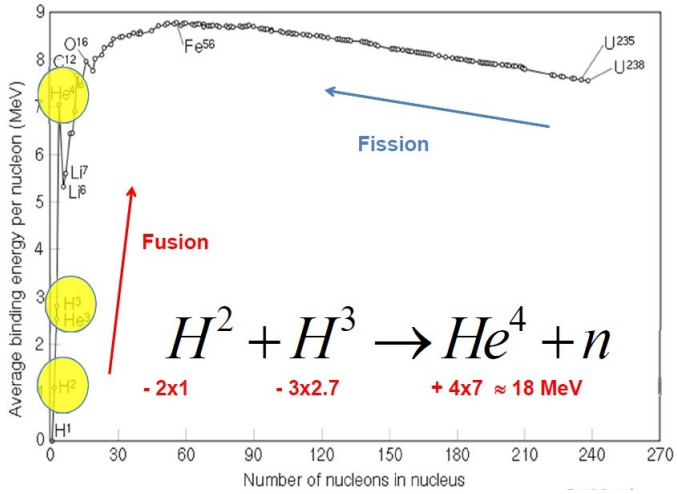

Figure 2.2: Binding energy per nucleon as a function of the number of nucleons. Adapted from [Wikipedia, n.d.].

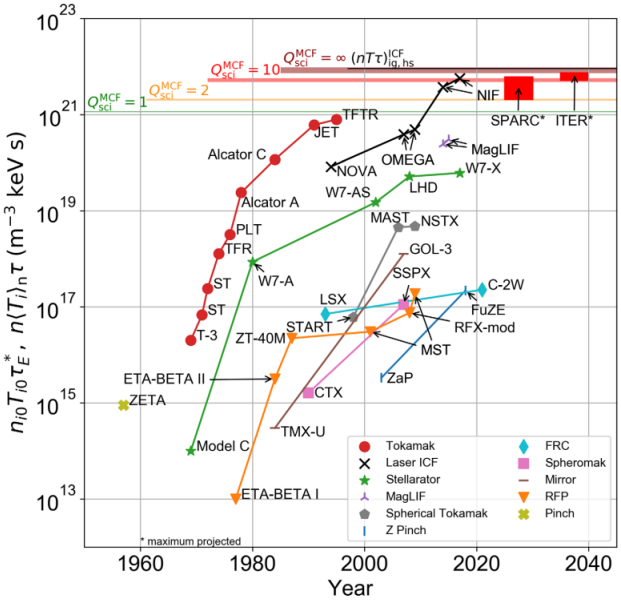

Figure 2.3: Triple products for MCF and ICF for a given concept vs year achieved [Wurzel and Hsu, 2022]. Note that for some of the experiments (like for ITER) a band is provided as the machines are not yet complete.

In order to have a fusion reaction, it is not sufficient to reach high temperatures, but it is also necessary for D and T to be close enough for a sufficient amount of time. In fusion physics, the "triple product" [Lawson, 1957] is often

used to quantify the requirements for a fusion reactor, and is defined as $n\tau_E T$, where n is the plasma density, τ_E is the confinement time (i.e., the rate at which a system loses energy to its environment), and T the temperature expressed in eV. It turns out that there is a minimum value of the triple product for fusion reactions to generate as much fusion energy as it is given to the plasma, and in particular $n\tau_E T \sim 10^{21}$ m$^{-3} \cdot$ s $\cdot$ keV. This value corresponds to a unitary energy gain $Q = 1$, the "break-even". For controlled engineering application, the goal is to obtain energy multiplication ($Q > 1$) and regulate the fusion power as a function of the external energy input ($Q < \infty$), thus, for a given temperature, the product $n\tau_E$ can be varied in such a way as to meet the requirements of a minimum value of the triple product. In order to do so, there are two strategies that define the two main research pathways: inertial confinement fusion (ICF) and magnetic confinement fusion (MCF). The former is based on maximizing the plasma density with a relatively low confinement time, the opposite for the latter. Figure 2.3 gives an idea about the progress of the current experiments and facilities towards the break-even.

2.1.2 Fusion experiments and tokamaks

While this thesis is being written, as shown in figure 2.3, there are several ongoing experimental projects and start-ups around the world, both focusing on ICF and MCF [Meschini et al., 2023]. Concerning ICF, the main experiment is the National Ignition Facility in the US, in which relatively high plasma densities are achieved through high-power lasers. Concerning MCF, there are different machine configurations, e.g., stellarators, and tokamaks. While stellarators employ complex-shaped magnets to achieve plasma confinement, in tokamaks the plasma is confined in a toroidal chamber. The main stellarator project is Wendelstein 7-X in Germany, while the main tokamaks projects, besides the already cited JET in the UK and DIII-D in the US, are ASDEX Upgrade in Germany, EAST in China, KSTAR in South Korea, JT-60SA in Japan, SPARC in the US, and ITER in France.

In particular, in tokamaks, in order to effectively confine the plasma, three kinds of magnets are necessary, namely toroidal magnets, a central solenoid, and poloidal magnets. As depicted in figure 2.4, these magnets generate respectively the toroidal component of the magnetic field, the poloidal one, and the vertical one. An electric current is driven in the toroidal magnets generating a toroidal magnetic field B_ϕ which is given by Ampere's law (figure 2.5). The central solenoid relies upon the working principle of a transformer: the plasma is the secondary side of a transformer having the central solenoid as the primary side. A ramp variation of current flowing in the central solenoid generates a variable magnetic field, which generates in turn an electric field according to Faraday's law when the magnetic flux is concatenated to a coil represented by the plasma itself. Being the plasma a resistive medium, a plasma current of the order of magnitude of MA is induced in the plasma following Ohm's law. The plasma current generates the poloidal magnetic field B_θ. The combination of a toroidal magnetic field and a poloidal magnetic field results in a helical magnetic field. Finally, poloidal magnets are used in order to get a certain plasma shape so that it is not unstable. The resulting magnetic field is very high, of the order of magnitude up to several T, approximately 5 orders of magnitude more than the magnetic field on Earth.

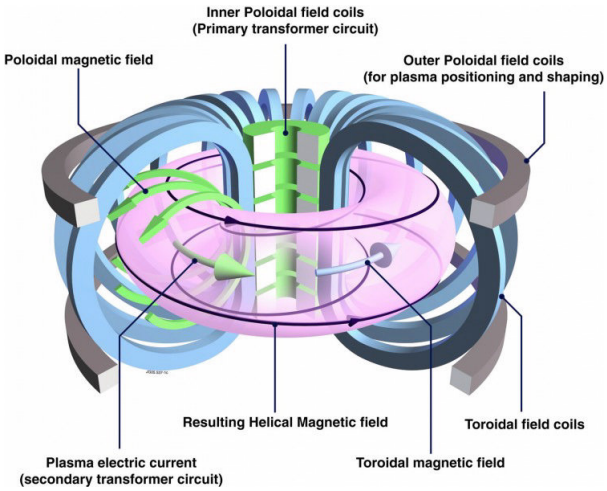

Figure 2.4: Magnetic field components in a tokamak [Federici et al., 2019].

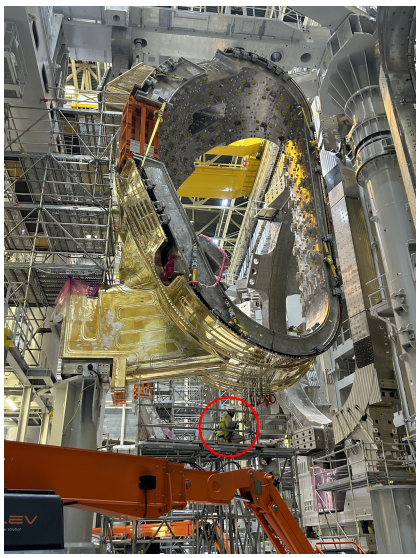

Figure 2.5: Picture of an ITER toroidal magnet taken during a site visit. Note the magnet's size compared to the operator circled in red.

In tokamaks, the energy gain Q is a function of the radius of the machine and the magnetic field as shown in figure 2.6. The same energy gain Q can be achieved with a relatively low radius and very high magnetic field, which is the case of SPARC where High-Temperature Superconductors are employed, or alternatively with a higher radius and lower magnetic field, which is the case of ITER. In ITER, superconductor magnets are typically refrigerated with supercritical helium at 4 K. This characteristic of the magnets, together with their complex shape and huge dimensions, make them very delicate components of tokamaks, thus constituting a significant amount of the total up-front cost.

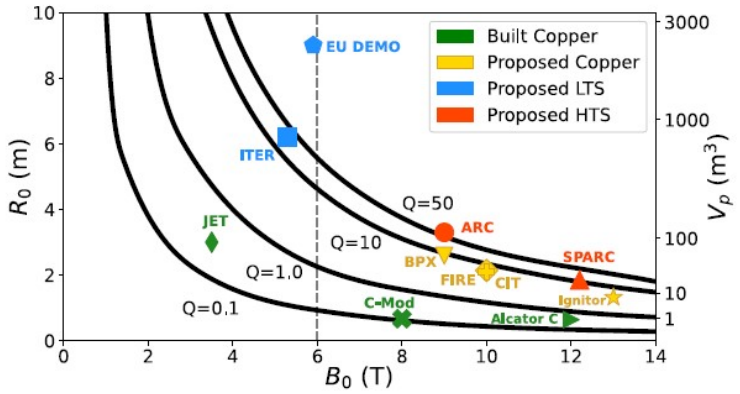

Figure 2.6: Energy gain Q as a function of major radius R_0 and toroidal magnetic field B_0 for several tokamaks characterized by different types of magnets (namely, copper, Low-Temperature Superconductors (LTS), and High-Temperature Superconductors (HTS)[Creely et al., 2020].

2.1.3 ITER project and its main components

As already stated in chapter 1, ITER is an international project aiming to be the largest tokamak on Earth and to obtain a Q = 10. ITER is characterized by a major radius of 6.2 m and nominal values of plasma current and toroidal magnetic field of 15 MA and 5.3 T respectively [Li et al., 2019]. ITER will not produce electricity, but it is essential for the commercialization of fusion energy as it will contribute to demonstrating the operation of technologies for a power plant. Fusion power plants, such as DEMO, will be based on the fact that neutrons emitted by fusion reactions, having no electric charge, are not influenced by the total magnetic field, thus interacting with the components behind the tokamak wall, generating thermal energy which in turn can be converted into electricity through a turbine. The kinetic energy of α particles can be employed to heat the plasma and compensate for the thermal losses due to energy and particle transport.

Besides magnets, tokamaks encompass several components, the main ones being, in the case of ITER, the following (figure 2.7):

- vacuum vessel. It is the structure containing the chamber hosting the plasma. As fusion reactions require an extremely pure fuel mix, the vacuum vessel is kept under vacuum conditions. Moreover, it represents the first containment barrier for the neutrons released by fusion reactions, therefore is made of borated steel for neutron shielding. The thermal energy deposited by neutrons during operation is removed through primary cooling water systems. These systems are then connected to secondary cooling systems, which are finally connected to cooling towers for heat rejection to the environment. Again, ITER is not designed for electricity production, but in the future commercial power plants' cooling systems will serve as power cycles in connection with steam turbines
- blanket. The blanket is composed of blanket modules (BM) directly facing the hot plasma and has two main functions: conversion of neutrons' kinetic energy into thermal energy and neutrons shielding. Moreover, some of ITER blanket modules will be replaced with special modules testing the "tritium breeding concept", namely the production of tritium from lithium in situ. The blanket portion facing the plasma is called first wall (FW) and is composed of first wall panels (FWPs)
- cryostat. It is a stainless steel structure containing the vacuum vessel and the superconducting magnets, ensuring the vacuum and a sufficiently low temperature for the proper operation of magnets
- ports. The vacuum vessel is characterized by dozens of openings, called ports, for various purposes, e.g. diagnostics, vacuum systems, remote handling, and external heating systems. Indeed, the heat released by α particles is not enough to sustain autonomously the fusion reaction rate for which the machine is designed, therefore ITER relies on the heat provided by the plasma current and by external heating systems, namely neutral beam injection and two sources of high-frequency electromagnetic waves
- divertor. Together with the blanket, it directly faces the hot plasma. Together they are referred to as plasma-facing components (PFCs). The divertor is designed to manage particle fluxes and thermal fluxes, besides minimizing plasma contamination.

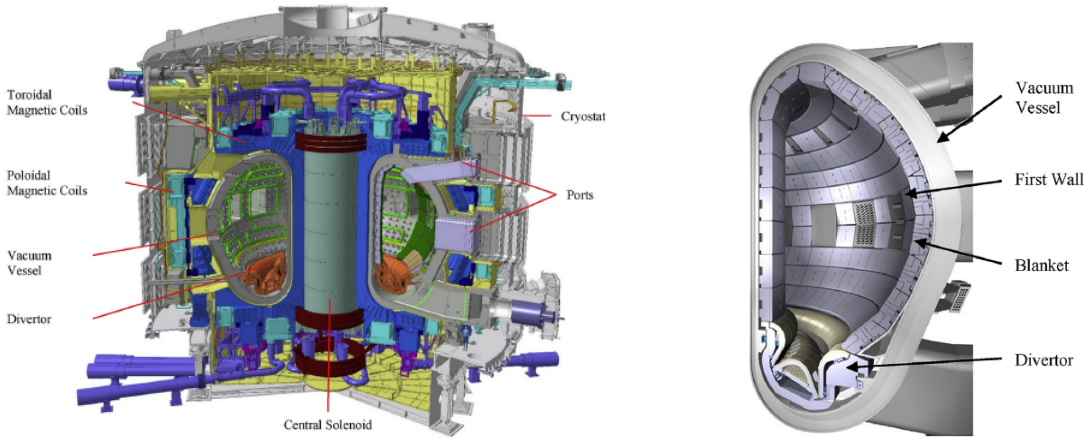

(a) (b)

Figure 2.7: (a) ITER main components. (b) ITER poloidal cross section [ITER Organization, n.d.b].

2.2 ITER Blanket systems

The blanket of ITER is a PFC having the multiple objectives of providing thermal and neutron shielding both to the vacuum vessel and superconducting magnets, limiting plasma contamination, and withstanding heat loads during nominal transient conditions and accidental events [Merola et al., 2010]. The blanket is composed of 440 blanket modules (BMs), which cover the VV inner wall. In a poloidal cross-section, there are 18 BMs which can be divided into three groups according to the three zones called high-field side (HFS), top side, and low-field side (LFS). HFS and LFS refer to the magnitude of the toroidal magnetic field. A BM is composed of two main components, the shield block (SB) and the first wall panel (FWP). The SB provides mechanical and electrical connections of the BM to the

VV and contains the manifolds for the SB cooling, while the FWP is the component directly facing the hot plasma. A FWP is mechanically connected to a SB through bolts, located in the middle of the FWP itself. Figures 2.8 and 2.9 depict the above description.

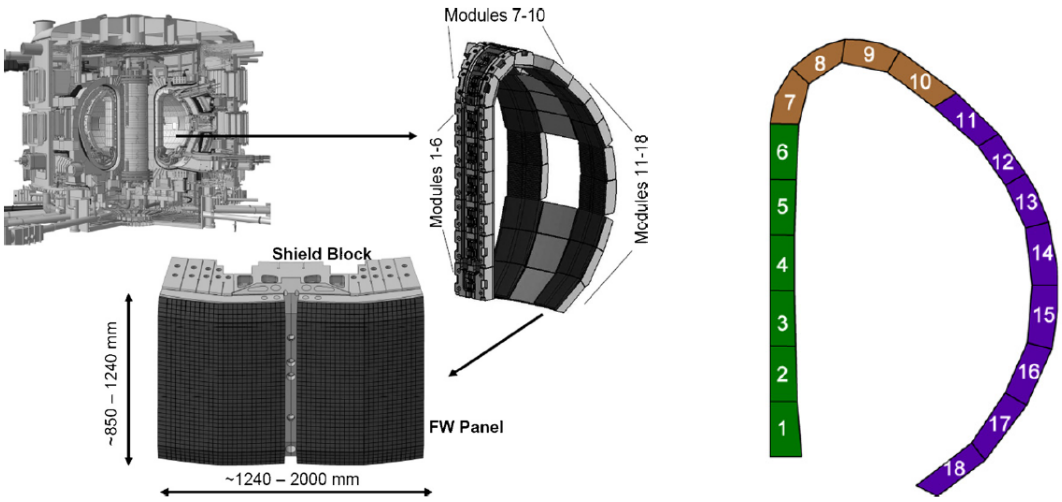

(a) (b)

Figure 2.8: (a) BM structure and order of magnitude of FWPs' dimensions [Merola et al., 2010]. (b) ITER's poloidal cross section showing BMs' specific numbers and the three zones (HFS in green, top in brown, LFS in purple) [Pitts et al., 2011].

.

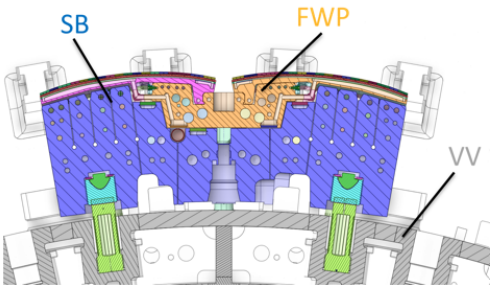

Figure 2.9: Detail of an SB and its connection to the VV [Hunt, 2023].

2.2.1 First wall panels design

As depicted in figure 2.10, FWPs are divided into fingers installed onto a support beam [Pitts et al., 2011]. Fingers are essential to limit the formation of eddy currents in the plasma-facing materials and can be individually manufactured, assembled, and inspected through remote handling systems.

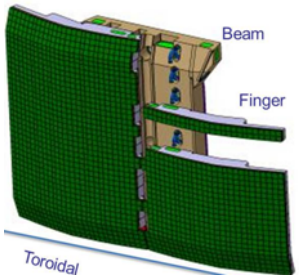

Figure 2.10: FWP subdivided into fingers [Brank et al., 2019].

As charged particles move following magnetic field lines, the incidence angle of the latter on FWPs is an important parameter for their design. Indeed, charged particles are characterized by a thermal flux denoted as $q_{//}$, whose projection on FWPs is (denoted as $q_{\perp}$), and the higher the incidence angle the higher $q_{\perp}$ is. Fortunately, as the toroidal field is much stronger than the poloidal field, incidence angles are relatively low. However, the heat flux needs to be further lowered in some critical edges like FWPs penetrations. That being the case, FWPs have toroidally shaped front surfaces for optimized power spreading, thus providing magnetic shadowing and separating "shadowed areas" from "wetted areas". At first, it was believed $q_{//}$ (evaluated at the outer midplane of the machine) to decay with a single exponential close to the wall, but in 2013 during an experimental campaign at the experimental tokamak JET in the UK, a double exponential was found [Arnoux et al., 2013]. This led to the new toroidal shaping profile depicted in figure 2.11.

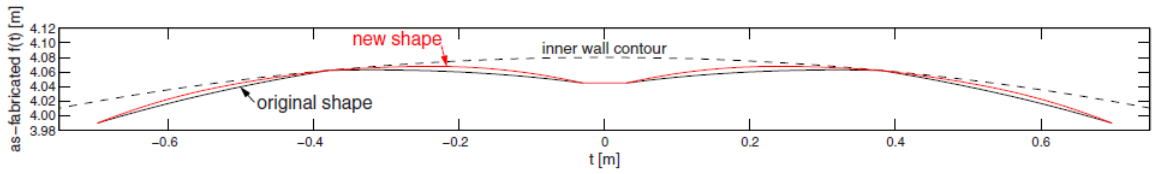

Figure 2.11: FWPs' original and new shaping following experimental campaigns at JET in 2013 [Kocan et al., 2015].

Before the re-baseline, detailed studies led to two different designs of FWPs, namely Normal Heat Flux (NHF) and Enhanced Heat Flux (EHF) panels, both actively cooled and capable of accommodating 2 MW/m^2 and 4.7 MW/m^2 respectively [Mitteau et al., 2013]. In both types of panels, each finger is individually cooled and is composed of armour tiles made of a plasma-facing material, a heat sink made of the copper alloy CuCrZr, and a stainless steel support structure. In NHF fingers, the cooling channels are stainless steel pipes, while EHF fingers rely on the hypervapotron technology, namely rectangular cooling channels designed for maximizing the heat transfer coefficient. Additionally, NHF and EHF armour tiles are divided into small cells, i.e., "castellations", for thermo-mechanical stability [Litnovsky et al., 2009]. Figures 2.12 and 2.13 depict NHF and EHF panels design respectively before the re-baseline. Currently, it is envisaged to use the same design as in the past with the only difference of having W tiles instead of Be ones facing the plasma. As anticipated in chapter 1, with the re-baseline, a new type of FWP has been introduced, namely temporary first wall (TFW) panels, which are inertially cooled and will be employed in the AFP phase. Their design is still under discussion but, at the moment of this thesis finalization, the current concept design is the one depicted in figure 2.14. Currently, it is still unclear whether ITER FW will be entirely covered by TFW panels during the AFP phase or by a mix of TFW, EHF, and NHF panels. Conversely, in the DT phase, the FW will be exclusively covered by NHF and EHF panels as shown in figure 2.15.

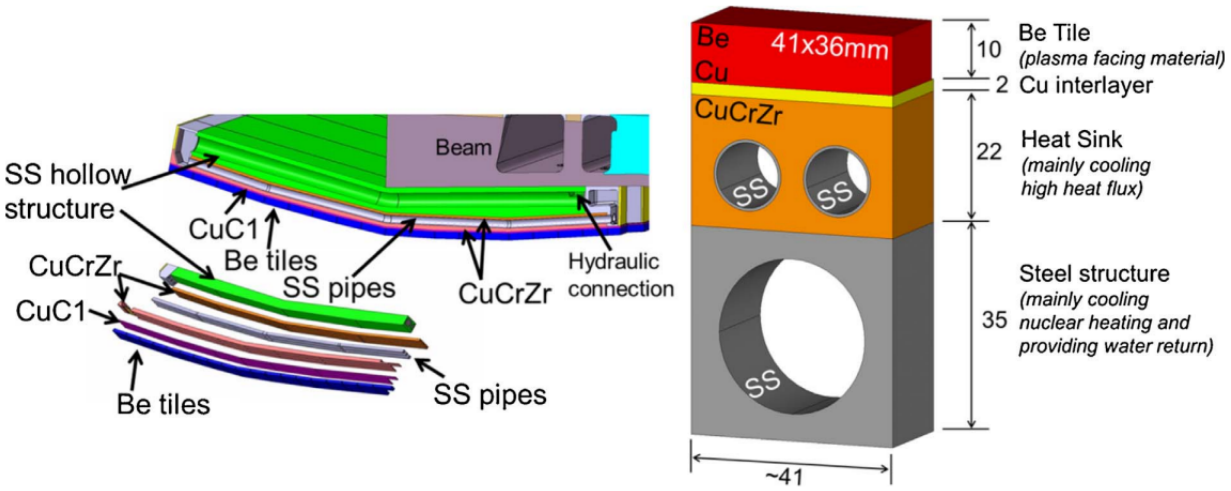

Figure 2.12: Design of NHF before the re-baseline with a particular on the cross-section [Perez-Pichel et al., 2017].

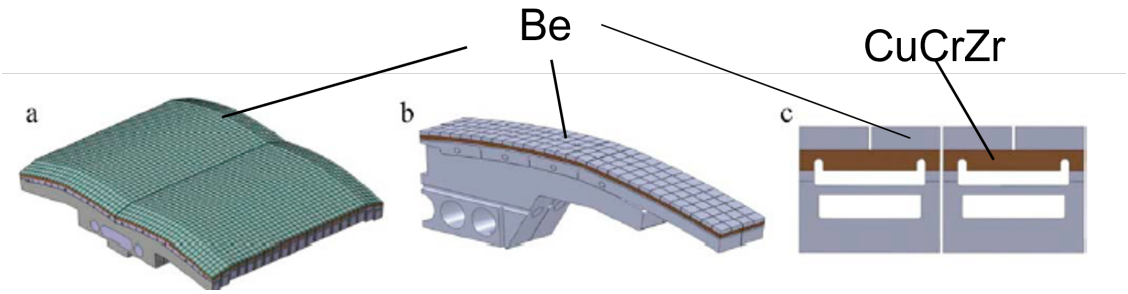

Figure 2.13: Design of EHF panels before the re-baseline: (a) FWP general view; (b) finger; (c) cross-section. Adapted from [Mazul et al., 2012].

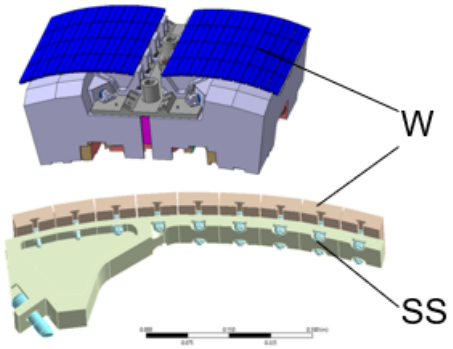

Figure 2.14: Current TFW panel design and particular of a generic finger. Adapted from [Hunt, 2023]. Note that, in this design, W tiles are characterized by toroidal gaps.

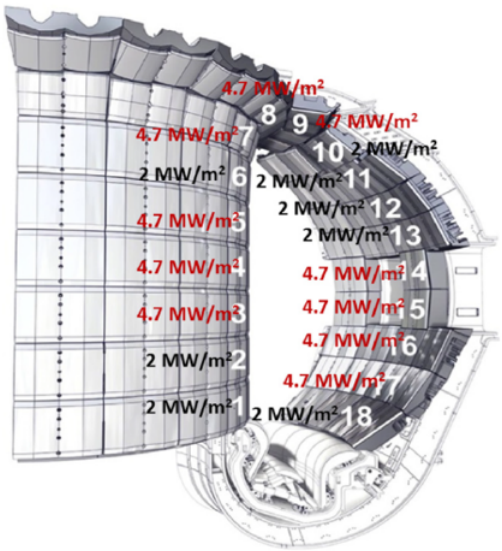

Figure 2.15: Distribution of NHF and EHF panels in the DT phase [Mitteau et al., 2013]. Figure adapted from [Kocan et al., 2015].

2.3 Transients occurring during ITER operation

During ITER operation there are several transients, the main ones being ramp-up and ramp-down phases, L-H transition, and plasma instabilities, described hereafter. The FW is designed to withstand all of them.

2.3.1 Ramp-up and ramp-down phases

As the plasma current is induced by the central solenoid following the working principle of a transformer, the operation of ITER will be pulsed, meaning that the plasma will be generated by the ionization of a neutral gas at the beginning of each pulse [Ravensbergen et al., 2023]. As shown in figure 2.16, the plasma current follows three operational phases: ramp-up, flat-top, and ramp-down.

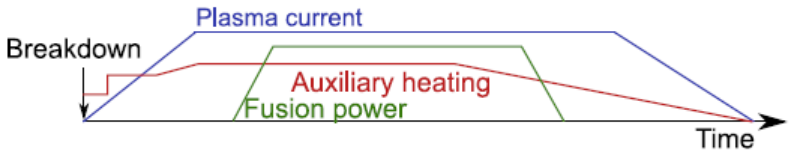

Figure 2.16: Plasma current operational phases [Ravensbergen et al., 2023].

The typical operation of a plasma pulse at ITER is hereafter described. During ramp-up and ramp-down phases, as depicted in figure 2.17, the plasma is "limited" on the central column of the FW, located on the HFS, meaning that it is in direct contact with FWPs (the plasma start-up happens on the central column itself). As a consequence, in the ramp-up and ramp-down phases, the central column of the FW experiences its largest incident time-dependent heat flux of the entire nominal operation. During the ramp-up phase, the plasma passes from being limited to being "diverted". In this state, the plasma is characterized by a so-called x-point (see magenta line in figure 2.17) and is detached from the central column. When the plasma is diverted, the majority of the heat exhausted from the plasma is discharged onto the divertor, therefore the FW receives relatively low heat fluxes. When the plasma current reaches the flat-top, the plasma is diverted in the so-called "L mode", which corresponds to a plasma low confinement state [Freidberg, 2008]. When the plasma is diverted in L mode this corresponds to the steady-state phase of a single pulse. Additionally, a plasma pulse operation can be designed such that the plasma undergoes a transition from a low confinement state to a high confinement state, referred to as H mode. A plasma in H-mode is characterized by a confinement time τ_E approximately twice as in L-mode, therefore reaching H-mode is desirable from the standpoint of a fusion reactor economy. For the duration of the LH transition (fractions of a second), inherently dynamic, the incident heat flux on the FW is again time-dependent. Apart from this, it is expected that for the majority of the L or H mode, the incident heat flux on the central column of the FW is considerably lower with respect to ramp-up and ramp-down phases, as it is concentrated by design in the divertor region, although significant heat fluxes can impact the upper FW also in H mode.

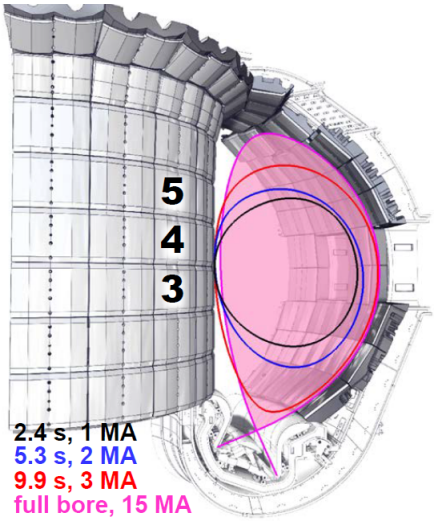

Figure 2.17: Plasma magnetic surfaces in the ramp-up phase for increasing values of the plasma current [Pitts, 2019]. Note that when the plasma is limited it is in contact with the central column of the FW, while when the plasma is diverted it is detached from the wall. Note also the x-point when the plasma is diverted.

2.3.2 Plasma instabilities

Plasmas are high-order non-linear systems subjected to numerous types of instabilities, which are inherently dynamic thus determining time-dependent heat loads [Pironti and Walker, 2005]. As stated in section 2.1, in order to reach the break-even, plasmas must be heated and confined in such a way as to reach the necessary triple product. However, as its temperature and density increase, a plasma becomes more unstable. During an instability, a plasma can possibly undergo a disruption, in which it suddenly changes its structure and can not be magnetically confined anymore, thus losing its energy to the surrounding structures and eventually extinguishing. The energy deposited on PFCs following a plasma disruption represents a serious threat, as it may potentially lead to unacceptable surface erosion and plasma contamination in successive plasma pulses.

There are several types of plasma instabilities, characterized by very different time scales, which can be divided into long-term and short-term instabilities. Among short-term instabilities, there are edge localized modes (ELMs), which take place when the plasma is in H-mode [Freidberg, 2008]. Short-term instabilities are fast compared to the characteristic thermal time scales of the first wall, which will be shown in section 4.1.7 to be in the order of 1 s. A typical approach to include their effect in thermal simulations that have a duration comparable to a plasma discharge (~ 100 s) is to consider only the time-averaged contribution of cyclical fast instabilities [Kocan et al., 2015]. Conversely, long-term instabilities, whose characteristic time is around 1 s, may be corrected in real-time using feedback control, and their influence on the FW surface temperature can be controlled.

2.4 First Wall Heat Load Controller

Due to unavoidable energy and particle transport in tokamak plasma, charged particles escape from the magnetic confinement thus hitting PFCs. As a consequence, not only these charged particles deposit thermal fluxes on the wall materials, but they also damage and erode the structures. The phenomenon of erosion, known as sputtering, causes impurities to flow in the core plasma, where they can irradiate away the plasma energy thus causing nuclear reactions, which are thermally sustained, to stop. For this reason, as pointed out before, the divertor is designed to concentrate particle fluxes thus managing thermal flux deposition and plasma contamination. In order to do so, the magnetic field is optimized to avoid contact of the core plasma with the wall and divert the most external flux surface onto the divertor, thereby concentrating particle fluxes and heat exhaust on it. The resulting configuration of diverted plasma is qualitatively shown in figure 2.18. In this configuration, there are two regions, namely the core plasma region and the scrape-off layer (SOL) region, separated by the separatrix, which for diverted plasma is the magnetic surface including the x-point (a point where the magnetic field is identically zero). The SOL region is a continuous region in space, but the heat flux deposited by charged particles decays exponentially [Stangeby et al., 2000], therefore in steady-state conditions during the flat-top phase in L mode the heat load is managed by the cooling system of the divertor [Mitteau et al., 2010]. However, in transient nominal conditions, i.e., when the plasma is limited in ramp-up and ramp-down phases, or off-nominal conditions such as plasma instabilities, the FW is subjected to heat loads much higher than in steady-state conditions. That being the case, it is essential to design a First Wall Heat Load Controller (FWHLC) to effectively manage heat exhausted from the plasma to the FW during these transient events.

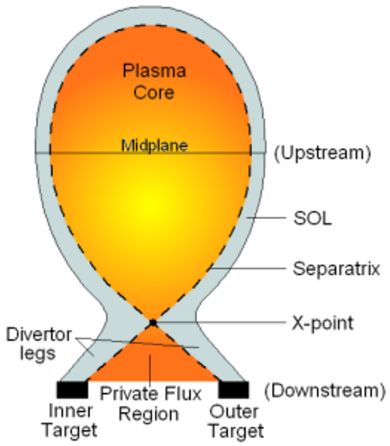

Figure 2.18: Magnetic field lines in the presence of a divertor [Kumar, 2021].

The FWHLC is part of the broader Plasma Control System (PCS), which is composed of controllers receiving measurements from diagnostics in real-time and sending signals to ITER actuators accordingly [Ravensbergen et al., 2023]. The PCS, currently in the design process for the AFP phase at EPO at ITER, is being implemented in the PCS Simulation Platform (PCSSP), a specific framework in Simulink [Walker et al., 2015]. In particular, the FWHLC is characterized by a modular structure in order to benchmark and validate specific modules against more accurate simulations and evaluates the thermal response onto the FW in real-time by combining temperature measurements from IR cameras and heat flux estimations for a given plasma equilibrium [Pesamosca et al., 2023]. The FWHLC (in blue in figure 2.19) will be designed with a model-based approach, where a dynamical model of the physical process to control is an integral part of the controller synthesis procedure. This lightweight control-oriented dynamical model for the simulation of ITER wall temperature response to transients in the plasma shape and auxiliary power is validated against high fidelity codes (in light blue in figure 2.19).

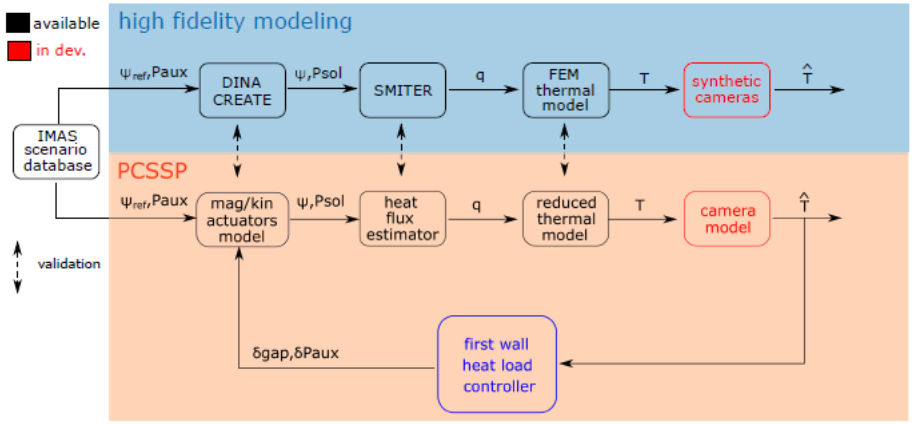

Figure 2.19: Design of the FWHLC in the PCSSP [Pesamosca et al., 2023].

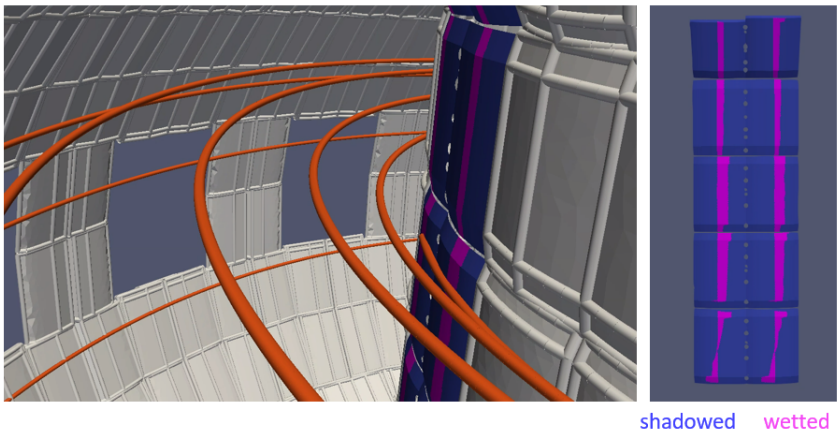

Figure 2.20: Typical distribution of magnetic field lines (highlighted in orange on the left), which determine shadowed and wetted areas (on the right) [Pesamosca, 2023]. For a given FWP, the wetted area is cast by the apex of the neighbor FWP.

The constituting modules of the FWHLC are actuator models, a heat flux estimator, a thermal model, and IR cameras model. Actuators are either magnetic or kinetic. Through magnetic actuators, it is possible to modify the plasma shape, while through kinetic actuators the auxiliary power coupled with the plasma. Indeed, by lowering the auxiliary power, the power lost from the plasma to the SOL because of particle diffusion, indicated as P_{SOL}, is lowered accordingly. The output of this model, namely the magnetic equilibrium Ψ and P_{SOL}, constitutes the input for the heat flux estimation, through which it is possible to determine the wetted area on a specific FWP and calculate the incident heat flux (figure 2.20). The heat flux is the input of a thermal model, which evaluates its thermal response. The resulting temperature distribution, complementary to the measurements with IR cameras, is the input for the

controller. The thermal model flanks IR cameras' measurements because of their limited FW coverage. Moreover, the temperature map can be used to perform synthetic diagnostics for IR cameras [Aumeunier et al., 2017].

It is important to underline that the FWHLC is a part of the broader PCS limited to work during nominal and off-nominal transient events in which the plasma can be too close to the FW (as it may happen when the plasma is limited) or when it receives excessive heat load after the L-H transition. In both cases, the incident heat flux on the FW may lead to unacceptable temperatures. The FWHLC is therefore not designed for handling disruptions, as they are characterized by different time scales. Specifically, the incident heat flux on the FW is composed of the thermal power coming from the SOL (specifically, its projection on the normal direction of a FWP) and, when the plasma is in H mode, time-averaged ELMs load.

2.5 Energy balance equation for First Wall Panels

This section provides the theoretical foundations to formulate the energy balance equation for FWPs, which is implemented in the thermal model to find the temperature distribution.

Starting from the first law of thermodynamics in integral form applied to a Control Volume (CV) coinciding with a generic infinitesimal element:

$$\frac{D}{Dt}\int_{V(t)} \rho e dV = \Phi + \sum W + S \tag{2.2}$$

where ρ is the density, *V(t)* a time-dependent volume, e the total energy, Φ is the net heat flux, $\sum W$ the rate of work done by forces onto the CV, and S internal sources [Munson et al., 2013]. The left-hand side represents the rate of change, expressed with a total derivative, of the total energy, which is defined as follows:

$$e = u + \frac{1}{2}\vec{v}\cdot\vec{v} \tag{2.3}$$

where u is the internal energy and $\frac{1}{2}\vec{v}\cdot\vec{v}$ the kinetic energy, being $\vec{v}$ the velocity. By considering pressure p, viscous stresses $\vec{\tau}$, and body forces per unit of mass F as acting on the CV, the equation 2.2 can be written as:

$$\begin{aligned}\frac{D}{Dt}\int_{V(t)} \rho\left[u + \frac{1}{2}\vec{v}\cdot\vec{v}\right]dV = &-\int_{S(t)} \vec{q}\cdot\vec{n}dS - \int_{S(t)} p\vec{v}\cdot\vec{n}dS + \\ &+\int_{S(t)} (\vec{\tau}\cdot\vec{v})\cdot\vec{n}dS + \int_{V(t)} \rho\vec{F}\cdot\vec{v}dV + \int_{V(t)} \phi dV\end{aligned} \tag{2.4}$$

where $\vec{q}$ the heat flux per unit area, ϕ the heat generated per unit volume, $S(t)$ the potentially time-dependent surface of the CV, and $\vec{n}$ the vector normal to the surface pointing outside the volume. This expression can be further simplified by applying the Reynolds theorem to the left-hand side term, allowing to move the total derivative inside the integral [Munson et al., 2013]. Additionally, the application of the Gauss theorem leads to the following expression:

$$\begin{aligned}\int_{V(t)} \frac{D}{Dt}\rho\left[u + \frac{1}{2}\vec{v}\cdot\vec{v}\right]dV = &-\int_{V(t)} \vec{\nabla}\cdot\vec{q}dV - \int_{V(t)} \vec{\nabla}\cdot(p\vec{v})dV + \\ &+\int_{V(t)} \vec{\nabla}\cdot(\vec{\tau}\cdot\vec{v})dV + \int_{V(t)} \rho\vec{F}\cdot\vec{v}dV + \int_{V(t)} \phi dV\end{aligned} \tag{2.5}$$

Being this expression completely independent from any specific definition of CV, it is also equivalent to the following:

$$\frac{D}{Dt}\rho\left[u + \frac{1}{2}\vec{v}\cdot\vec{v}\right] = -\vec{\nabla}\cdot\vec{q} - \vec{\nabla}\cdot(p\vec{v}) + \vec{\nabla}\cdot(\vec{\tau}\cdot\vec{v}) + \rho\vec{F}\cdot\vec{v} + \phi \tag{2.6}$$

Bearing in mind the definition of the total derivative, i.e. $\frac{D}{Dt}\rho\left[u + \frac{1}{2}\vec{v}\cdot\vec{v}\right] = \frac{\partial}{\partial t}\left(\rho u + \frac{1}{2}\rho v^2\right) + \left(\vec{v}\cdot\vec{\nabla}\right)\left(\rho u + \frac{1}{2}\rho v^2\right)$, the kinetic energy term can be canceled out by applying the momentum equation [Anderson and Wendt, 1995]. In this way, the energy balance equation can be expressed in the following form:

$$\frac{\partial}{\partial t}(\rho u) + \vec{\nabla} \cdot (\rho u \vec{v}) = -\vec{\nabla} \cdot \vec{q} - p\vec{\nabla} \cdot \vec{v} + \vec{\tau} \cdot \vec{\nabla} v + \phi \tag{2.7}$$

It is worthwhile underlining that the density can be extracted from the partial derivatives in the left-hand side term. Indeed:

$$\frac{\partial}{\partial t}(\rho u) + \vec{\nabla} \cdot (\rho u \vec{v}) = \rho \frac{\partial u}{\partial t} + \vec{\nabla} u \cdot (\rho \vec{v}) + u \left(\frac{\partial \rho}{\partial t} + \vec{\nabla} \cdot (\rho \vec{v}) \right) \tag{2.8}$$

but $\left(\frac{\partial \rho}{\partial t} + \vec{\nabla} \cdot (\rho \vec{v}) \right) = 0$ for the continuity equation, thus:

$$\frac{\partial}{\partial t}(\rho u) + \vec{\nabla} \cdot (\rho u \vec{v}) = \rho \frac{\partial u}{\partial t} + \vec{\nabla} u \cdot (\rho \vec{v}) = \rho \cdot \left[\frac{\partial u}{\partial t} + \vec{\nabla} \cdot (u \vec{v}) \right] \tag{2.9}$$

Therefore, equation 2.7 can be further simplified as follows:

$$\rho \frac{\partial u}{\partial t} + \rho \vec{v} \cdot \vec{\nabla} u = -\vec{\nabla} \cdot \vec{q} - p\vec{\nabla} \cdot \vec{v} + \vec{\tau} \cdot \vec{\nabla} v + \phi \tag{2.10}$$

which is the general expression for the energy balance equation.

As previously mentioned, the thermal models are applied to FWPs, which are obviously solid bodies. That being the case, the internal energy u reduces to $u = c(T)T$, with c being the specific heat and T the temperature [Moran et al., 2010]. In a solid body, the means of heat transfer are conduction and radiation heat transfer, with the latter being considered as occurring on the surface of the material only [Bergman et al., 2011]. As a consequence $\vec{v} = 0$, allowing to neglect both compressible and viscous terms ($p\vec{\nabla} \cdot \vec{v}$ and $\vec{\tau} \cdot \vec{\nabla} v$ respectively), as well as the transport term ($\rho \vec{v} \cdot \vec{\nabla} u$). Finally, by modeling conduction heat transfer through Fourier's law, namely $\vec{q} = -k(T)\vec{\nabla} T$ with k being the heat conductivity, it is possible to write the energy balance equation for a solid:

$$\rho(T) \frac{\partial (c(T)T)}{\partial t} = \vec{\nabla} \cdot (k(T) \vec{\nabla} T) + \phi \tag{2.11}$$

where the left-hand side can be written as $\left(\rho(T)c(T) + \rho(T)T \frac{\partial c(T)}{\partial T} \right) \frac{\partial T}{\partial t}$ by computing the partial derivative. It is worthwhile stressing that this equation is quite general, and can be applied to any solid body. Strictly speaking, this applies to any isotropic solid body. Indeed, thermal properties are assumed to be potentially dependent on temperature only, and not by any space coordinate.

As reported in Appendix A, which contains materials properties adopted for the present study, the relation between specific heat and temperature can be modeled as a polynomial approximation for the materials of interest in this work, namely SS, CuCrZr, and W. In particular, the specific heat can be generally expressed as $c(T) = c_0 + c_1 T + c_2 T^2$, with c_0, c_1, and c_2 depending on the specific material. It can be shown that the left-hand side term of equation 2.11 can be written as $\rho(T) \cdot \left[c_0 + 2c_1 T + 3c_2 T^2 \right] \cdot \frac{\partial T}{\partial t}$ [Hristov, 2023]. If then a "corrected" specific heat is defined as $c^* = \left[c_0 + 2c_1 T + 3c_2 T^2 \right]$, thereby accounting for its dependence upon the temperature, the equation 2.11 can be expressed in the following compact form:

$$\rho(T) c^*(T) \frac{\partial T}{\partial t} = \vec{\nabla} \cdot (k(T) \vec{\nabla} T) + \phi \tag{2.12}$$

As it will be subsequently explained, in this work FWPs are modeled by employing 1D and 2D simplifications, thus the previous equation is hereafter particularized in these two cases respectively.

2.5.1 1D simplification

When considering a 1D simplification, the divergence terms are reduced to:

$$\vec{\nabla} \cdot (k(T)\vec{\nabla}T) = \frac{\partial}{\partial x}\left(k(T)\frac{\partial T}{\partial x}\right) = k(T)\frac{\partial^2 T}{\partial x^2} + \frac{\partial k(T)}{\partial x} \cdot \frac{\partial T}{\partial x} = k(T)\frac{\partial^2 T}{\partial x^2} + \frac{\partial k(T)}{\partial T} \cdot \left(\frac{\partial T}{\partial x}\right)^2 \tag{2.13}$$

By substituting this expression in equation 2.12, the 1D energy balance for a solid body with temperature-dependent properties is expressed by:

$$\rho(T)c^*(T)\frac{\partial T}{\partial t} = k(T)\frac{\partial^2 T}{\partial x^2} + \frac{\partial k(T)}{\partial T} \cdot \left(\frac{\partial T}{\partial x}\right)^2 + \phi \tag{2.14}$$

In the particular case of constant thermal properties, this equation reduces to:

$$\rho c\frac{\partial T}{\partial t} = k\frac{\partial^2 T}{\partial x^2} + \phi \tag{2.15}$$

2.5.2 2D simplification

When considering a 2D simplification, the divergence term reduces to:

$$\begin{aligned}\vec{\nabla} \cdot (k(T)\vec{\nabla}T) &= k(T) \cdot \nabla^2 T + \vec{\nabla}T \cdot \vec{\nabla}k(T) = \\ &= k(T)\left[\frac{\partial^2 T}{\partial x^2} + \frac{\partial^2 T}{\partial y^2}\right] + \frac{\partial k}{\partial x} \cdot \frac{\partial T}{\partial x} + \frac{\partial k}{\partial y} \cdot \frac{\partial T}{\partial y}\end{aligned} \tag{2.16}$$

As for the 1D simplification, this equation can be written in a compact way:

$$\rho(T)c^*(T)\frac{\partial T}{\partial t} = k(T)\left[\frac{\partial^2 T}{\partial x^2} + \frac{\partial^2 T}{\partial y^2}\right] + \frac{\partial k}{\partial x} \cdot \frac{\partial T}{\partial x} + \frac{\partial k}{\partial y} \cdot \frac{\partial T}{\partial y} + \phi \tag{2.17}$$

In the particular case of constant thermal properties, this equation reduces to:

$$\rho c\frac{\partial T}{\partial t} = k\left[\frac{\partial^2 T}{\partial x^2} + \frac{\partial^2 T}{\partial y^2}\right] + \phi \tag{2.18}$$

2.6 Numerical methods

The equations deduced in the previous section do not admit, except in particular cases, analytical solutions, therefore they are solved numerically to maintain the generality of the solution. This section provides the theoretical foundations for the numerical schemes employed in this thesis and for numerical methods applied to handle non-linearity. The discretization of equations follows the finite difference method [Hirsch, 1988].

2.6.1 Euler numerical schemes for PDEs

The most general energy balance equation for this work, namely equation 2.12, is a partial differential equation (PDE) as the variable T depends on both spatial coordinates and time. If this equation is discretized in space, it becomes an ordinary differential equation (ODE) [Hirsch, 1988], having the following general expression:

$$\frac{\partial T}{\partial t} = f(T, \rho(T), c^*(T), k(T), \Delta x, \Delta y, \Delta z, \phi) \tag{2.19}$$

where $\Delta x, \Delta y$ and Δz correspond to the grid sizes in the x-direction, y-direction, and z-direction respectively. For ODEs there are several numerical schemes. In this work, essentially two numerical schemes are employed, explicit

Euler scheme and implicit Euler scheme. The explicit Euler scheme, also known as forward Euler (FE), consists in discretizing the left-hand side term of equation 2.19 in time between the current time step $m+1$ and the previous one m and evaluating the right-hand side term at the previous time step m, namely:

$$\frac{T^{m+1} - T^m}{\Delta t} = f(T^m, \rho(T^m), c^*(T^m), k(T^m), \Delta x, \Delta y, \Delta z, \phi) \tag{2.20}$$

On the other hand, the implicit Euler scheme, also known as backward Euler (BE), consists of evaluating the right-hand side at the time step $m+1$.

$$\frac{T^{m+1} - T^m}{\Delta t} = f(T^{m+1}, \rho(T^{m+1}), c^*(T^{m+1}), k(T^{m+1}), \Delta x, \Delta y, \Delta z, \phi) \tag{2.21}$$

In both cases, the numerical discretization in space is performed with centered finite differences, which have a second order of accuracy, meaning that for a reduction of the grid size of one order of magnitude there is a reduction of the discretization error of two orders of magnitude. The discretization in time is instead, in both cases, of the first order. Therefore, both explicit and implicit Euler methods are first-order accurate in time and second-order accurate in space. FE method has the disadvantage of requiring a criterion for numerical stability [Hirsch, 1988]. The stability limit, in the case of constant properties and 1D simplification, is:

$$\Delta t \leq \frac{1}{2}\frac{\Delta x^2}{\alpha} \tag{2.22}$$

where α is the thermal diffusivity, while in the case of 2D simplification is:

$$\Delta t \leq \frac{1}{\alpha \cdot \left(\frac{1}{\Delta x^2} + \frac{1}{\Delta y^2}\right)} \tag{2.23}$$

The consequence of the stability limit is that finer grid sizes imply smaller time steps, which can be very small compared to the typical timescales of interest, thus requiring a greater number of computations. Conversely, the BE method is "unconditionally stable", meaning that there is no stability limit, therefore the grid size and the time step can be independently chosen. However, FE scheme is much more straightforward to implement than BE, as the latter involves solving a linear system of equations by performing matrix inversions, thus increasing the computational cost.

2.6.2 Methods for non-linear equations

The presence of temperature-dependent properties renders the energy balance equation non-linear, therefore when equations are discretized a system of non-linear equations has to be solved for each time step. There are several methods available in the literature to handle non-linearity, and in this thesis two of them are employed: Newton's method [Hirsch, 1988] and the frozen-coefficients (FC) method [Kachanov, 1959]. Newton's method is iterative, meaning that the algorithm is applied until a set tolerance is reached (for each time step) and is one of the fastest iterative methods, albeit not straightforward to implement, while the FC method is a simplified method consisting in evaluating the thermal properties at the previous time step (m) instead of the current one ($m+1$). In this way, the problem is linearized and there is no need to solve a system of non-linear equations, therefore it is ideal from the computational cost standpoint with respect to Newton's method. The FC method introduces an error in the computation, which depends on the sensitivity of the thermal properties with the temperature. For this reason, both methods are implemented in this work and compared in terms of accuracy and computational cost. Solving equations for temperature-dependent properties yields more accurate solutions at the expense of the computational cost.

Chapter 3

Methodology

In the framework of the FWHLC, as mentioned in section 1.2, this thesis has the specific goal of developing a control-oriented thermal model for its design and RT operation in the AFP phase. In particular, the thermal model is developed with the objective of being a trade-off between accuracy and computational cost for it to be suitable for RT application. Furthermore, this thesis has the specific goal of developing an additional simple and reliable thermal model to generate temperature maps for IR cameras' synthetic diagnostics in the DT phase. This chapter describes the methodology followed in order to answer the research questions stated in section 1.4.

The features for the first model of being control-oriented and for the second model of being simpler than the 3D simulations already available imply in both cases the necessity of narrowing down models' complexity through simplifying assumptions. Therefore, the rationale of this work is to start with the simplest model possible, then benchmark the results with more accurate models (provided the lack of experimental results) and, in the case of insufficient accuracy, adding complexity to the original model. This approach of progressively increasing the complexity of the model allows on the one hand to gradually verify the model's underlying assumptions, and on the other hand to find a simple model without dramatically losing the accuracy of the solution. Figure 3.1 depicts the methodology followed in order to fulfill the thesis' aim and answer to the research questions reported in section 1.4. The flowchart is divided into two parts reflecting the thermal models developed: a thermal model for the design and RT operation of the FWHLC in the AFP phase, and a thermal model for IR cameras' synthetic diagnostics in the DT phase.

Concerning the first one, currently, it is still unclear whether ITER FW will be entirely covered by TFW panels during the AFP phase or by a mix of TFW, EHF, and NHF panels. However, even in the case of EHF and NHF panels' installation, the current proposal is to avoid having active cooling in order to minimize the risk of losing coolant in accidental cases. Therefore the thermal model developed encompasses the possibility of having all three types of panels following the flexibility requirement. Additionally, according to the requirement of having a general model stated in section 1.2, the thermal model can be applied to any FWP. Therefore, for a given FWP design (and FWP type), there is first a part of model design and validation, after which the thermal model is ready to be integrated into the PCS and used to investigate the thermal response of the FW. Specifically, the model design and validation part is structured in a thermal modelling part, a comparative assessment, and a convergence analysis. Regarding the thermal modelling, different time-dependent models of increasing complexity are developed: a 0D model, a 1D semi-infinite model, a 1D model, and a 2D model having a rectangular grid. In particular, the 2D simplification with a rectangular grid is deemed to be the maximum complexity acceptable for a control-oriented model. Initially, in order to reduce the variables into play and without lacking generality, an artificial constant heat load corresponding to the maximum value allowed for the specific panel type is employed. For both 1D and 2D models, constant properties and variable properties (temperature dependent) are investigated. Additionally, in the case of variable properties, two different methods are employed to handle the non-linearity, the FC method and Newton's method. The thermal modelling is done in MATLAB and the discretization is performed with finite difference (FD) schemes, which provide a simple and versatile approach, thus respecting the flexibility requirement. For the same reason, codes are written from scratch in MATLAB without using external libraries. After the thermal modelling, a comparative assessment is carried out, comparing:

- the 2D model with a rectangular grid with more accurate simulations obtained using higher fidelity models providing the ground truth
- the 1D model with the 2D model

- constant properties with variable properties approximations (both FC and Newton's methods)

The comparative assessment allows in this way to test the assumptions of 2D with a rectangular grid simplification, 1D simplification, constant properties, and FC method respectively. Specifically, as the 2D model is the most accurate amongst the models developed, the validity of the 2D simplification with rectangular grid is assessed through a benchmark with more accurate models developed not for control purposes from third parties in Ansys and Python (called "2D validation" in the figure). The comparative assessment allows to find the most representative control-oriented thermal model depending on the type of FWP, namely a model capable of computing the thermal response of FWPs with sufficient accuracy while being as simple as possible at the same time. Once a representative model is identified, a convergence analysis is performed in order to find a reasonable grid size and time step so that the model is compliant with RT requirements. Because of its excessive simplification, the 1D semi-infinite model is not considered a representative model, but instead, it is useful for the convergence analysis to find a reasonable first-guess grid size. At this point, a systematic approach to identify the most suitable control-oriented model in terms of a trade-off between accuracy and computational cost for the design and RT operation of the FWHLC in the AFP phase for each FWP design and type has been provided. The final part is the integration in the PCS, which requires respecting the formalism of the PCSSP in Simulink, after which the thermal models developed are finally applied using realistic time-dependent heat loads in order to investigate the thermal response of the FW in the AFP phase. The advantage of coding in MATLAB is that the integration with Simulink is facilitated.

Concerning the model for IR cameras' diagnostics, unlike the AFP phase, in the DT phase, there will exclusively be NHF and EHF panels. The thermal model, developed in steady-state conditions, reads the thermal flux data from the SMITER code, evaluates the surface temperature map for every FWP, and loads the temperature data back to SMITER. Therefore, these data can be used as a benchmark with the measurements of the IR cameras during the flat-top phase (as this model is limited to steady-state conditions) in DT operation. In this case, there is no need to address a representative model, as this is already done for the AFP phase. Indeed, the model developed for the AFP phase, being time-dependent, is more general than the one needed for the DT phase (steady-state conditions are just a particular case of transient conditions), thus the same representative model can be employed without lacking validity.

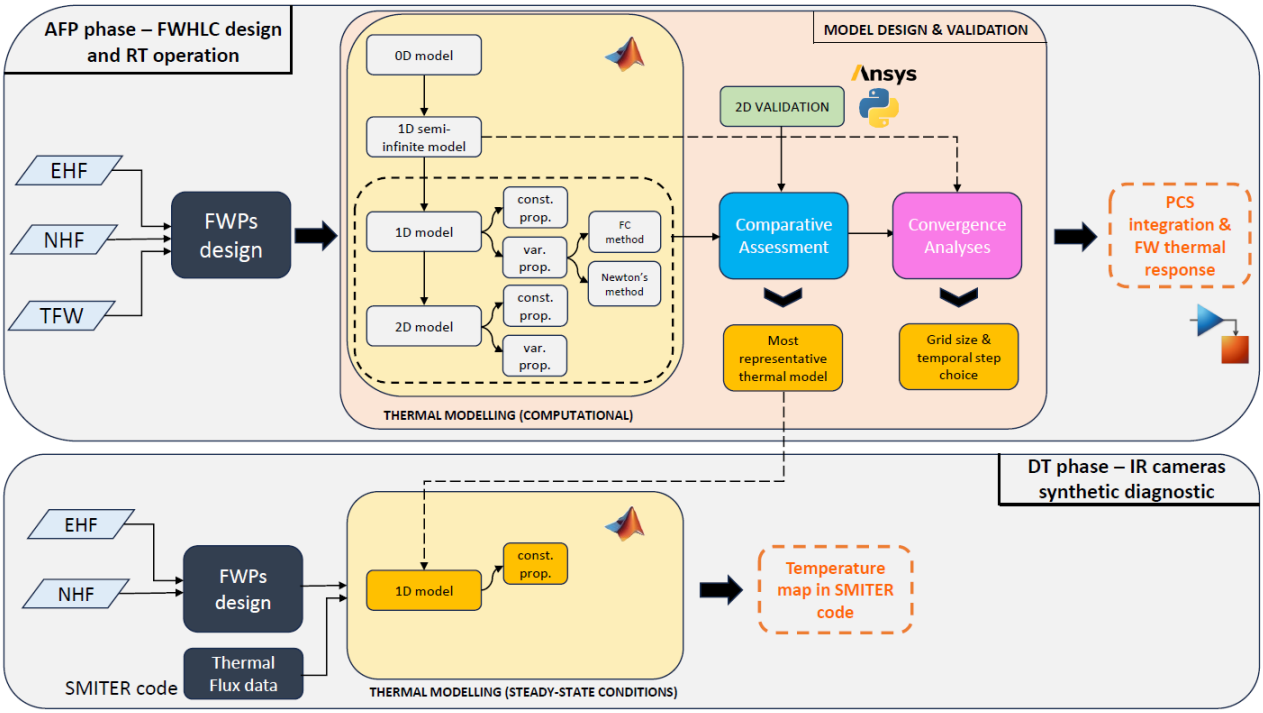

Figure 3.1: Methodology flowchart.

The next two sections are dedicated to the details of the thermal modelling for the design and RT operation of the FWHLC in the AFP phase and IR cameras' synthetic diagnostics in the DT phase respectively. Both sections start with presenting the underlying model assumptions, followed by their mathematical derivation. Specifically, for the design and RT operation of the FWHLC in the AFP phase part, the order in which the thermal models developed are

presented follows the logic of increasing model complexity as shown in figure 3.1. The application and the results of the models developed are then presented and discussed in chapter 4.

3.1 Thermal modelling in the AFP phase - FWHLC design and RT operation

3.1.1 Assumptions

In order to narrow down the complexity of the study, one of the most important assumptions of this work is considering the fingers of FWPs to be thermally isolated. As a consequence, the thermal models are developed for individual fingers of any FWP of any type. This assumption is supported by the fact that, as mentioned in section 2.2.1, fingers are mechanically separated. An individual finger in a given FWP can be identified by defining a local frame of reference for the specific FWP having the following coordinates as represented in figure 3.2: ϕ (toroidal direction), θ (poloidal direction), and x (FWP depth). While the heat flux considerably varies along the poloidal direction along the entire FWP, its variation along the poloidal direction when looking at an individual finger is instead much lower. The direct consequence is that higher thermal gradients are expected in the toroidal direction (where the heat flux is suddenly interrupted) and in the x direction than in the poloidal one. That being the case, as the goal is developing a control-oriented model (which inherently involves a reduced complexity, thus a reduced computational cost), another fundamental assumption is that the heat transfer along the poloidal direction of a finger is not considered, and only the toroidal direction and x direction are taken into account. In other words, a simplification from 3D heat transfer to 2D in an individual finger is carried out. Thermal fluxes are then considered to be uniform in the poloidal direction and distributed along the toroidal direction of the given finger, as depicted in figure 3.3. Subsequently, the complexity is further narrowed down by assuming a rectangular computational grid for the 2D model in order to employ finite differences in a simple way, thus ignoring the toroidal curvature. Figure 3.2 shows the sketch of the computational grid of interest. It is important to underline that the presence of design details such as the finger's leading edges is neglected. These elements play a crucial role in FWPs design as magnetic field lines' incidence angle is locally increased thus increasing the local heat load [Mitteau et al., 2017]. Therefore, this assumption is deemed reasonable as the model is developed for control purposes rather than for design purposes. Additionally, once a final FWPs design is established, one can think of adding correcting factors in order to take into account the temperature peaks due to leading edges. Another relevant feature of fingers belonging to EHF and NHF panels is the presence of castellations, because of which not only magnetic field lines' incidence angle is locally increased due to poloidal and toroidal gaps thus increasing the local heat load but also the heat diffusion in the toroidal direction is interrupted. However, concerning the aspect of local increased heat load, similarly to leading edges, this is mostly related to design purposes rather than to control purposes. Concerning the aspect of the interruption of heat diffusion in the toroidal direction, for EHF and NHF panels the thermal gradient is expected to be predominant in the x direction rather than in the toroidal direction because of the heat transfer with the coolant, therefore the presence of castellations is not expected to play a significant role and hence is neglected. Additional design details are neglected for the sake of reducing model complexity. Moreover, as in the AFP phase temperatures are relatively low for fusion reactions to happen, there is no volumetric heat generation in the materials as no neutrons are produced. Furthermore, the phenomenon of melting is not involved in the modelling, as it is expected to take place in the case of accidental situations (in which the RACLETTE code, as stated in section 1.1, is particularly suitable), while this model is developed with the objective of FW protection, thus actuators should intervene before melting becomes relevant. Additionally, the phenomenon of sputtering is neglected. Finally, also the presence of vapour shielding is neglected, which is a phenomenon thanks to which the heat load onto the FW is mitigated, therefore this is a conservative assumption [Raffray and Federici, 1997].

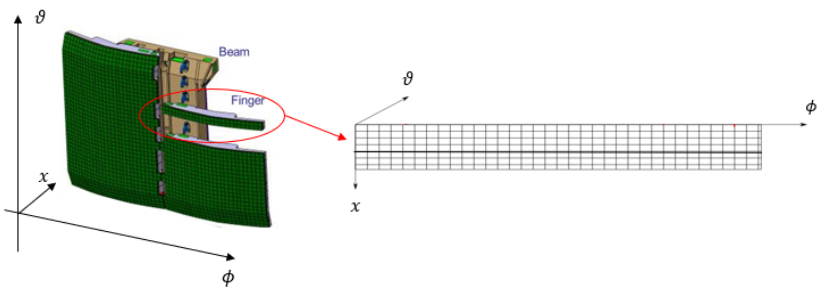

Figure 3.2: Scheme of a generic FWP's finger and computational grid employed. Adapted from [Brank et al., 2019].

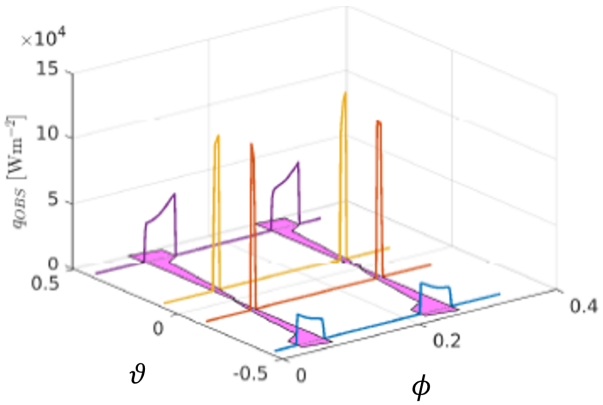

Figure 3.3: Example of the typical heat flux profile along the toroidal direction on selected fingers for a given FWP, which may change in magnitude in time and change spatially [Pesamosca et al., 2023]. Note that the heat flux is significant in the wetted area only (in magenta).

Fingers' geometric measures are taken thanks to CAD models from the Blanket Section. Specifically, the length of the computational grid in the ϕ direction corresponds to a single finger's toroidal length, while the thickness in the x direction, which depends on the type of FWP, is taken as shown in figure 3.4. Basically, the materials involved are W (armour tiles) and CuCrZr or SS for the underneath layer (CuCrZr for NHF and EHF panels, SS for TFW panels). In all the cases, the thermal resistance between the materials is neglected. Geometric measures employed are summed up in tables 3.1 and 3.2.

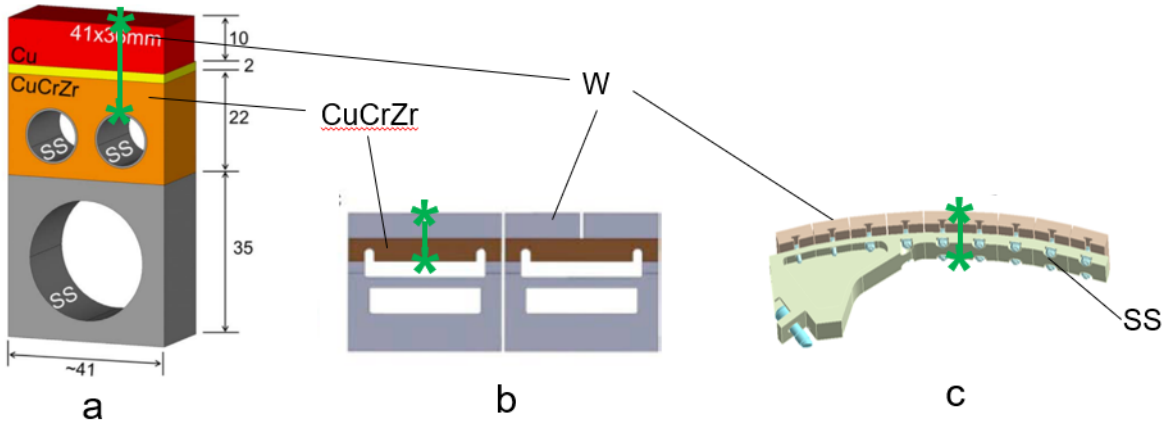

Figure 3.4: Thickness along the x direction considered for NHF (a), EHF (b), TFW (c) panels respectively. Adapted from [Perez-Pichel et al., 2017], [Mazul et al., 2012], and [Hunt, 2023] respectively. Note that in the case of NHF panels, the thin Cu layer is neglected for the sake of model simplification.

		FWP type		
		NHF	EHF	TFW
Length x direction [mm]	W layer	10	7	15
	CuCrZr/SS layer	7	4	20

Table 3.1: Geometric measures in the x direction for each FWP type.

	FWP type		
	NHF	EHF	TFW
Length ϕ direction [m]	0.69	0.64	0.66

Table 3.2: Geometric measures in the ϕ direction for each FWP type.

3.1.2 State-space formulation

Before addressing the details of the thermal models developed, it is important to underline that those thermal models involving a discretization are expressed using a state-space formulation. This formulation is widely employed in control system theory. Indeed, among the thermal models developed for control purposes cited in section, 1.1, [Valcárcel et al., 2014] and [Anand et al., 2021] employ a state-space formulation with explicit schemes assuming constant coefficients (therefore matrices $\underline{\underline{A}}$, $\underline{\underline{B}}$, $\underline{\underline{C}}$, and $\underline{\underline{D}}$ are constant). This present work extends this approach by applying an implicit scheme and variable properties. The advantage of using a state-space representation is to facilitate the implementation in Simulink and consequently the integration in the PCSSP, which is indeed designed in Simulink. The most general representation of a discrete state-space representation discretized with an explicit scheme having n state variables and evaluated at the time $m+1$ is the following:

$$\begin{aligned} \underline{x}^{m+1} &= \underline{\underline{A}}(\underline{x}^m)\underline{x}^m + \underline{\underline{B}}(\underline{x}^m)\underline{u}^m \\ \underline{y}^{m+1} &= \underline{\underline{C}}(\underline{x}^m)\underline{x}^m + \underline{\underline{D}}(\underline{x}^m)\underline{u}^m \end{aligned} \tag{3.1}$$

where $\underline{x}^{m+1}$ is the state vector with n states, y^{m+1} the output vector with n states, $\underline{u}^m$ the input vector, $\underline{\underline{A}}(\underline{x}^m)$ the nXn state matrix, $\underline{\underline{B}}(\underline{x}^m)$ the input matrix, $\underline{\underline{C}}(\underline{x}^m)$ the output matrix, and $\underline{\underline{D}}(\underline{x}^m)$ the feedforward matrix. Specifically, in the thermal models employed in this work, the state vector corresponds to the temperature distribution at time $m+1$, the output vector to the surface temperature distribution at time $m+1$, the input vector to the incident heat flux distribution on a finger and to the heat transfer to the surrounding environment, while the state matrix describes the diffusion process. In the case of an implicit discretization, right-hand side terms are evaluated at time $m+1$, therefore the general representation is the following:

$$\begin{aligned} \underline{x}^{m+1} &= \underline{\underline{A}}(\underline{x}^{m+1})\underline{x}^m + \underline{\underline{B}}(\underline{x}^{m+1})\underline{u}^{m+1} \\ \underline{y}^{m+1} &= \underline{\underline{C}}(\underline{x}^{m+1})\underline{x}^m + \underline{\underline{D}}(\underline{x}^{m+1})\underline{u}^{m+1} \end{aligned} \tag{3.2}$$

Note that the formulation of matrices $\underline{\underline{A}}$, $\underline{\underline{B}}$, $\underline{\underline{C}}$, and $\underline{\underline{D}}$ changes going from an explicit to an implicit discretization of the same system. However, for the sake of keeping the notation as general as possible, matrices in the state-space representation are always referred to as $\underline{\underline{A}}$, $\underline{\underline{B}}$, $\underline{\underline{C}}$, and $\underline{\underline{D}}$ but their formulation changes according to the specific system under study and the specific discretization. Moreover, in the case of constant properties, the matrices do not depend on the values of the state vector.

3.1.3 0D model

The simplest heat transfer model is a 0D model, also known as "lumped capacitance method" [Çengel and Ghajar, 2020]. In the 0D approximation, the temperature in a solid body is assumed to be uniform in space and vary exclusively in time. If the solid body of interest is cooled down or heated up by convection heat transfer, then the dimensionless Biot number B_i number can be defined:

$$B_i = \frac{h \cdot L_c}{k} \tag{3.3}$$

where h is the heat transfer coefficient (HTC), L_c a characteristic length, and k the thermal conductivity. The validity of the 0D approximation can be determined according to this rule of thumb:

- if $B_i \gg 0.1$ thermal gradients inside the material are quite relevant, so a 0D model would be highly inaccurate
- if $B_i < 0.1$ employing a 0D model is a good approximation

The situation in which the solid body is exclusively subjected to convective heat transfer is referred to as "classical lumped capacitance method". This method can be generalized in order to take into account also radiation heat transfer, incident heat flux, and volumetric heat generation [Bergman et al., 2011]. However, while in the classical lumped capacitance method the Biot number is the only relevant parameter for assessing the validity of the 0D approximation, in the generalized method also incident heat flux and volumetric heat generation may play a significant role, therefore the verification of the previous rule of thumb is not sufficient. Therefore, if one wants to rigorously apply the generalized lumped capacitance method, further studies investigating the impact of incident heat flux and volumetric heat generation are needed. Alternatively, it is possible to apply enhanced 0D models present in the literature which, despite being analytically more complex, extend the validity of the 0D approximation to heat transfer problems that are not interested by heat convection only (and to situations of high Biot number as well). For instance, [Sahu and Behera, 2012] proposed an enhanced lumped capacitance method by employing a polynomial approximation, concluding that the uniform time-dependent temperature distribution depends on Biot number, incident heat flux and volumetric heat generation parameters, and time. The application of the 0D model is discussed in section 4.1.1.

3.1.4 1D semi-infinite model

The first model consists of considering the heat transfer along the x direction of a finger with the approximation of modeling only the W layer, where high thermal gradients are expected. This 1D homogeneous model is schematically depicted in figure 3.5.

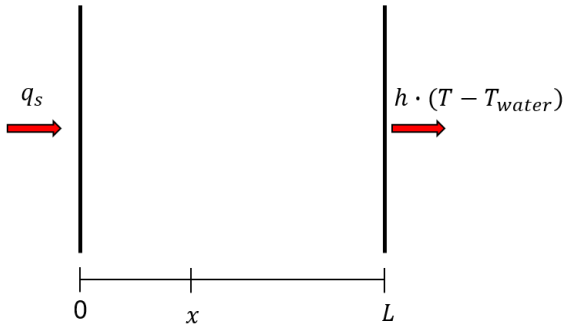

Figure 3.5: Schematic representation of 1D homogeneous heat transfer model. In this figure, q_s is the incident heat flux, h is the heat transfer coefficient, and T_{water} is the coolant temperature.

In order to narrow down the complexity, a 1D semi-infinite model is first implemented. In the 1D semi-infinite model it is assumed that $L \to \infty$ and, assuming constant thermal properties, equation 2.15 can be applied for the energy conservation. It can be shown that, with the additional assumptions of constant heat flux q_s and absence of volumetric heat generation, the equation admits an analytical solution, namely:

$$T(x,t) = T_{in} + \frac{q_s}{k} \cdot \left[\sqrt{\frac{4\alpha t}{\pi}} \cdot exp\left(\frac{-x^2}{4\alpha t}\right) - x \cdot erfc\left(\frac{x}{\sqrt{4\alpha t}}\right) \right] \tag{3.4}$$

with T_{in} being the initial temperature, α the thermal diffusivity, and $erfc$ the error function [Maurizio, 2020]. This model is particularly useful when the heat deposition time is much smaller than the typical timescales for heat diffusion in the material [Çengel and Ghajar, 2020]. In this case, indeed, relatively high thermal gradients occur close to the surface facing the heat flux, while the temperature is basically undisturbed far from the surface.

In order to understand if a 1D semi-infinite model is a good approximation, this model is compared with a simplified 1D model, in which it is assumed an adiabatic boundary condition for $x = L$ (with reference to figure 3.6) and a homogeneous material in this case too. It is expected these two models to yield the same results at the beginning of the heat transfer process, in which the temperature is almost undisturbed far from the surface. In this case, indeed, the thermal gradient far from the surface is relatively low, therefore imposing an adiabatic condition is consistent with the 1D semi-infinite model assumption. However, due to heat diffusion, it is expected that at a certain time t^* the temperature far from the surface is not undisturbed anymore and therefore the two models start to yield different results. In order words, for $t > t^*$ the underlying assumption of very rapid thermal fluxes does not hold anymore, hence the 1D semi-infinite model is not valid. Note that t^* depends on the value of L: a lower slab length implies

lower t^* because the heat diffusion process is more rapid (less heat capacity available). Essentially, the 1D semi-infinite approximation is valid if the time t^* is higher than typical heat deposition times on ITER FW for the given finger's dimensions in the x direction.

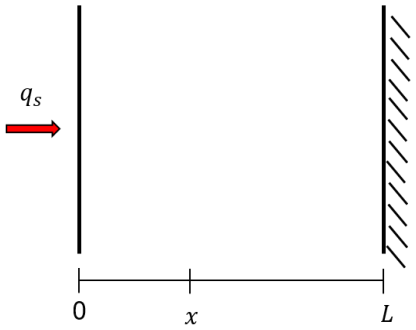

Figure 3.6: Schematic representation of 1D simplified heat transfer model.

The 1D simplified model is solved numerically by using a FE discretization scheme. With the assumption of constant properties, the energy conservation equation 2.15 can be discretized with centered differences in space around a generic node i at the time step m as follows:

$$\rho c \frac{T_i^{m+1} - T_i^m}{\Delta t} = k \cdot \frac{T_{i-1}^m - 2T_i^m + T_{i+1}^m}{\Delta x^2} \tag{3.5}$$

where Δt and Δx are the fixed time step and the grid size respectively. The above expression can be applied to the domain shown in figure 3.6 (to all the n nodes) together with the boundary condition of imposed heat flux for $x = 0$ and the adiabatic boundary condition for $x = L$, thus yielding the following expression in state-space:

$$\underbrace{\begin{pmatrix} T_1 \\ T_2 \\ \vdots \\ \\ \\ \\ T_{end} \end{pmatrix}^{m+1}}_{\underline{T}^{m+1}} = \underbrace{\begin{pmatrix} 1-a & a & 0 & \cdots & \cdots & \cdots & 0 \\ a & 1-2a & a & 0 & \cdots & \cdots & 0 \\ 0 & \ddots & \ddots & \ddots & 0 & \cdots & 0 \\ \vdots & 0 & \ddots & \ddots & \ddots & \vdots & \\ \vdots & & & & & & \\ & & & & & & \\ 0 & \cdots & & & & a & 1-a \end{pmatrix}}_{\underline{\underline{A}}} \cdot \underbrace{\begin{pmatrix} T_1 \\ T_2 \\ \vdots \\ \\ \\ T_{end-1} \\ T_{end} \end{pmatrix}^{m}}_{\underline{T}^{m}} + \underbrace{\begin{pmatrix} \frac{\Delta t}{\rho c \Delta x} \\ 0 \\ \vdots \\ \\ \\ \\ 0 \end{pmatrix} \cdot q_s}_{\underline{\underline{B}}}$$

$$\underline{u}^m = [q_s]_{1X1} \qquad \underline{\underline{C}} = [1, 0, ..., 0]_{1Xn} \qquad \underline{\underline{D}} = [0]_{1X1} \tag{3.6}$$

where $a = \frac{\alpha \Delta t}{\Delta x^2}$. The full derivation is provided in Appendix B.1. It is important to underline that, as mentioned in section 2.6, in the case of FE method the stability limit has to be respected.

When comparing the 1D semi-infinite model with the 1D simplified model, if the final time of the simulation is fixed, there is a source of error linked to the discretization of the 1D simplified model scheme, and another error linked to the length of the domain used. Indeed, as mentioned above, at a given time the lower the slab length is, the higher the difference between the two models is. Therefore, in order to isolate the first source of error from the second one, the length of the slab is set to be 100 mm, one order of magnitude larger than the typical values for FWPs. In this way, the two models should yield approximately the same solution during the simulation time, and the potential errors committed would exclusively be linked to the discretization error. Because of the discretization error, using a too coarse grid would imply losing information about thermal gradients. Therefore this approach is useful in order to identify a typical grid size in the x direction to avoid losing information about thermal gradients.

Given the fact that the 1D semi-infinite model is applied to W only (which is common to every type of FWP), and to an arbitrarily long slab, this model does not depend on the type of FWP. The results of this comparison are shown in section 4.1.2.

3.1.5 1D model

A more complex and accurate model is a bi-layer 1D model along the x-direction, whose domain is schematically depicted in 3.7. The geometric quantities L_W and L_{tot} depend on the type of FWP. Moreover, the layer besides the W one can be made of CuCrZr or SS depending on if the FWP considered is a NHF/EHF or TFW respectively.

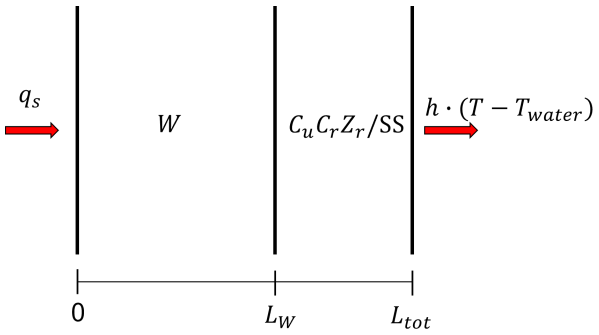

Figure 3.7: Schematic representation of 1D bi-layer heat transfer model.
Note that CuCrZr is employed in the case of NHF and EHF panels, while SS in the case of TFW panels.

In the above figure, q_s is the incident heat flux which may potentially vary in time, h is the HTC, and T_{water} is the temperature of the coolant.

The HTC in the case of NHF and EHF panels is quite straightforward to evaluate, as it depends on the coolant flow regime exclusively. In order to narrow down the complexity of the study, the HTC is considered to be constant without employing any correlation to determine it. Instead, a reasonable fixed value is chosen. On top of that, also the coolant temperature T_{water} is considered to be constant. From this standpoint, more accurate models are needed to assess the coupling between the FWP and the coolant, especially in order to include nucleate boiling and avoid reaching the boiling crisis [Bergman et al., 2011]. Conversely, in the case of TFW panels, the cooling process is inertial, meaning that the panel is not actively cooled. Therefore, these panels can cool down by transferring heat to the surrounding structures for diffusion or thermal radiation. In order to take this phenomenon into account, an equivalent HTC h_{eq} can be defined. In this way, the domain depicted in figure 3.7 can be generalized to TFW panels as well. The equivalent HTC is determined through a 0D approximation as described in section 4.1.1.

The transient is solved numerically by using a backward Euler discretization scheme. With the assumption of constant properties, the energy conservation equation 2.15 can be discretized around a generic node i at the time step m as follows:

$$\rho c \frac{T_i^{m+1} - T_i^m}{\Delta t} = k \cdot \frac{T_{i-1}^{m+1} - 2T_i^{m+1} + T_{i+1}^{m+1}}{\Delta x^2} \tag{3.7}$$

This expression is applied to the domain depicted in figure 3.7 together with the boundary conditions of imposed heat flux for $x = 0$ (in which the heat flux is evaluated at the time step $m+1$), heat flux continuity at the interface between the materials, and convective heat transfer to the coolant:

$$\begin{pmatrix} T_1 \\ T_2 \\ \vdots \\ T_{int} \\ \\ \\ T_{end} \end{pmatrix}^{m+1} = \begin{pmatrix} 1 & -1 & 0 & \cdots & \cdots & \cdots & & 0 \\ -a_W & 1+2a_W & -a_W & 0 & \cdots & \cdots & & 0 \\ 0 & \ddots & \ddots & \ddots & 0 & \cdots & & 0 \\ \vdots & 0 & -\frac{k_W}{k} & 1+\frac{k_W}{k} & -1 & 0 & \cdots & 0 \\ \vdots & 0 & \cdots & -a & 1+2a & -a & & \\ 0 & \cdots & & & \ddots & \ddots & \ddots & \\ 0 & \cdots & & & & 0 & -1 & 1+\frac{h\Delta x}{k} \end{pmatrix}^{-1} \cdot \begin{pmatrix} \frac{q_s^{m+1} \cdot \Delta x}{k_W} \\ T_2^m \\ \vdots \\ 0 \\ \\ \\ T_{end-1}^m \\ \frac{h\Delta x T_{water}}{k} \end{pmatrix} \tag{3.8}$$

where $a_W = \frac{\alpha_w \Delta t}{\Delta x^2}$ for tungsten and $a = \frac{\alpha \Delta t}{\Delta x^2}$ for CuCrZr/SS. Note that the above expression is not written in the state-space formulation. Appendix B.2 provides the full derivation of the above expression and the state-space formulation.

In the case of temperature-dependent properties the energy balance equation to consider is equation 2.14. As far as the FC method is concerned, the definition of the matrix is quite similar but its coefficients need to be updated at each time step, therefore it is necessary to perform a matrix inversion at each time step, thus increasing the computational cost. Concerning Newton's method, it is necessary to solve a system of non-linear equations at each time step, which increases the computational cost. Conversely, the advantage of having constant properties is that the matrix inversion can be performed just once before the time loop, at the expense of a lower accuracy in the solution. The discretization with both the FC method and Newton's method is provided in Appendix B.3. The 1D model is applied to EHF, NHF, and TFW panels, and results are discussed in sections 4.1.3, 4.1.4, and 4.1.5 respectively.

3.1.6 2D model

A more accurate model is a 2D model along the x direction and the toroidal direction. The domain is schematically depicted in figure 3.8.

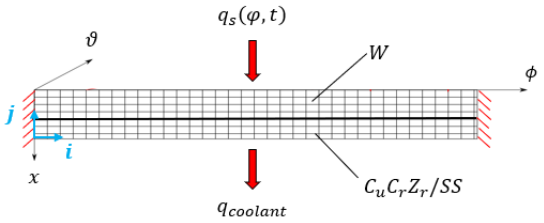

Figure 3.8: Schematic representation of 2D model's domain. i and j are the indexes along the toroidal and the x direction respectively.

The incoming heat flux q_s can vary both in time and in the toroidal direction. With the hypothesis of constant thermal properties, the energy balance equation 2.18 can be discretized as follows with a backward Euler scheme:

$$\rho c \frac{T_{i,j}^{m+1} - T_{i,j}^{m}}{\Delta t} = k \left[\frac{T_{i-1,j}^{m+1} - 2T_{i,j}^{m+1} + T_{i+1,j}^{m+1}}{\Delta \phi^2} + \frac{T_{i,j-1}^{m+1} - 2T_{i,j}^{m+1} + T_{i,j+1}^{m+1}}{\Delta x^2} \right] \tag{3.9}$$

For the sake of convenience, the above expression can be written using another index k defined as follows:

$$\begin{aligned} T_{i,j} &\rightarrow T_k \\ T_{i-1,j} &\rightarrow T_{k-1} \\ T_{i+1,j} &\rightarrow T_{k+1} \\ T_{i,j-1} &\rightarrow T_{k-n_\phi} \\ T_{i,j+1} &\rightarrow T_{k+n_\phi} \end{aligned} \tag{3.10}$$

with $k = 1, ..., n_\phi \cdot n_x$. Therefore, equation 3.9 can be written as:

$$\rho c \frac{T_{k}^{m+1} - T_{k}^{m}}{\Delta t} = k \left[\frac{T_{k-1}^{m+1} - 2T_{k}^{m+1} + T_{k+1}^{m+1}}{\Delta \phi^2} + \frac{T_{k-n_\phi}^{m+1} - 2T_{k}^{m+1} + T_{k+n_\phi}^{m+1}}{\Delta x^2} \right] \tag{3.11}$$

By applying this equation to the domain in figure 3.8, a pentadiagonal matrix of dimensions $n_\phi \cdot n_x \times n_\phi \cdot n_x$ is obtained, having $(n_\phi \cdot n_x)$ elements on the main diagonal, $(n_\phi \cdot n_x) - 1$ elements on the inferior and superior diagonals, $(n_\phi \cdot n_x) - n_\phi$ elements on the n_ϕ-th inferior diagonal and on the n_ϕ-th superior diagonal. More precisely, the above equation is applied to the inner nodes, namely those nodes not belonging to interfaces. As a result, by employing the single underlining as a symbol of a vector and the double underlining as a symbol of a matrix, the above expression can be written as:

$$\underline{T}^{m+1} = \underline{T}^{m} + \frac{\Delta tk}{\rho c} \cdot \underline{\underline{P}} \cdot \underline{T}^{m+1}$$
$$\iff \left(\underline{\underline{I}} - \frac{\Delta tk}{\rho c} \cdot \underline{\underline{P}}\right) \cdot \underline{T}^{m+1} = \underline{T}^{m} \tag{3.12}$$

where $\underline{\underline{P}}$ is the pentadiagonal matrix, and $\underline{\underline{I}}$ the identity matrix. By the defining a new matrix $\underline{\underline{L}} = \left(\underline{\underline{I}} - \frac{\Delta tk}{\rho c} \cdot \underline{\underline{P}}\right)$, the temperature distribution at the time step $m+1$ can be found by performing a matrix inversion:

$$\underline{T}^{m+1} = \underline{\underline{L}}^{-1} \cdot \underline{T}^{m} \tag{3.13}$$

Boundary conditions can be formulated for matrix $\underline{\underline{L}}$. Their definition, as well as the state-space formulation, are described in Appendix C.1.

In the case of variable thermal properties, the energy equation to solve is 2.17. In the case of the FC method, the definition of the matrix is quite similar but its coefficients need to be updated at each time step, therefore it is necessary to perform a matrix inversion at each time step, thus increasing the computational cost. Further details about the discretization are provided in Appendix C.2. The 2D model is applied to EHF, NHF, and TFW panels, and results are discussed in sections 4.1.3, 4.1.4, and 4.1.5 respectively.

3.2 Thermal modelling in DT phase - IR cameras' synthetic diagnostics

3.2.1 Assumptions

Contrarily to section 3.1.1, the thermal model is developed for NHF and EHF panels only, as they are the only panels employed in the DT phase. Additionally, the solution is computed under the assumptions of constant thermal properties and steady-state. As a consequence, heat fluxes on FWPs have a similar distribution as depicted in figure 3.3, with the difference that the heat load is constant in time, which is considered generally the case during the flat-top and in absence of transient auxiliary heating. As in section 3.1.1, fingers are considered to be thermally isolated from each other. On top of that, only the x direction is considered because, as it will be demonstrated in section 4.1.4, a 1D thermal model (with constant properties) accurately describes the heat transfer phenomena in actively cooled panels. Also in this model, the presence of castellations is neglected. Finally, unlike in the AFP phase, in the DT phase fusion reactions are expected to take place, therefore in the energy balance equation volumetric heat generation must be taken into account. As reported by [Zhang et al., 2011], the heat deposited by neutrons decreases with the penetrated depth in the material. However, for the sake of simplicity, the volumetric heat generation, which depends on the specific material, is considered to be homogeneous. This conservative assumption is justified by the fact that, as it will be subsequently shown in section 4.2, the influence of volumetric heat generation is less impactful on the temperature distribution than that of the heat flux deposited on the surface. Finally, as this study is carried out in nominal conditions, melting is not involved in the modelling, while sputtering is neglected as it is not expected to play a significant role.

3.2.2 Analytical solution

Figure 3.9 qualitatively depicts the domain of interest.

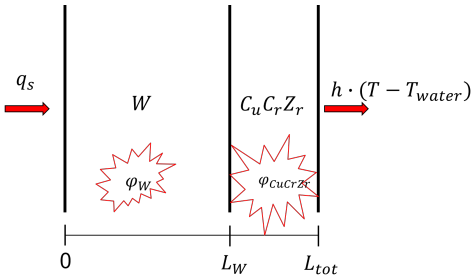

Figure 3.9: Schematic representation of 1D bi-layer heat transfer model in steady state conditions with volumetric heat generation. Note that q_s is constant in time.

Given the assumptions mentioned above, the energy balance equation to solve is 2.15 with the addition of the left-hand side being zero. This equation admits an analytical solution. In particular, as the thermal model aims to evaluate the temperature maps needed for IR cameras' synthetic diagnostics, it is sufficient to evaluate the surface temperature, which has the following expression:

$$T_{surf} = \frac{\phi_W L_W^2}{2k_W} + \frac{q_s}{k_W} L_W + \frac{\phi_{CuCrZr} L_{CuCrZr} - k_{CuCrZr} \cdot \left(-\frac{\phi_W \cdot L_W}{k_{CuCrZr}} - \frac{q_s}{k_{CuCrZr}} \right)}{h} + \frac{\phi_{CuCrZr} L_{CuCrZr}^2}{2k_{CuCrZr}} - L_{CuCrZr} \cdot \left(-\frac{\phi_W \cdot L_W}{k_{CuCrZr}} - \frac{q_s}{k_{CuCrZr}} \right) + T_{water} \tag{3.14}$$

The full derivation is provided in Appendix D.

The volumetric heat generation in the C_uC_rZr layer is assumed to be $\phi_{CuCrZr} = 10$ MW/m^3 [Zhang et al., 2011]. Concerning the heat generation in the W layer, no data have been found in the literature. Therefore, this value has been calculated by making the conservative assumption that all the neutrons scattered by the interaction with W atoms release all their carrying energy. This assumption is conservative because there can be several types of particle impacts (e.g., elastic, inelastic) in which the energy transferred by neutrons to W atoms is only a part of their carrying energy. Specifically, the volumetric heat can be estimated as:

$$\phi_W = E \cdot R \tag{3.15}$$

where E is the energy carried by neutrons (i.e., 14.1 MeV for the D-T reaction, see section 2.1) and R is the reaction rate. The reaction rate can be expressed as $R = \sigma \cdot N_{AV} \cdot \frac{\rho_W}{M_W} \cdot N$, where σ is the scattering microscopic cross section (assumed to be $5 \cdot 10^{-24}$ cm^2 [National Nuclear Data Center, 2024]), N_{AV} is Avogadro's number, ρ_W and M_W are the density and molar mass of tungsten respectively, and N is the neutron flux (assumed to be $0.45 \cdot 10^{14}$ 1/(s $\cdot$ cm^2) [ITER, 2007]). As a result, $\phi_W = 32$ MW/m^3.

Chapter 4

Results and discussion

This chapter is dedicated to presenting the results of the thermal modelling. The chapter reflects the structure presented in the methodology flowchart (figure 3.1), therefore the first section is relative to the design and RT operation of the FWHLC in the AFP phase and the second section is relative to IR cameras' synthetic diagnostics in DT phase.

4.1 AFP phase - FWHLC in RT

This section presents the results of the thermal models developed in an order that reflects the logic of increasing model complexity, coherently with the methodology flowchart structure. Initially, the 0D and 1D semi-infinite models, which do not depend on the type of FWP, are presented, followed by 1D and 2D models for EHF, NHF, and TFW panels respectively (1D and 2D models are instead specific for the type of FWP). After a sum-up of the main results of comparative assessments and convergence analyses, the thermal models developed are applied using realistic heat load data. Subsequently, further insights about model reduction techniques and comparison between explicit and implicit Euler schemes are presented. It is important to underline that, to have precise estimations of computational times, simulations should be performed in a dedicated RT framework. However, as this has not been possible during this thesis work, simulations have been performed using ITER computing cluster [ITER Computing Cluster, n.d.], for which it is not straightforward to define the computational time in a deterministic way as it depends on the cluster's load at the moment the simulation is performed. Therefore, simulations are repeated for 100 times and a statistical distribution of computational times is provided. In this work, the approach described is deemed to be sufficient to draw meaningful conclusions and simulations' replication in a dedicated RT framework is left for further studies.

4.1.1 0D model

Heat transfer phenomena occurring in FWP fingers (of any type) are essentially incident heat flux on their surface exposed to the plasma and convective heat transfer with the coolant. That being the case, the classical lumped capacitance method, which assumes the presence of convective heat transfer only, can not be directly applied, but instead a generalized lumped capacitance method is more appropriate. As pointed out in section 3.1.3, the applicability of this generalized method, besides the verification of the Biot number, is limited by the prior investigation of the impact of the incident heat flux on thermal gradients. As mentioned earlier, an alternative is employing the enhanced 0D models present in the literature (for instance the one developed by [Sahu and Behera, 2012]), which however have the limitation of being analytically more complex and therefore not straightforward from the implementation standpoint. Because of these limitations, it is deemed reasonable to directly choose more accurate models than the 0D approximation, i.e., a 1D semi-infinite model. This approach is supported by the fact that, if the 1D semi-infinite model turns out to be inaccurate, the 0D is inaccurate as a consequence of having a poorer level of approximation.

Among the heat transfer phenomena analyzed, the only case in which the underlying assumptions of the classical lumped capacitance method are respected is during the cooling phase of TFW panels. Indeed, TFW panels, even if not actively cooled, are cooled down by transferring heat to the surrounding structures for diffusion or thermal radiation. This phenomenon is equivalent to a convective heat transfer with a fluid upon a suitable definition of an equivalent heat transfer coefficient h_{eq}. In this case, if $B_i < 0.1$, the classical lumped capacitance method can be applied. In order to define the equivalent heat transfer coefficient, the system is initially supposed to be simplified with a 0D approximation, therefore the resulting energy balance is:

$$\rho c \frac{\partial T}{\partial t} V = -h_{eq} \cdot A \cdot (T - T_0) \tag{4.1}$$

where T_0 is the temperature of the surrounding structures, assumed constant, V the volume, A the external surface, while ρ and c can be considered the density and specific heat capacity respectively averaged on the volume (indeed, a TFW panel is composed of two materials in the models developed, W and SS). In order for the model to be as general as possible, T_0 can be treated as the temperature of an equivalent coolant, therefore referred to as T_{water} as for NHF and EHF panels. The above equation has the following analytical solution:

$$T(t) = T_{water} + (T_{in} - T_{water}) \cdot e^{-t/\tau} \tag{4.2}$$

with T_{in} being the initial temperature, and $\tau = \frac{\rho c V}{h_{eq} A}$. At this point, this analytical solution can be compared to data from more accurate simulations as shown in figure 4.1.

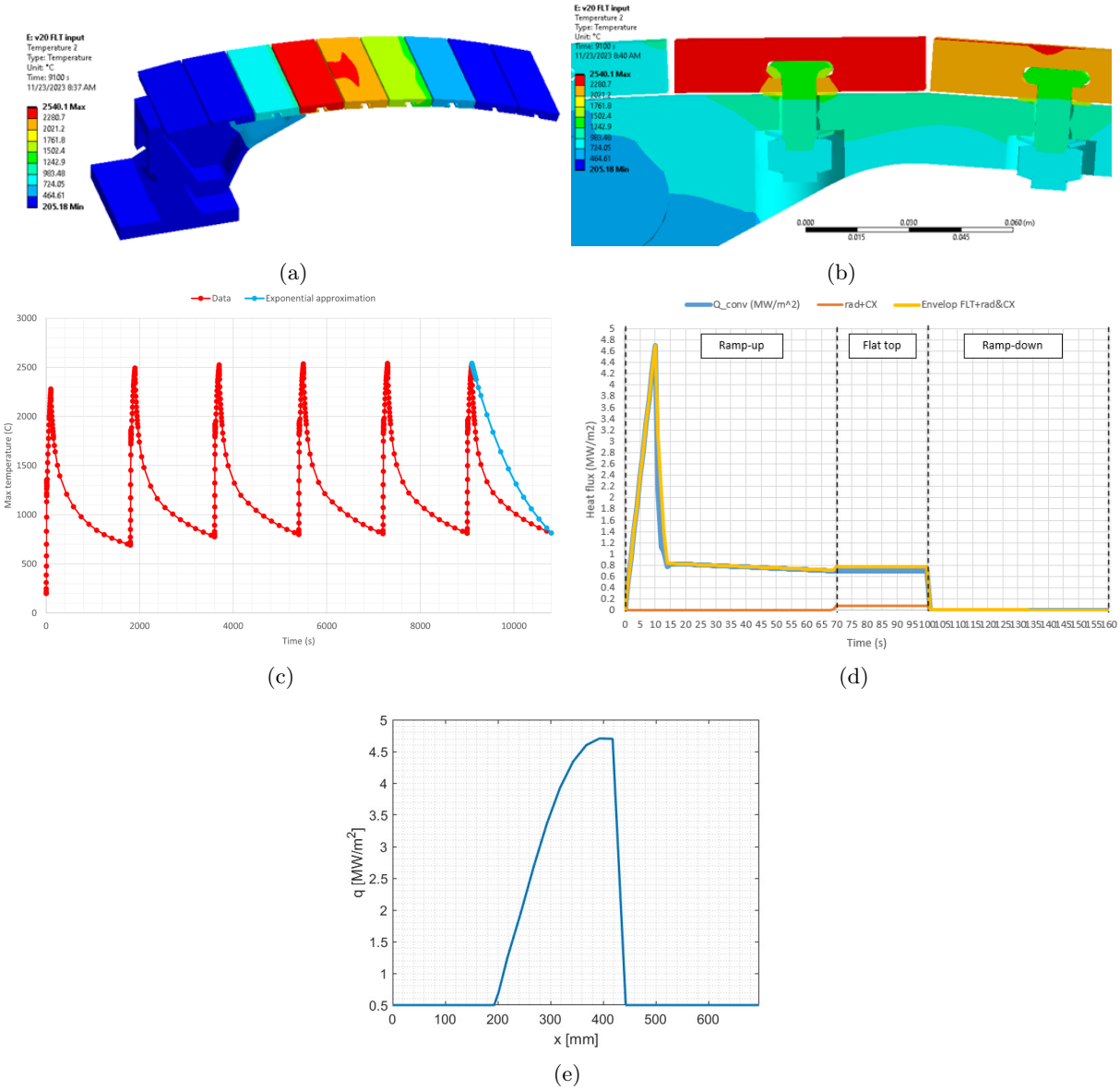

Figure 4.1: 3D time-dependent simulation of a TFW panel's finger with a periodical heat load in Ansys. In particular: temperature distribution at the end of the 6th cycle (a); detail of the temperature distribution of W tile and a bolt at the end of the 6th cycle (b); trend of the maximum temperature in the finger compared to the exponential approximation (c); periodical heat load employed (Q_{conv} in the figure); (e) heat load space distribution. Courtesy of ITER Blanket Section [Deliege, 2024].

The simulation reported in the above picture is a time-dependent 3D simulation in Ansys for the purpose of TFW panel's finger design. The input heat load is applied periodically for 6 cycles every 1800 s for a total of 100 s, corresponding to the duration of a plasma pulse. This heat load is artificial and it is used for design purposes, thus it does not represent typical heat flux profiles during a single plasma pulse. However, similarly to realistic heat flux profiles, this heat load is periodic in time, coherently with the fact that ITER operation will be pulsed. Indeed, because of inertial cooling, a discharge phase is necessary so that panels can cool down for some time through diffusion and radiation heat transfer before initiating a new plasma pulse. That being said, the exponential approximation is compared to the time evolution of the maximum temperature during the discharge phase of the 6th cycle, knowing the initial and the final temperature of the discharge phase. In this way, the only unknown value in equation 4.2 is τ, allowing to then evaluate $h_{eq} = \frac{\rho c V}{\tau A}$. Finally, the Biot number results in $B_i = \frac{h_{eq} * L}{k} \simeq 0.06 < 0.1$, therefore the initial assumption of using a 0D model is verified. As can be observed in the picture, the 0D approximation does not accurately describe the transient temperature variation in the discharge phase. This is quite reasonable as one of the key heat transfer phenomena involved, namely radiation heat transfer, should be described with a polynomial approximation rather than with an exponential. However, the 0D approximation allows to accurately describe the final temperature of each discharge phase, whose accuracy is essential as it constitutes the initial temperature of the following pulse. Moreover, the 0D approximation allows to define a h_{eq} (from this point forward referred to as simply h) similarly to NHF and EHF panel's models, thus increasing the flexibility of this model, which is one of the essential model requirements. Another limit of this approach is that the equivalent HTC calculated is defined in the case of high temperatures, therefore more precise estimations should take other types of heat loads into account. The h_{eq} has then to be considered a first-guess value suitable for representing panels' discharge phase in the case of high temperatures.

4.1.2 1D semi-infinite model

As mentioned in section 3.1.4, the 1D semi-infinite model is compared with the 1D simplified model in the domain depicted in figure 3.6. This comparison is useful to estimate a first-guess grid size in the x direction in order not to lose information about the thermal gradients in the material. In particular, as shown in figure 4.2, the analytical solution of 1D semi-infinite model, independent of the grid size, is compared with the numerical solution of the simplified 1D model solved with a FE scheme both in terms of accuracy and computational cost for different grid sizes. The final time of the simulation is set to be 1 s. The comparison is carried out by applying the same thermal flux in both models, namely $q_s = 4.7$ MW/m^2, which is a realistic value corresponding to the maximum heat load for EHF panels. Indeed, to get reliable results in terms of time scales involved, it is important to employ a realistic value of the thermal flux for the comparison as the magnitude of the heat flux influences the diffusion process, and in particular the higher the heat flux the sooner the temperature is undisturbed for a given distance from the surface.

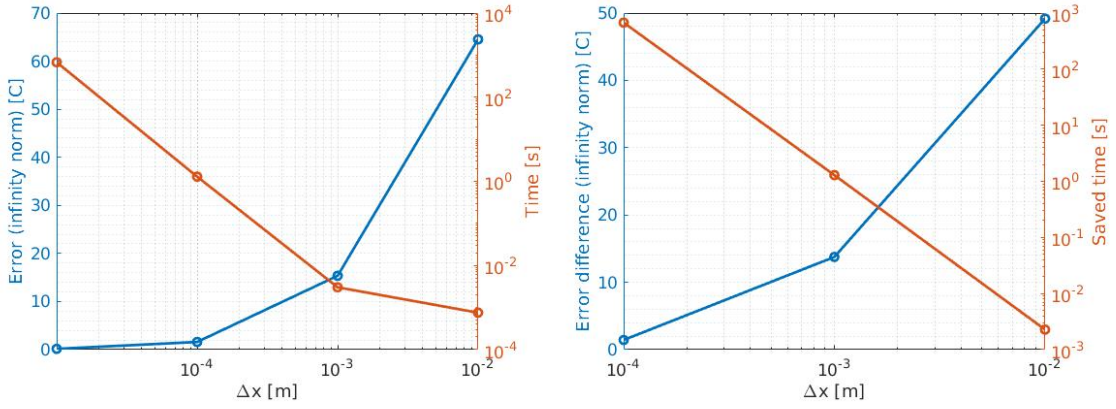

(a) (b)

Figure 4.2: Comparison between 1D semi-infinite model and 1D simplified model in absolute terms (a) and in marginal terms (b). In (a) the error is computed in infinity norm on the entire temperature profile for each grid size k, namely $err(k) = |\underline{T}(k) - \underline{T}_{an}|_\infty$, and evaluated at the final time step of the simulation. $\underline{T}_{an}$ is the temperature distribution computed through the analytical solution. On the right y-axis, the simulation of the elapsed time $time(k)$ of the 1D simplified model is shown. In (b) the error difference is defined as $e(k) = |err(k) - err(k-1)|$, and similarly the saved time $saved_{time} = |time(k) - time(k-1)|$, that is plotted on a logarithmic scale. In both figures, the x-axis is logarithmic.

As shown in the picture, the difference between the models reasonably decreases for lower Δx, because the discretization error goes down, at the expense of the computational time. As shown in figure 4.2b, for $\Delta x = 1e-4$ m there is the highest saved time with a very low discretization error of around 2 °C. If this grid size is used for the computational grid of EHF panels, the resulting number of nodes is $N_x = 108$. As NHF and TFW panels' thickness is higher, this would result in a bigger number of nodes. However, for the sake of keeping models as general as possible, it is desirable to have the same number of nodes in the x direction for each model regardless of FWP type. Therefore, in the case of NHF and TFW panels, it is chosen $\Delta x \simeq 3e-4$ m so that the number of nodes is $Nx = 108$ as well. Obviously, in this way, the discretization error committed is higher, specifically around 10 $°C$ (figure 4.2a), which is still deemed to be acceptable. Therefore, $N_x = 108$ is deemed to be a reasonable grid resolution to accurately get temperature variations in the few first millimeters of FWPs. Another conclusion that is possible to draw from picture 4.2 is that the 1D numerical model discretized with a FE scheme is quite computationally heavy. For instance, in the case of $\Delta x = 1e-4$ m, the simulation takes around 1.2 s (as shown in figure 4.3, this value is obtained by computing the statistical distribution of computational times in ITER computing cluster). This value is too high for the RT implementation (indeed, it is above the final time of the simulation) and this is due to the stability limit required for the FE scheme, which is clearly quite stringent. Therefore, in order to achieve lower computational times, from this point forward it has been preferred to choose BE discretization schemes, which do not have the limitation of the stability condition.

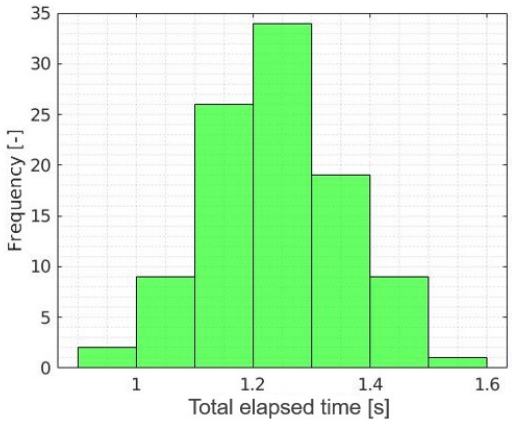

Figure 4.3: Statistical distribution of computational time obtained by performing 100 simulations in ITER computing cluster.

As discussed in section 3.1.4, the length of the slab is set to be high enough for the temperature profile far from the surface to be undisturbed as much as possible, thus respecting the underlying hypothesis of the 1D semi-infinite model of rapid thermal fluxes. In order to verify the choice of the slab length, the comparison between 1D semi-infinite model and 1D simplified model is carried out for increasing lengths, but with the fixed value of $\Delta x = 1e-4$ m. That being the case, the discretization error is fixed, so the only difference in the models is associated to the length employed. In this case, the simulation time is not 1 s, but instead, the simulation is stopped when the error (still in infinity norm) between the models is set to reach 100 °C, which is deemed to be a non-acceptable difference. Figure 4.4 shows the result of this comparison. As expected, the longer the slab is the higher is the time needed for the 1D semi-infinite model to be inaccurate. Indeed, for higher slab lengths, the heat takes more time to diffuse, therefore it is more likely that the temperature far from the surface is undisturbed. It turns out that, in the case of $L = 100$ mm, the 1D semi-infinite model becomes unacceptably inaccurate after about 55 s, far more than the simulation time of before (1 s). Therefore, this justifies the choice of the slab length in the previous simulation. Nevertheless, for a slab length of around 10 mm, which is the typical order of magnitude of fingers' thickness in the models developed, the 1D semi-infinite model is inaccurate after already 1.5 s. On top of that, ramp-up and ramp-down phases at ITER last tens of seconds, so the heat has more time to diffuse making it is even less likely for the temperature profile to be undisturbed. In other words, for longer simulations of tens of seconds, errors would be even higher, namely the 1D semi-infinite model would be less accurate, i.e., the underlying hypothesis of rapid thermal fluxes would not be valid anymore. For this reason, the 1D semi-infinite model is deemed useful exclusively to get a first-guess reasonable value of N_x, but more accurate models are needed to accurately describe heat transfer processes. Furthermore, as written at the beginning of this section, being the 1D semi-infinite model not a valid approximation, the 0D model is not valid as well.

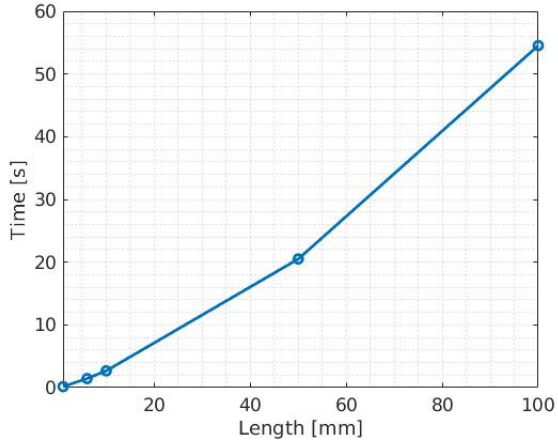

Figure 4.4: Time at which the maximum temperature difference between the 1D semi-infinite model and 1D simplified model reaches the threshold of 100 °C as a function of the slab length. Calculations done assuming $q_s = 4.7$ MW/m^2.

4.1.3 EHF panels

In this section, the results for EHF panel's fingers, depicted in figure 4.5, are presented and discussed. For the sake of conciseness, only the results of the 1D model with constant properties and the 2D model with constant properties are presented, leaving the results of the variable properties aside. Subsequently, a comparative assessment is carried out. In particular, first, the 2D model is validated against a more accurate simulation in order to demonstrate the validity of the 2D assumption with a rectangular grid for a finger. Afterwards, a comparison between 1D versus 2D models in order to assess the validity of the 1D assumption is performed. The following comparison is between the 1D model with constant properties with the 1D model with variable properties (solved with both Newton's method and FC method) in order to assess the validity of using constant properties. The comparative assessment allows to find the most representative model for modelling heat transfer phenomena in EHF panels, namely a model capable of computing the thermal response of FWPs with sufficient accuracy while being as simple as possible at the same time. A convergence analysis on this model is then carried out in order to find a reasonable time step for the time simulation for RT application. At this point, a suitable model in terms of a trade-off between accuracy and computational cost is identified for EHF panels. Having made a decision on the final model to employ, a sensitivity analysis on the heat transfer coefficient is finally carried out.

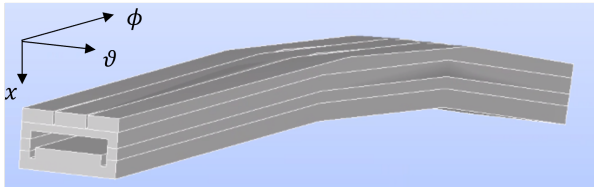

Figure 4.5: CAD file of EHF panel's fingers. Courtesy of ITER Blanket Section.

1D model with constant properties

In the case of a 1D model of a finger along the x direction, the domain of interest is the one depicted in figure 3.7. With the hypothesis of constant properties, the discretization of the energy balance equation is equation 3.7, in which the Δx employed is the one discussed in section 4.1.2. The geometric values in figure 3.7 are taken as shown in figure 3.4. It is assumed the finger to be in thermal equilibrium with the cooling water at the beginning of the simulation. Subsequently, a constant heat flux of $q_s = 4.7$ MW/m^2, equal to the maximum design value for EHF panels, is applied. The final time of the simulation is 30 s, corresponding to a steady-state temperature distribution. Results are shown in figure 4.6.

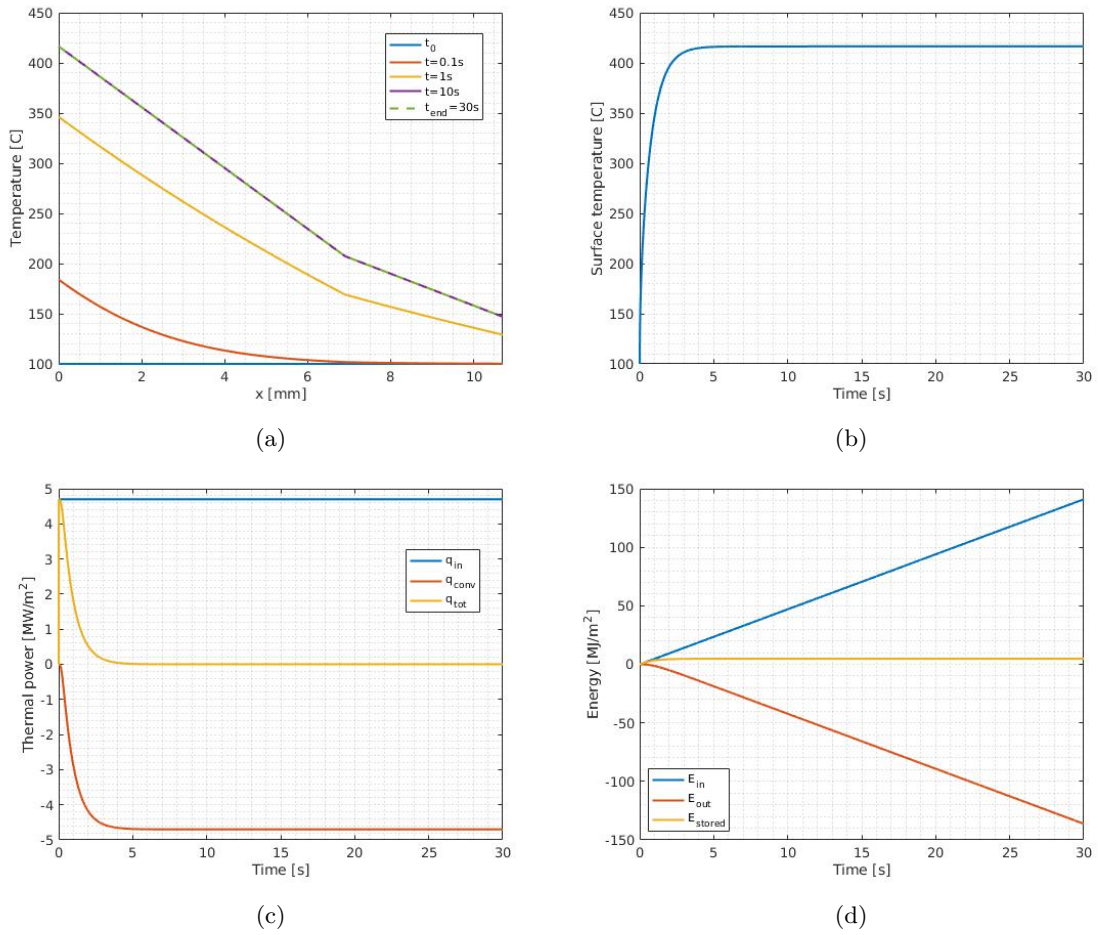

Figure 4.6: Results of 1D model for EHF panel's fingers: (a) temperature distribution; (b) surface temperature time evolution; (c) power flow; (d) energy conservation.

As depicted in figure 4.6a, there is a transient phase in the temperature distribution of the domain, after which a steady-state condition is reached because the incident heat flux q_s is balanced by the heat transferred to the cooling water (indeed, as shown in figure 4.6c, the net power eventually becomes zero). The steady-state temperature distribution is reasonably linear and is characterized by slope change at the interface between the materials due to their different thermal conductivity, coherently with the condition of heat flux continuity. As far as the surface temperature time evolution is concerned, it goes from an initial value corresponding to the cooling water temperature to a plateau in steady-state conditions. The energy conservation is respected (indeed E_{in} in figure 4.6d is linear coherently with q_s being constant, and the time derivative of the energy stored in the domain eventually approaches a zero value coherently with the temperature distribution being constant).

2D model with constant properties

In the case of a 2D model of a finger along x and toroidal directions, the domain of interest is the one depicted in figure 3.8. With the hypothesis of constant properties, the discretization of the energy balance equation is equation 3.9. The thermal response of an EHF panel's finger is investigated by applying the incident constant heat flux q_s profile depicted in figure 4.7c. Results are reported in figures 4.7a and 4.7b. As it is possible to observe from the figure, isothermal lines are approximately horizontal, meaning that heat diffusion takes place predominantly in the x direction. This is due to the presence of the coolant. The energy conservation demonstrates the physical consistency of the model, as E_{in} linearly increases (coherently with the incident heat flux being constant) and E_{stored} is constant in steady-state conditions.

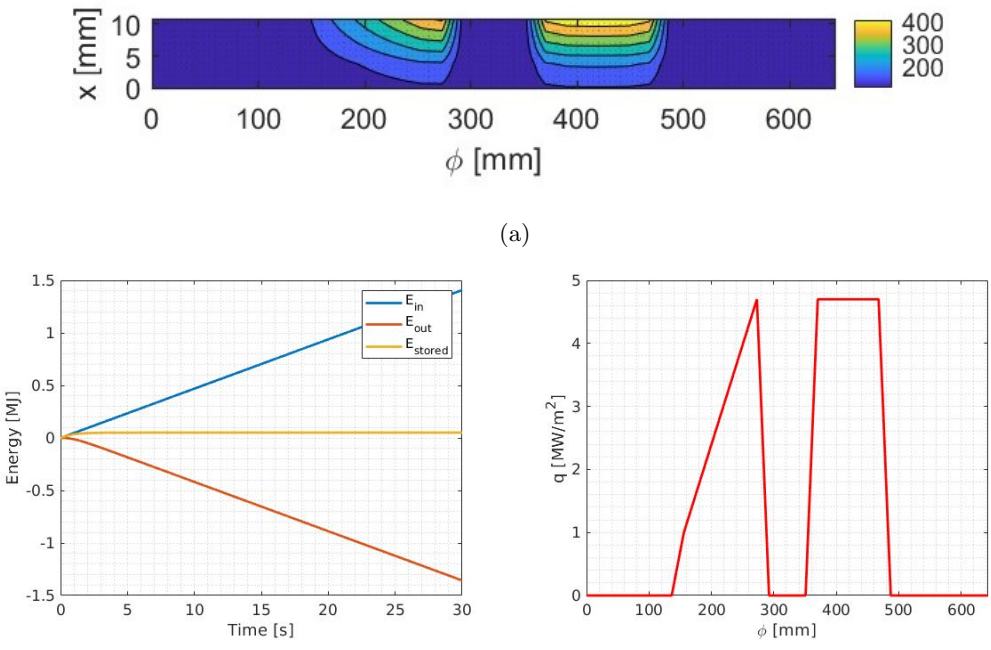

(a)

(b)

(c)

Figure 4.7: EHF panel's finger 2D model: (a) steady state temperature distribution; (b) energy conservation; (c) incident heat flux q_s toroidal profile applied to the domain depicted in figure 3.8.

Comparative assessment

In order to find the most representative model for heat transfer phenomena occurring in EHF panel's fingers, a comparative assessment is carried out. Firstly, with the goal of assessing the validity of the 2D model with a rectangular grid, the 2D model is validated against a more accurate simulation available, namely a 2D simulation solved with finite volumes (FV) taking into account fingers' toroidal shaping and developed in Python [Brank, 2024]. This simulation employs the constant incident thermal flux profile q_s shown in figure 4.8a. The steady-state temperature map is shown in figure 4.8b.

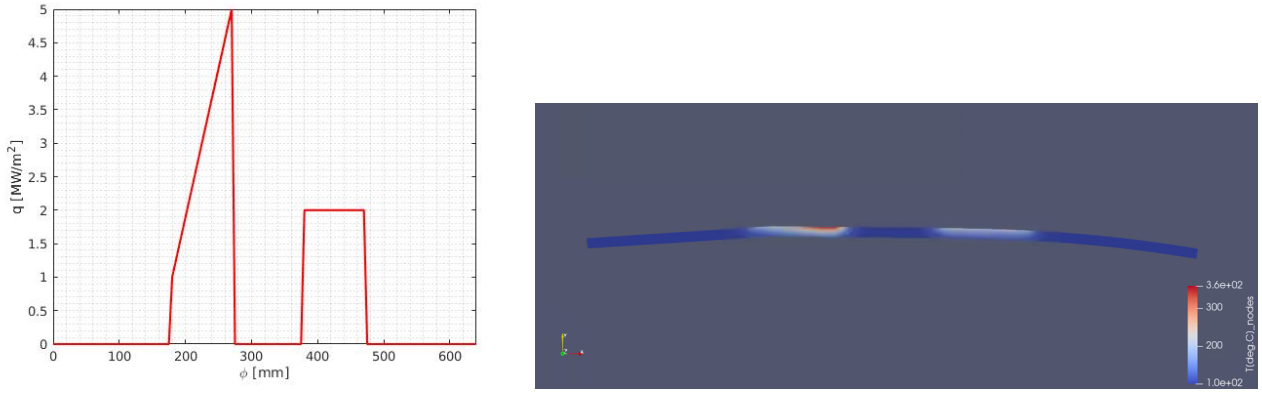

(a)

(b)

Figure 4.8: 2D simulation with toroidal shaping solved with FV method. (a) Incident heat flux profile. (b) Steady-state temperature distribution.

The benchmark of the 2D model with a rectangular grid developed in MATLAB with the more accurate 2D simulation with toroidal shaping is performed by comparing their surface temperature distribution in steady-state conditions and by employing the same constant incident heat flux profile and the same heat transfer coefficient with a coolant at the same temperature. The result of the validation is presented in figure 4.9. As shown in the figure, there is only a slight

difference between the profiles, probably due to the toroidal shaping. Therefore this comparison validates the 2D model with a rectangular grid thus justifying one of its underlying assumptions, namely that fingers' toroidal shaping can be neglected. This model has the advantage of being more flexible than the FV model (indeed, for instance, in the latter the thermal flux is not designed to be updated in time).

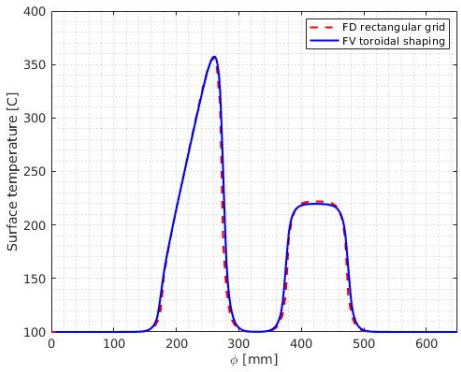

Figure 4.9: Results of the validation for EHF panels: surface temperature distribution in steady-state conditions.

The following comparison is between the 1D model with constant properties with the 2D model with constant properties with the goal of verifying the 1D approximation. As shown in figure 4.10, the comparison is performed in steady-state conditions in different sections of the domain, a section characterized by a high toroidal thermal gradient of the incident heat flux, and a section in which the incident heat flux is toroidally uniform. Along the first section, the 1D model slightly overestimates the surface temperature of approximately 30 °C, as it does not take the toroidal diffusion into account. Along the second section, instead, the temperature profiles are basically overlapping.

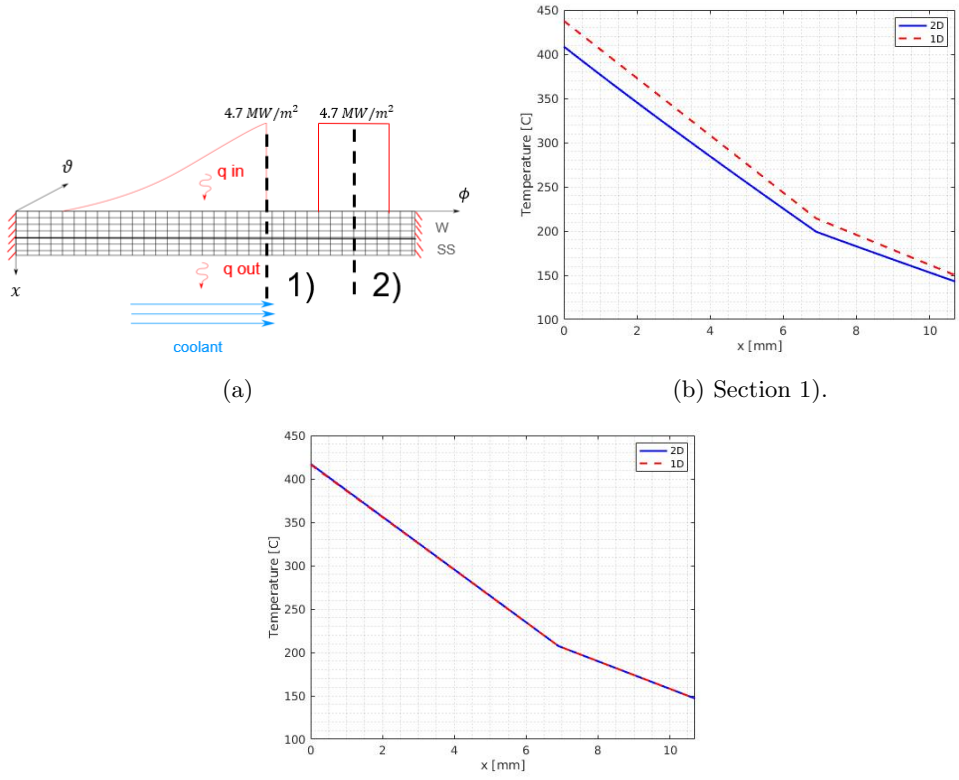

(a)

(b) Section 1).

(c) Section 2).

Figure 4.10: Comparison between 1D and 2D models in terms of accuracy in two different sections in steady-state conditions: (a) sections of interest; (b) temperature distribution along section 1; (c) temperature distribution along section 2.

By looking at figure 4.11, reporting the statistical distribution of computational times in ITER computing cluster, it is evident that the computational cost of the 2D model is much higher than that of the 1D model. Given its relatively small difference with the 2D model (also on the conservative side) and its benefit in terms of computational cost, the 1D model approximation is deemed to be acceptable. The validity of the 1D approximation consequently justifies the assumption of neglecting the castellations, whose presence could have been, in principle, relevant because of the interruption of heat diffusion in the toroidal direction.

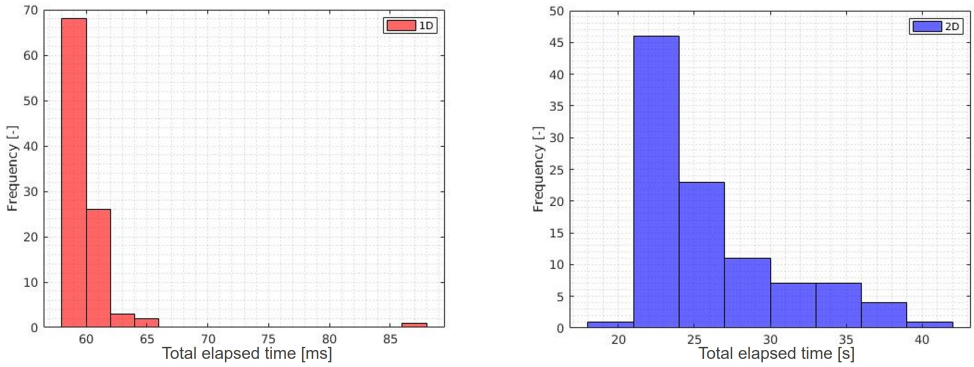

(a) (b)

Figure 4.11: Comparison between 1D and 2D models in terms of computational cost, measured as simulations' elapsed time: (a) computational time distribution for the 1D model; (b) computational time distribution for the 2D model. Note the different time scales, ms for the 1D model and s for the 2D model. The statistical distribution is obtained by performing 100 simulations in ITER computing cluster.

Once established the validity of the 1D approximation, the influence of variable properties is investigated. When doing a comparison between a model with constant properties and a model with variable properties, the immediate question is at what temperature to evaluate the properties of the model with constant properties. As a first guess, the criterion is evaluating W properties at the average temperature between the surface and the interface in steady-state conditions, and CuCrZr properties at the average temperature between the interface and the cooling water in steady-state conditions. These temperatures can be easily evaluated in steady-state conditions because an analytical solution can be found through the electric analogy. Indeed, with reference to the domain in figure 3.7, the electric analogy yields:

$$q_s = \frac{\Delta T}{R_{tot}} = \frac{T(x=0) - T(x=L_{tot})}{R_W + R_{CuCrZr}} = \frac{T(x=0) - T(x=L_{tot})}{\frac{L_W}{k_W} + \frac{L_{tot}-L_W}{k_{CuCrZr}}} \tag{4.3}$$

where R_W and R_{CuCrZr} are the thermal resistances of W and CuCrZr and R_{tot} the total one. Given that $q_s = h \cdot (T(x = L_{tot}) - T_{water})$ in steady-state, the temperature of the surface exposed to the plasma can be found by substituting this expression in the previous one:

$$T_{surf} = \frac{q_s}{h} + T_{water} + q_s \cdot \left(\frac{L_W}{k_W} + \frac{L_{tot} - L_W}{k_{CuCrZr}} \right) \tag{4.4}$$

from which the temperature at the interface can be found as:

$$T_{int} = T_{surf} - q_s \cdot R_W \tag{4.5}$$

At this point, the 1D model with constant properties can be compared with the 1D model with variable properties solved with Newton's method and FC method. The results of the comparison are shown in figure 4.12.

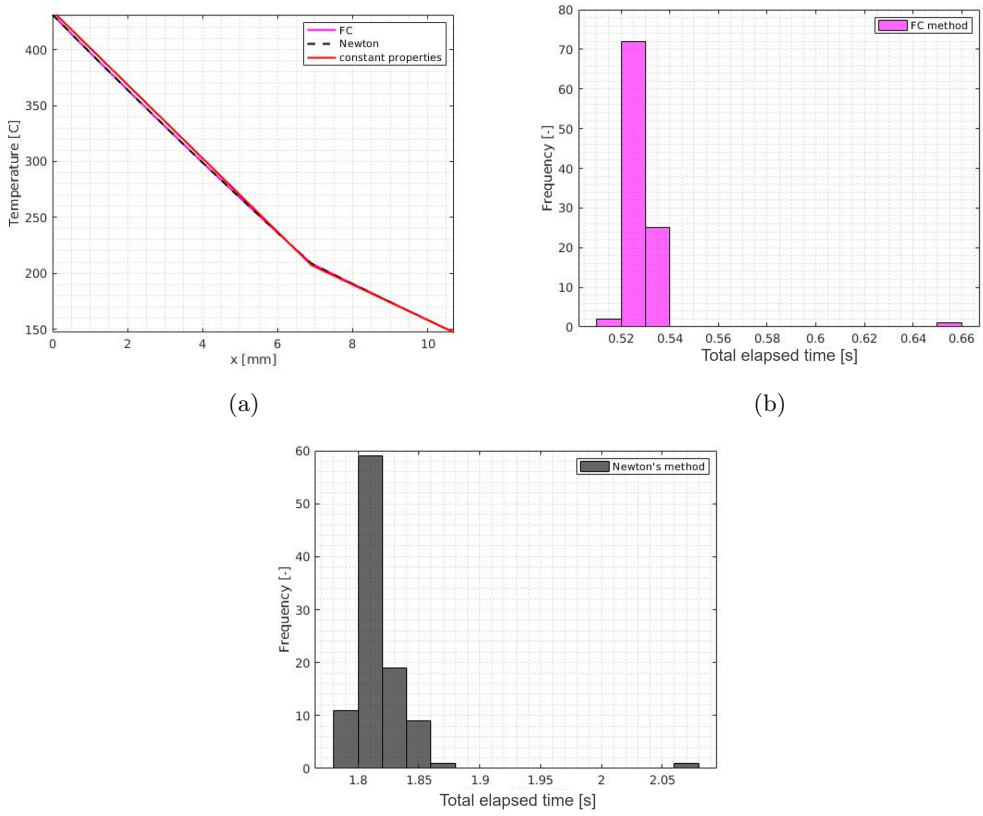

(a) (b)

(c)

Figure 4.12: Comparison between the 1D model with constant properties with the 1D model with variable properties: (a) temperature distribution in steady-state conditions; (b) simulation elapsed time in case of FC method (statistical distribution); (c) simulation elapsed time in case of Newton's method (statistical distribution).

As depicted in the figure, the influence of variable properties on the solution is negligible for the steady-state distribution, while the computational cost of implementing either the FC method or Newton's method is obviously higher than that of having constant properties depicted in figure 4.11a. This is due to the fact that, for the FC method, it is necessary to update the coefficients of the matrix at each time step, therefore a matrix inversion must be performed at each time step while, in the case of constant properties, the matrix can be inverted only once before the time loop. For Newton's method, the higher computational cost is linked to solving a system of non-linear equations at each time step. Additionally, by comparing Newton's method with the FC method, even if the FC method is a simplified approach to solving non-linear problems, it is evident that Newton's method does not have any benefit in terms of accuracy, while its computational cost is higher. Therefore, if one wants to consider variable thermal properties, Newton's method is not recommended.

In order to prove that evaluating the thermal properties using the average temperature in the materials is a reasonable approximation when comparing a 1D model with constant properties with a 1D model with variable properties, the former model is compared with the latter in terms of absolute difference in the computed surface temperature for different magnitudes of incident thermal fluxes. The comparison, reported in figure 4.13, shows that the difference between the models increases for higher heat fluxes, but is quite low in all the cases with a maximum error of 12 °C for $q = 5$ MW/m^2. It is meaningless to investigate the effect of higher heat fluxes, which occur in the case of accidental events, as this work has the objective of FW protection, thus actuators should intervene before reaching these higher heat fluxes. Therefore, this justifies the choice of the temperature at which thermal properties are evaluated in the case of constant properties. The result of these analyses confirms the validity of the constant properties assumption.

As a consequence of the comparative assessment, the 1D model with constant properties is deemed to be the most representative model for modelling heat transfer phenomena in EHF panels' fingers.

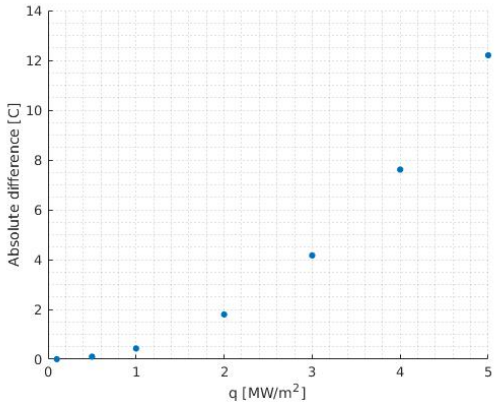

Figure 4.13: Difference in terms of surface temperature between 1D model with constant properties and 1D model with variable properties (solved with FC method) for different incident heat fluxes.

Convergence analysis

The following step towards the definition of a suitable thermal model for EHF panel's fingers in terms of a trade-off between accuracy and computational cost is a convergence analysis. As the grid size in the x direction is already fixed from the analysis on the 1D semi-infinite model, as discussed in section 4.1.2, the convergence analysis is focused on the choice of the time step of the simulation Δt, which is a free parameter.

The convergence analysis on Δt is carried out starting from analyzing two different types of incident heat flux. As discussed in section 2.19, the incident heat flux is distributed on a given FWP and, when the plasma changes its position (such as during ramp-up and ramp-down phases) the heat flux shifts in time because the wetted area shifts accordingly to plasma movements. On top of that, the FWP of interest receives the thermal flux crossing the separatrix P_{SOL}, which increases during the ramp-up phase and remains constant during the flat-top phase. Therefore, a given point on a FWP can be interested by two types of heat fluxes. The first type, linked to plasma movements, causes the point of interest, in the first place not belonging to the wetted area, to be suddenly exposed to a heat flux. This is modelled as a step response $q_s(t) = 4.7$ MW/m^2. The second type, linked to P_{SOL}, causes the point of interest, continuously belonging to the wetted area, to be exposed to an increasing heat flux in the ramp-up phase. This is modelled through an exponential starting from zero and eventually reaching a constant value, namely $q_s(t) = 4.7 \cdot (1 - e^{-t/\tau})$ MW/m^2. This exponential is assumed to have a time constant corresponding to the confinement time in ITER, namely $\tau = 3.7$ s [Shimada et al., 2007]. Indeed, when the auxiliary power is turned on, P_{SOL} follows the ramp-up auxiliary power with a characteristic time of τ.

As the thermal model is discretized in time, there can be some discretization errors due to the finite Δt employed. Specifically, as far as the step response is concerned, there can be a delay between the effective signal and its computation. In the worst-case scenario, the delay is $\Delta t/2$. As far as the exponential heat flux is concerned, a finite Δt causes the input energy in the domain to be lower than in the case of a continuous input signal, thus leading to inaccuracies in the temperature distribution. That being the case, the convergence analysis is carried out by investigating the impact of different time steps on the solution with the two types of heat flux signals described above. Results are shown in figure 4.14, showing the discretization error and the number of computations for different time steps and for the two types of heat flux signals. In the case of a step input signal, the error for each Δt is calculated by comparing the solution obtained with an input delayed by $\Delta t/2$ with the solution without input delay. The error is defined as the maximum difference (in absolute terms) between the two solutions during the whole transient. In the case of exponential signal, the error for each Δt is evaluated by comparing the computed surface temperature with the solution obtained with the smallest Δt employed, which is taken as a reference. Additionally, for each Δt, the number of computations approximated as $n_c = \frac{elapsed\ time}{\Delta t}$ is computed. As shown in the figure, while the number of computations for the two types of heat fluxes is of the same order of magnitude, the error committed in the case of a delay of the step response signal is higher than that of the exponential signal for the same Δt. This is probably due to the fact that, for an exponential signal, the slab receives some heat flux at least, even though less than it would receive in the case of a continuous signal, while for a step input the slab does not receive any heat at all for $\Delta t/2$, determining a higher temperature difference between the two cases. The Δt chosen as a result of a compromise be-

tween accuracy and computational cost is $\Delta t = 1e-2$ s, which determines an error of approximately 25 °C in the case of a step response signal (in absolute terms). It is important to underline that the convergence analysis itself should be replicated several times as the number of computations in the ITER cluster is not deterministic. This is left for further studies, therefore the number of computations in the figure is to be considered indicative of the computational cost.

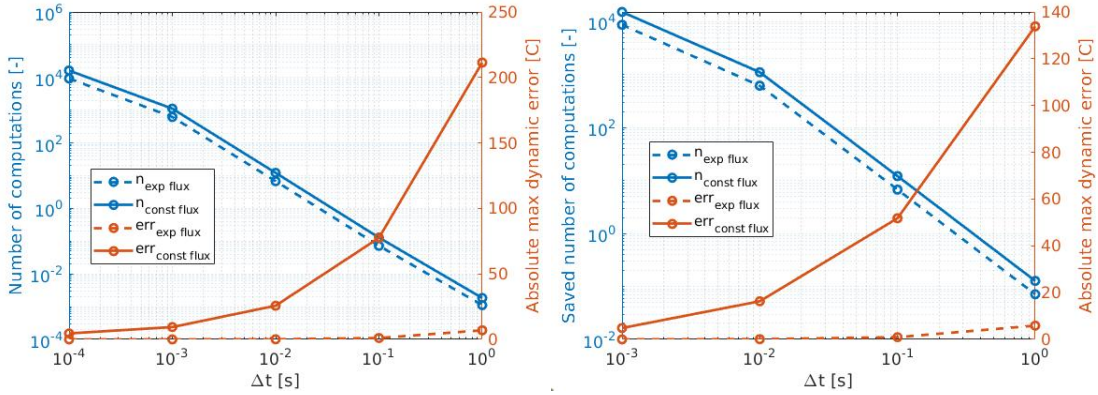

(a) (b)

Figure 4.14: Results of time convergence analysis for a step input heat flux and an exponential heat flux: error and number of computations in absolute terms (a), and in marginal terms (b).

At this point, having carried out a comparative assessment and a convergence analysis, it is possible to conclude that the 1D thermal model with constant properties with $N_x = 108$ nodes in the x direction and with a $\Delta t = 1e-2$ s represents the most suitable control-oriented model in terms of a trade-off between accuracy and computational cost for modelling heat transfer phenomena occurring in EHF panel's fingers. Once this is established, a further analysis of the HTC is hereafter presented.

Sensitivity analysis on the heat transfer coefficient

As already mentioned in 3.1.5, the HTC employed is assumed to be constant without employing any correlation. In order to investigate the validity of this assumption, a sensitivity analysis of the HTC is carried out. Specifically, for a given perturbation of δh the corresponding perturbation of the surface temperature in steady-state conditions δT_s is evaluated. The result is shown in figure 4.15.

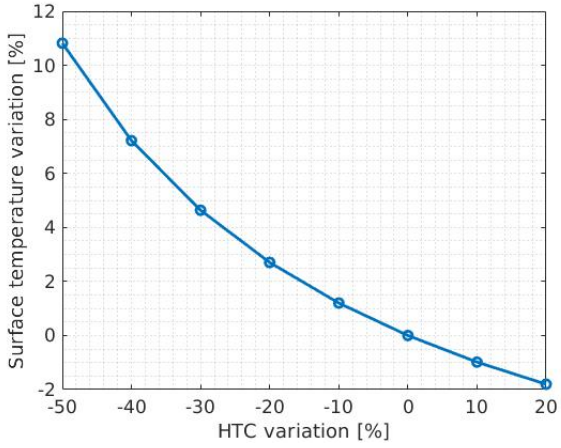

Figure 4.15: Sensitivity analysis on the HTC, showing the impact of its variation on the variation of the surface temperature in steady-state conditions.

Obviously, the worst case is an underestimation of the HTC, as it leads to a higher surface temperature. However, the surface temperature is not severely affected by HTC variation, as for an underestimation of the HTC of 50 % the

corresponding increase in the surface temperature is 11 %. However, it can be shown that for higher thermal fluxes the surface temperature becomes more sensible as the HTC varies. Indeed, in steady-state conditions by applying the electric analogy:

$$q_s = \frac{T_s - T_0}{R_T} = h \cdot (T_0 - T_{water}) \tag{4.6}$$

where T_0 is the temperature of the surface in contact with the coolant and R_T is the total thermal resistance. The above expression can be written as:

$$T_s = q_s \cdot R_T + \frac{q_s}{h} + T_{water} \tag{4.7}$$

If this expression is then perturbed, it turns out that:

$$\delta T_s(\delta h) = -q \cdot \frac{\delta h}{h + \delta h} \tag{4.8}$$

which proves that the surface temperature's sensitivity with HTC depends linearly on the incident heat flux. Therefore, the conclusion is that for EHF panel's fingers, even in the case of a design-limit heat flux of 4.7 $\mathrm{MW/m^2}$, the assumption of considering a constant heat transfer coefficient without employing a correlation is reasonable. Nevertheless, if one wants to have higher model precision or in the case of higher thermal fluxes such as in accidental cases, it is recommended to evaluate the HTC in a more accurate way by using suitable correlations, taking into account also the evolving conditions of the coolant.

4.1.4 NHF panels

In this section, the results for NHF panels, depicted in figure 4.16, are presented and discussed. For the sake of conciseness, only the results of the 1D model with constant properties and the 2D model with constant properties are presented, leaving the results of the variable properties aside. Subsequently, a comparative assessment is carried out. In particular, first, a comparison between 1D versus 2D models in order to assess the validity of the 1D assumption is performed. The following comparison is between the 1D model with constant properties with the 1D model with variable properties (solved with both Newton's method and FC method) in order to assess the validity of using constant properties. The comparative assessment allows to find the most representative model for modelling heat transfer phenomena in NHF panels, namely a model capable of computing the thermal response of FWPs with sufficient accuracy while being as simple as possible at the same time. A convergence analysis on this model is then carried out in order to find a reasonable time step for the time simulation for RT application. At this point, a suitable model in terms of a trade-off between accuracy and computational cost is identified for NHF panels. Having made a decision on the final model to employ, a sensibility analysis on the heat transfer coefficient is finally carried out.

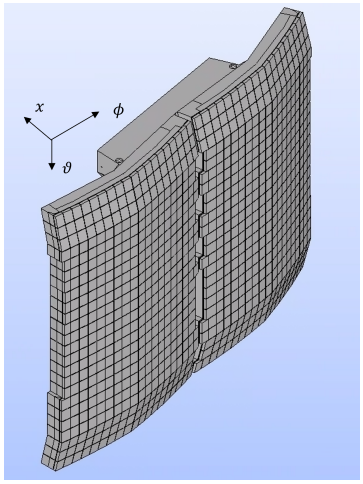

Figure 4.16: CAD file of NHF panels. Courtesy of ITER Blanket Section.

1D model with constant properties

In the case of a 1D model of a finger along the x direction, the domain of interest is the one depicted in figure 3.7. With the hypothesis of constant properties, the discretization of the energy balance equation is equation 3.7, in which the Δx employed is the one discussed in section 4.1.2. The geometric values in figure 3.7 are taken as shown in figure 3.4. It is assumed the finger to be in thermal equilibrium with the cooling water at the beginning of the simulation. Subsequently, a constant heat flux of $q_s = 2$ MW/m^2, equal to the maximum design value for NHF panels, is applied. The final time of the simulation is 30 s, corresponding to a steady-state temperature distribution. Contrarily to EHF panels in which cooling channels have a rectangular shape thus making the thermal gradient predominantly 1D towards the coolant, NHF panels are characterized by circular pipes, introducing 2D effects as a consequence. In order to take these 2D effects into account, the HTC is divided by a factor f_{2D} retrieved from the RACLETTE code [Raffray and Federici, 1997]. The f_{2D} factor employed in the RACLETTE code is defined for a similar geometry of PFCs as NHF panels, but it is defined for specific geometric quantities, which are different from the ones involved in this work. Therefore, the f_{2D} factor employed is considered to be suitable for a first guess, but further studies are necessary to assess a more accurate f_{2D} factor for the specific geometry of NHF panels. Results are shown in figure 4.17.

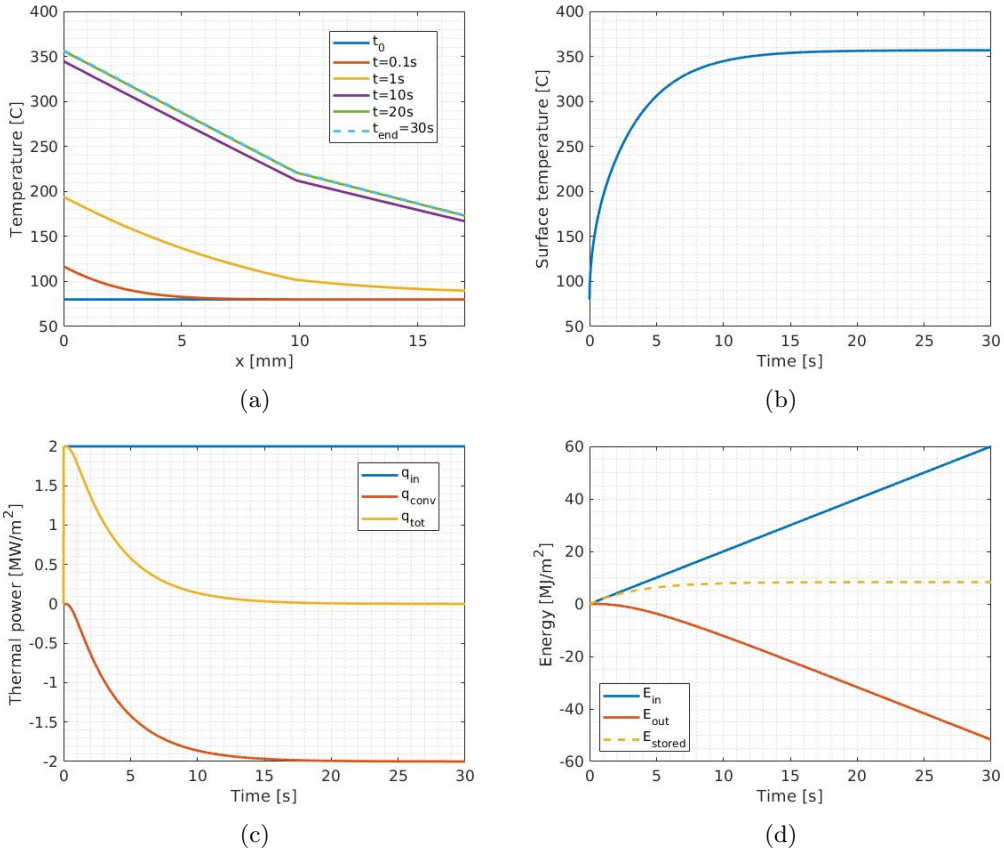

Figure 4.17: Results of 1D model for NHF panel's fingers: (a) temperature distribution; (b) surface temperature time evolution; (c) power flow; (d) energy conservation.

Heat transfer phenomena are qualitatively similar to EHF panel's fingers. Indeed, as depicted in figure 4.17a, there is a transient phase in the temperature distribution of the domain, after which a steady-state condition is reached because the incident heat flux q_s is balanced by the heat transferred to the cooling water (indeed, as shown in figure 4.17c, the net power eventually becomes zero). The steady-state temperature distribution is reasonably linear, and is characterized by a slope change at the interface between the materials due to their different thermal conductivity, coherently with the condition of heat flux continuity imposed. As far as the surface temperature time evolution is concerned, it goes from an initial value corresponding to the cooling water temperature to a plateau in steady-state conditions. The energy conservation is respected (indeed E_{in} in figure 4.17d is linear coherently with q_s being constant, and the time derivative of the energy stored in the domain eventually approaches a zero value coherently with the temperature distribution being constant).

2D model with constant properties

In the case of a 2D model of a finger along x and toroidal directions, the domain of interest is the one depicted in figure 3.8. With the hypothesis of constant properties, the discretization of the energy balance equation is equation 3.9. The thermal response of an NHF panel's finger is investigated by applying the incident constant heat flux q_s profile depicted in figure 4.18c. Results are reported in figures 4.18a and 4.18b.

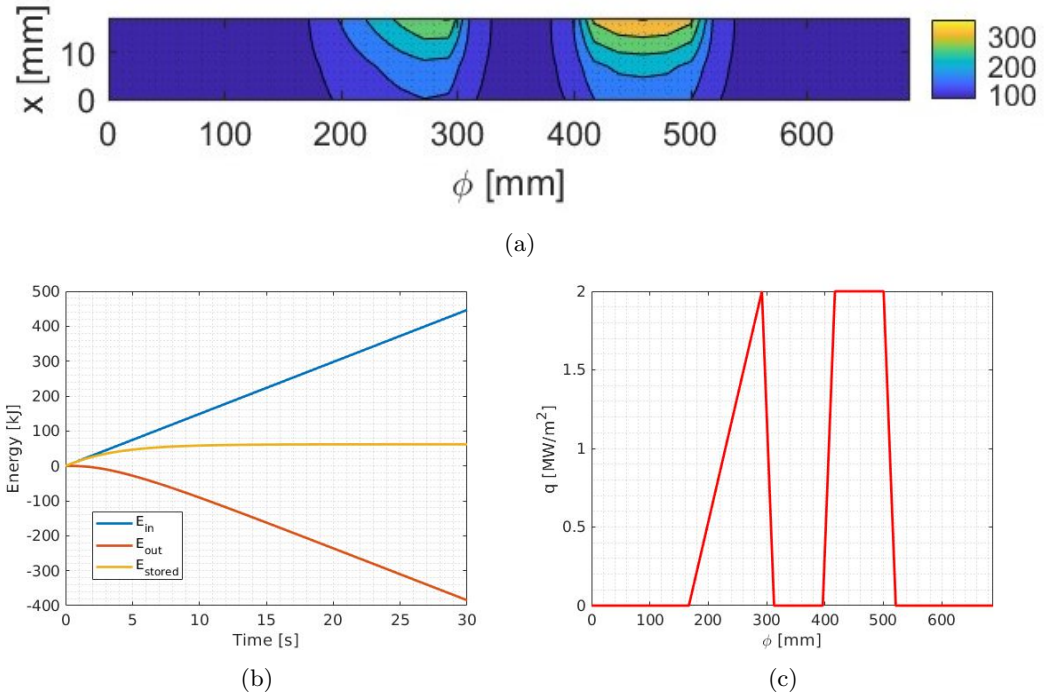

Figure 4.18: NHF panel's finger 2D model: (a) steady state temperature distribution; (b) energy conservation; (c) Incident heat flux q_s toroidal profile applied to the domain depicted in figure 3.8.

As it is possible to observe from the above figure, isothermal lines are approximately horizontal, meaning that the heat diffusion takes place predominantly in the x direction. This is due to the presence of the coolant. The energy conservation demonstrates the validity of the model, as E_{in} linearly increases (consistently with the incident heat flux being constant) and E_{stored} is constant in steady-state conditions.

Comparative assessment

In order to find the most representative model for heat transfer phenomena occurring in NHF panel's fingers, a comparative assessment is carried out. Contrarily to the case of EHF panel's fingers, for NHF ones the validation of the 2D model against a more accurate solution is not carried out, as more accurate simulations were not available. However, NHF panels are very similar to EHF ones both in terms of materials and heat transfer dynamic (indeed, both panels are actively cooled), therefore performing a model validation besides that of EHF panel's fingers is deemed to be not essential to assess the validity of the 2D assumption with rectangular grid for NHF panel's fingers. Nevertheless, a validation of the 1D model with a 2D simulation taking into account the presence of circular channels in order to estimate the f_{2D} in a more accurate way is deemed to be necessary and left for further studies. The first comparison is between the 1D model with constant properties and the 2D model with constant properties in order to assess the validity of the 1D simplification. As shown in figure 4.19, the comparison is performed in steady-state conditions in different sections of the domain, a section having a high toroidal thermal gradient in the incident heat flux, and a section in which the incident heat flux is toroidally uniform. Along the first section, the 1D model overestimates the surface temperature of approximately 45 °C, as it does not take the toroidal diffusion into account. Along the second section, instead, the temperature profiles are almost overlapping. Therefore, the 1D model is deemed to be sufficiently accurate, despite the slight overestimation with respect to the 2D model (which is also on the conservative side). By looking at figure 4.20, reporting the statistical distribution of computational times in ITER computing cluster, it is evident that the computational cost of the 2D model is much higher than that of the 1D model. Given its benefit in

terms of computational cost and its sufficient accuracy, the 1D model approximation is deemed to be acceptable. The validity of the 1D approximation consequently justifies the assumption of neglecting the castellations, whose presence could have been, in principle, relevant because of the interruption of heat diffusion in the toroidal direction.

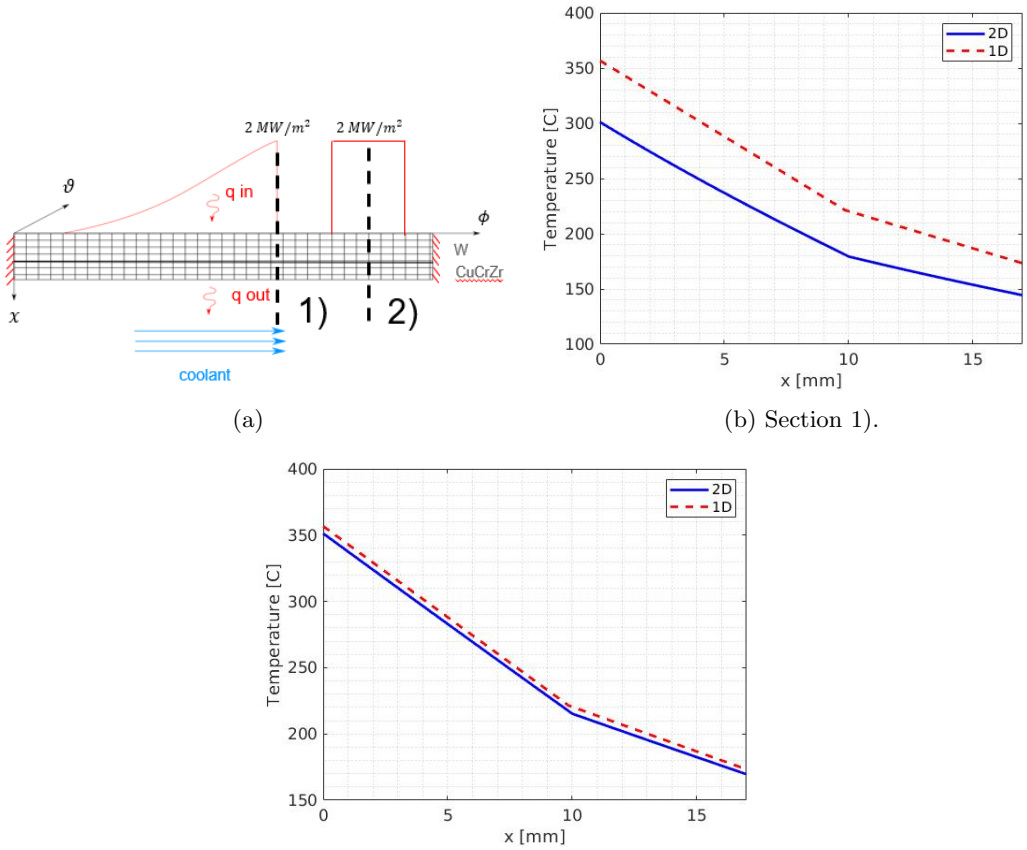

(a) (b) Section 1).

(c) Section 2).

Figure 4.19: Comparison between 1D and 2D models in terms of accuracy in two different sections in steady-state conditions: (a) sections of interest; (b) temperature distribution along section 1; (c) temperature distribution along section 2.

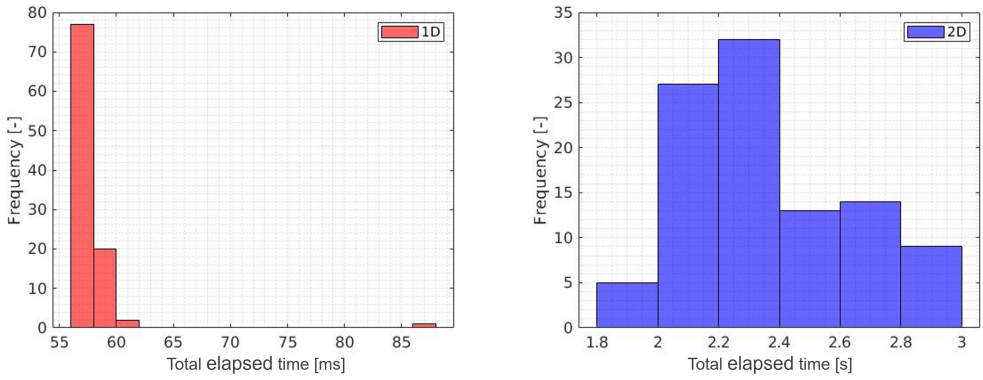

(a) (b)

Figure 4.20: Comparison between 1D and 2D models in terms of computational cost, measured as simulations' elapsed time: (a) computational time distribution for the 1D model; (b) computational time distribution for the 2D model. Note the different time scales, ms for the 1D model and s for the 2D model. The statistical distribution is obtained by performing 100 simulations in ITER computing cluster.

Once established the validity of the 1D approximation, the influence of variable properties is investigated. In the case of the constant properties model, properties are evaluated at the average temperature in the materials in steady-state conditions, similarly as for EHF panel's fingers. The 1D model with constant properties is compared with the 1D model with variable properties solved with Newton's method and FC method. The results of the comparison are shown in figure 4.21.

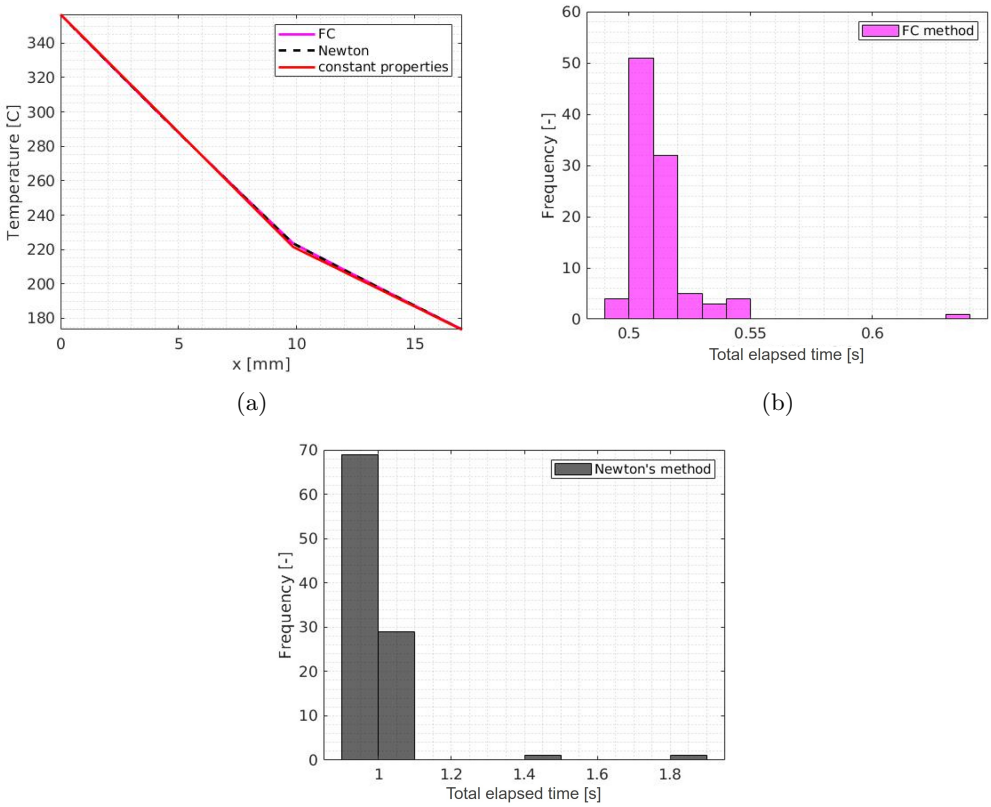

(a) (b)

(c)

Figure 4.21: Comparison between the 1D model with constant properties with the 1D model with variable properties. (a) temperature distribution in steady-state conditions; (b) simulation elapsed time in case of FC method (statistical distribution); (c) simulation elapsed time in case of Newton's method (statistical distribution).

As depicted in the figure, the influence of variable properties on the solution is negligible, while the computational cost of implementing either the FC method or Newton's method is obviously higher than that of having constant properties depicted in figure 4.20a. This is due to the fact that, for the FC method, it is necessary to update the coefficients of the matrix at each time step, therefore a matrix inversion must be performed at each time step while, in the case of constant properties, the matrix can be inverted only once before the time loop. For Newton's method, the higher computational cost is linked to solving a system of non-linear equations at each time step. Additionally, by comparing Newton's method with FC method, it is evident that the former does not have any benefit in terms of accuracy, while its computational cost is higher. Therefore, if one wants to consider variable thermal properties, Newton's method is not recommended. The result of this analysis confirms the validity of the constant properties assumption.

As a consequence of the comparative assessment, the 1D model with constant properties is deemed to be the most representative model for modelling heat transfer phenomena in NHF panels' fingers.

Convergence analysis

The following step towards the definition of a suitable thermal model for NHF panel's fingers in terms of a trade-off between accuracy and computational cost is a convergence analysis. As the grid size in the x direction is already fixed from the analysis on the 1D semi-infinite model, as discussed in section 4.1.2, the convergence analysis is focused on the choice of the time step of the simulation Δt. The convergence analysis on Δt is carried out by employing a step

response heat flux and an exponential heat flux, as for the thermal model for EHF panel's fingers. That being the case, the convergence analysis is carried out by investigating the impact of different time steps on the solution with the two types of heat flux signals mentioned above. Results are shown in figure 4.22.

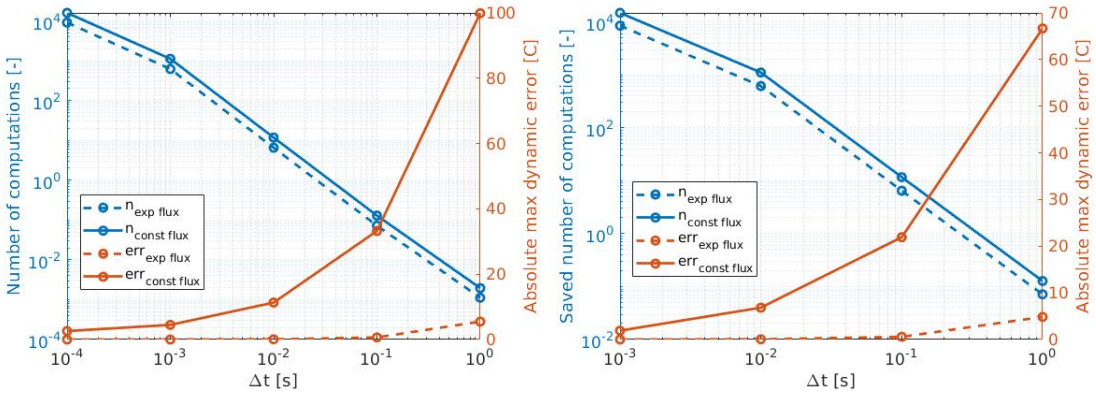

(a) (b)

Figure 4.22: Results of time convergence analysis for a step input heat flux and an exponential heat flux. Error and number of computations in absolute terms (a), and in marginal terms (b).

As shown in the figure and as is valid for EHF model, while the number of computations for the two types of heat fluxes is of the same order of magnitude, the error committed in case of a delay of the step response signal is higher than that of the exponential signal for the same Δt. Compared to EHF panels, in this case, the error committed for the same Δt is lower. The chosen Δt, result of a compromise between accuracy and computational cost, is $\Delta t = 1e-2$ s, which determines an error of approximately 10 °C in the case of the step response signal (in absolute terms). It is important to underline that the convergence analysis itself should be replicated several times as the number of computations in the ITER cluster is not deterministic. This is left for further studies, therefore the number of computations in the figure is to be considered indicative of the computational cost. At this point, having carried out a comparative assessment and a convergence analysis, it is possible to conclude that the 1D thermal model with constant properties with $N_x = 108$ nodes in the x direction and with a $\Delta t = 1e-2$ s represents the most suitable control-oriented model in terms of a trade-off between accuracy and computational cost for modelling heat transfer phenomena occurring in NHF panel's fingers. Once this is established, a further analysis on the HTC is hereafter presented.

HTC

A similar sensitivity analysis on the HTC as for EHF panel's fingers is performed. The results is reported in figure 4.23. Compared to EHF panels, the surface temperature is more sensible, therefore the HTC has to be evaluated more carefully.

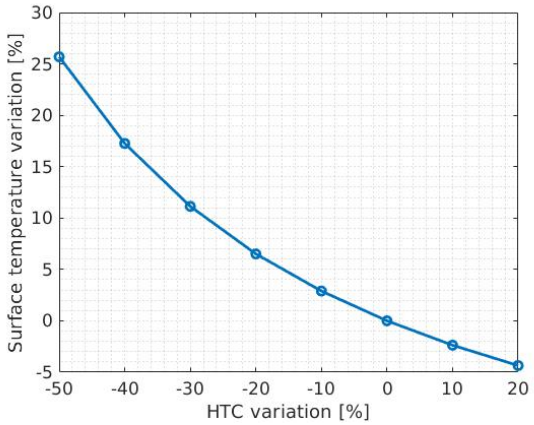

Figure 4.23: Sensitivity analysis on the HTC, showing the impact of its variation on the variation of the surface temperature in steady-state conditions.

4.1.5 TFW panels

In this section, the results for TFW panels, depicted in figure 4.24, are presented and discussed. For the sake of conciseness, only the results of the 1D model with constant properties and the 2D model with constant properties are presented, leaving the results of the variable properties aside. Subsequently, a comparative assessment is carried out. In particular, first, the 2D model is validated against a more accurate simulation to demonstrate the validity of the 2D assumption with a rectangular grid for the given finger. Afterwards, a comparison between 1D versus 2D models to assess the validity of the 1D assumption is performed. The following comparison is between the 2D model with constant properties with the 2D model with variable properties to assess the validity of using constant properties. The comparative assessment allows to find the most representative model for modelling heat transfer phenomena in TFW panels, namely a model capable of computing the thermal response of FWPs with sufficient accuracy while being as simple as possible at the same time. A convergence analysis of this model is then carried out to find a reasonable time step for the time simulation for RT application. At this point, a suitable model in terms of a trade-off between accuracy and computational cost is identified for TFW panels.

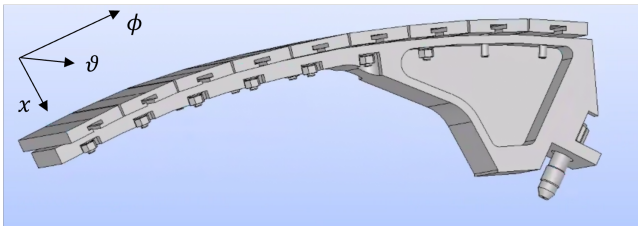

Figure 4.24: CAD file of TFW panel's fingers. Courtesy of ITER Blanket Section.

1D model with constant properties

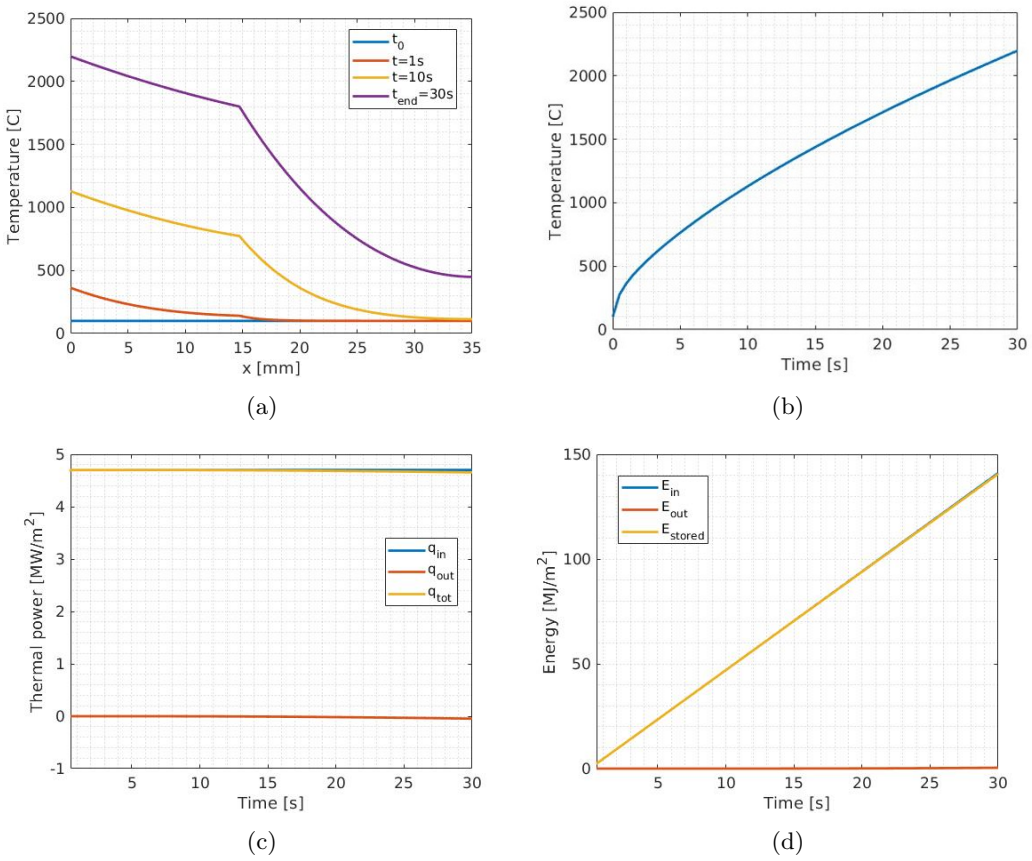

Figure 4.25: Results of 1D model for TFW panel's fingers: (a) temperature distribution; (b) surface temperature time evolution; (c) power flow; (d) energy conservation.

In the case of a 1D model of a finger along the x direction, the domain of interest is the one depicted in figure 3.7. With the hypothesis of constant properties, the discretization of the energy balance equation is equation 3.7, in which the Δx employed is the one discussed in section 4.1.2. The geometric values in figure 3.7 are taken as shown in figure 3.4. It is assumed the finger to be in thermal equilibrium with the surrounding structures at the beginning of the simulation. Subsequently, a constant heat flux of $q_s = 4.7$ MW/m^2 is applied. The final time of the simulation is 30 s. Results are shown in figure 4.25. As depicted in the figure, contrarily to actively-cooled FWPs, for TFW panels a steady-state condition is not reached. Indeed, as depicted in figure 4.25c, the thermal power out of the system transferred by diffusion and radiation heat transfer to the surrounding structures is significantly low compared to the input flux q_s, therefore the system does not reach equilibrium, thus the temperature continues to increase reaching considerably high values. That is why, in real operation conditions in the AFP phase, there will be a discharge phase for panels to be cooled down thanks to diffusion and radiation heat transfer (even if realistic heat loads are lower and not continuous). In other words, these results show that TFW panels' cooling is not significant while they are heated up, but instead are essential during the discharge phase. The energy conservation is respected: E_{in} linearly increases as q_s is constant, and almost the same as the stored energy, meaning that the average temperature in the system increases. Finally, the discontinuity in the first derivative visible in figure 4.25a is due to the different thermal properties of the two layers of W and SS.

2D model with constant properties

In the case of a 2D model of a finger along x and toroidal directions, the domain of interest is the one depicted in figure 3.8. With the hypothesis of constant properties, the discretization of the energy balance equation is equation 3.9. The thermal response of a TFW panel's finger is investigated by applying the incident constant heat flux q_s profile depicted in figure 4.26c. Results are reported in figures 4.26a and 4.26b.

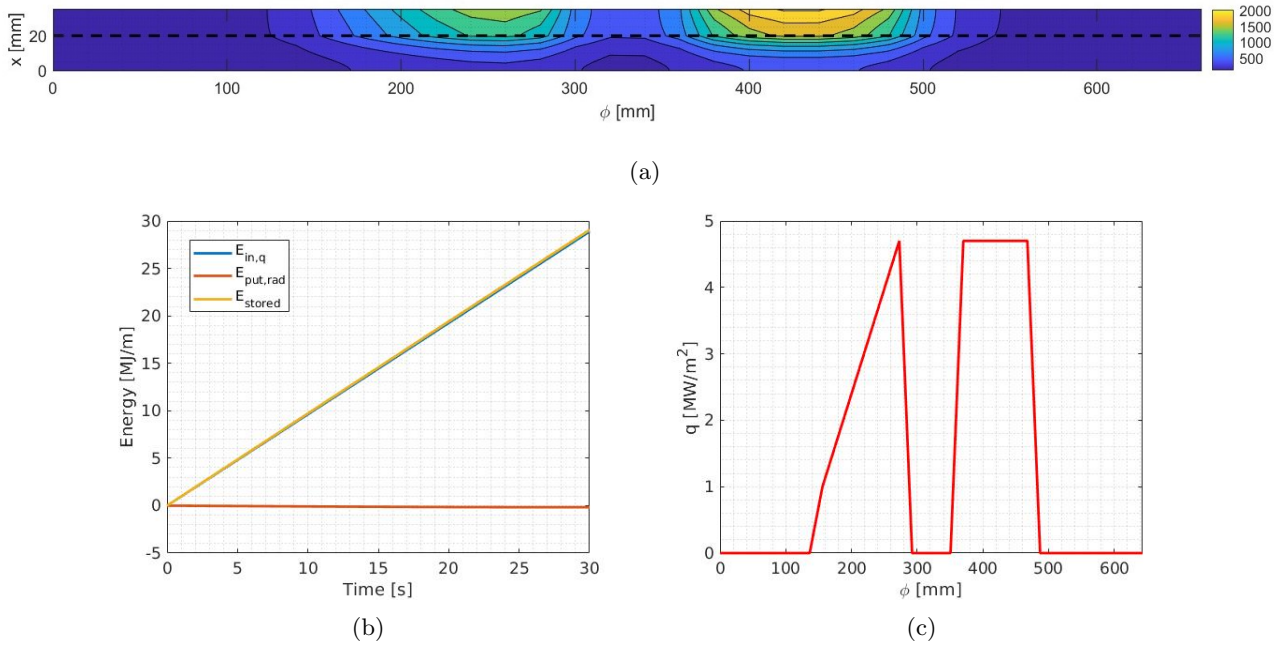

Figure 4.26: TFW panel's finger 2D model: (a) temperature distribution at the end of the simulation (the dashed black horizontal line divides the two layers); (b) energy conservation; (c) Incident heat flux q_s toroidal profile applied to the domain depicted in figure 3.8.

As it is possible to observe from the figure, the energy conservation demonstrates the validity of the model, as E_{in} linearly increases (consistently with the incident heat flux being constant) and E_{stored} is almost the same as E_{in} because E_{out} is very low, exactly as for 1D model. As shown in the available current design of TFW panel's fingers 2.14, W tiles are mechanically separated by toroidal gaps, which are not taken into account in the model whose results are shown above. However, toroidal gaps may significantly affect the temperature distribution because they interrupt heat diffusion along the toroidal direction. For this reason, another 2D model is developed including the presence of toroidal gaps in a simplified way by putting to zero the diffusion along the toroidal direction for those nodes placed

astride toroidal gaps belonging to the W layer. This model employs the same incident heat flux. Results are reported in figure 4.27. As it is possible to observe, the maximum temperature, which occurs in the region in which the heat flux is constant, does not change with respect to the model without toroidal gaps. However, the toroidal diffusion is less in the region in which there is a high gradient of the thermal flux in the toroidal direction, ending up with higher temperatures in that region. As expected, the energy conservation yields the same result as before as the incident heat flux is the same.

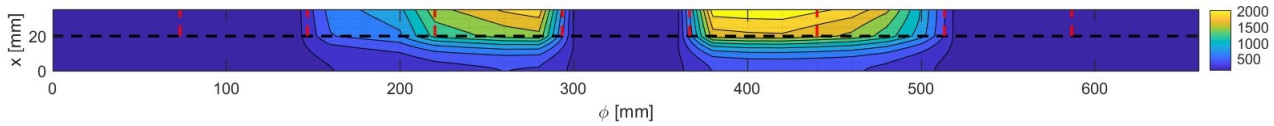

(a)

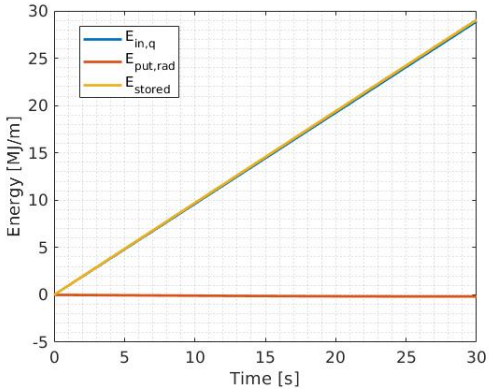

(b)

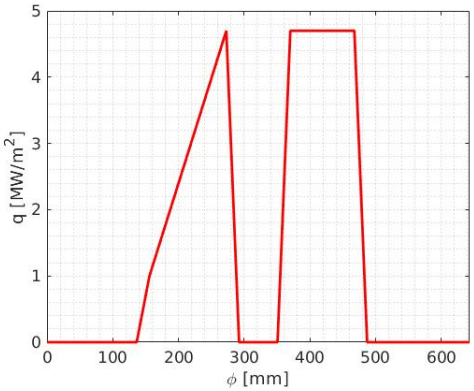

(c)

Figure 4.27: TFW panel's finger 2D model with toroidal gaps: (a) temperature distribution at the end of the simulation with the toroidal gaps schematically represented (the dashed black horizontal line divides the two layers and the dashed red vertical line represents toroidal gaps); (b) energy conservation; (c) Incident heat flux q_s toroidal profile applied to the domain depicted in figure 3.8.

Comparative assessment

In order to find the most representative model for heat transfer phenomena occurring in TFW panel's fingers, a comparative assessment is carried out. Firstly, with the goal of assessing the validity of the 2D model with a rectangular grid, the 2D model is validated against a more accurate simulation available, namely the 3D simulation carried out in Ansys simulating 6 plasma pulses shown in figure 4.1 [Deliege, 2024]. The same heat load is employed. This 3D simulation not only includes toroidal gaps between W tiles but also the bolts providing a mechanical connection of W tiles to the underneath SS structure. Bolts play a significant role in the heat transfer as they constitute a thermal bridge. In order to take into account the presence of bolts in a simple way, the heat conductivity of the SS layer is artificially lowered to the 3.5 % of its original value. The results of the validation are presented in figure 4.28, which contains the comparison between the maximum temperature during the 6th pulse obtained with the 3D simulation and the maximum temperature during the same pulse obtained with a simple 2D model. A comparison with the maximum temperature during the same pulse obtained with both a 2D model having toroidal gaps and a 2D model having both toroidal gaps and bolts is also included. The 2D model with both toroidal gaps and bolts follows approximately the same trend as the maximum temperature time evolution of the 3D simulation. This 2D model actually overestimates the temperature during the discharge phase, and this is due to the definition of the equivalent heat transfer coefficient reported in section 4.1.1, which approximates heat transfer phenomena in the finger through a 0D model. As shown in the figure, bolts play an essential role in the heat transfer, leading to very high temperatures. Moreover, the energy conservation indicates that the stored energy becomes periodic after the first two pulses, consistently with the maximum temperature time evolution being periodic (shown in figure 4.1). The energy conservation is the same for each version of the 2D model developed. This comparison demonstrates that by increasing the complexity of the 2D model, it is possible to get similar results as for the 3D simulation, thus validating the 2D model approximation with a rectangular grid. For the sake of clarity, figure 4.29 depicts the 2D temperature distribution at the moment

of maximum heat load during the 6th pulse in which toroidal gaps and bolts are included in the model. It is evident that heat diffusion is essentially localized to the single W tiles, leading to high temperatures.

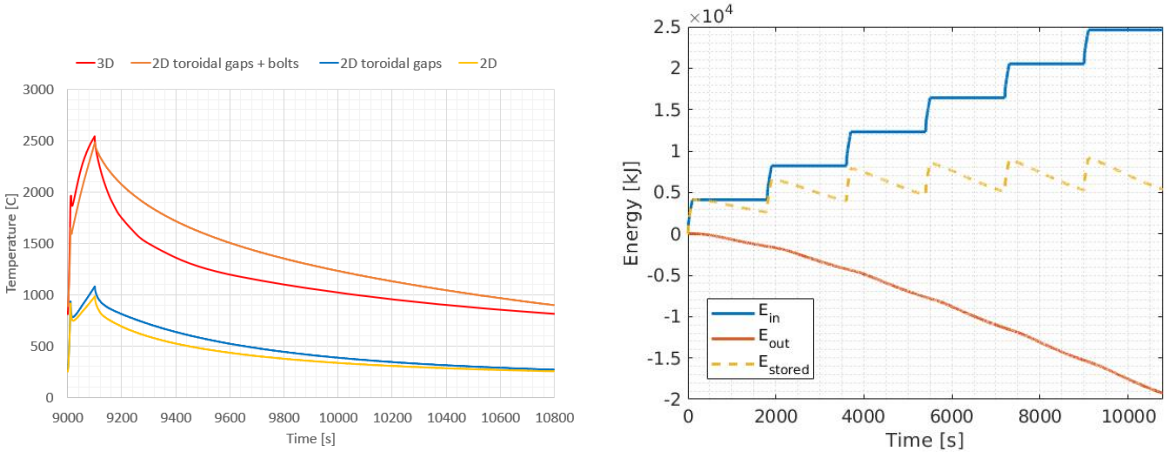

(a) (b)

Figure 4.28: Results of the validation for TFW panels: (a) maximum temperature time evolution during the 6th pulse (with reference to the 3D simulation reported in figure 4.1); (b) energy conservation during all the 6 pulses.

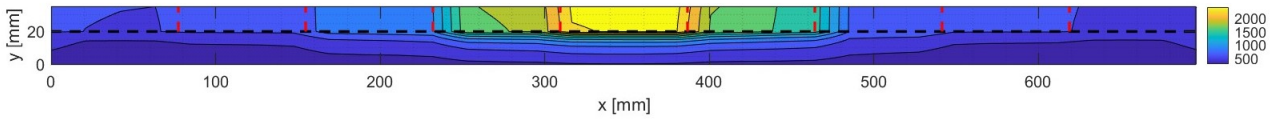

Figure 4.29: 2D temperature distribution at 9100 s (with reference to figure 4.28a).

The following comparison is between the 1D model with constant properties with the 2D model with constant properties with the goal of verifying the 1D approximation. Initially, the presence of both toroidal gaps and bolts is neglected. As shown in figure 4.30, the comparison is performed at the final time step of the simulation in different sections of the domain, a section having a high toroidal thermal gradient in the incident heat flux, and a section in which the incident heat flux is toroidally uniform. Along the first section, the 1D model excessively overestimates the temperature, due to the fact that it does not take toroidal diffusion into account. Along the second section, in which the thermal gradient in the toroidal direction is lower, the 1D model is closer to the 2D but still with a difference of 200 °C in terms of surface temperature. Therefore, it seems that the 1D model does not accurately represent heat transfer phenomena in TFW panels. In order to be sure about the validity of the 1D model with respect to the 2D model, an additional analysis is done by comparing the 1D model with a 2D model with toroidal gaps which, by interrupting the diffusion in the toroidal direction, make the 1D model closer to the 2D in terms of temperature distribution. Bolts are not included in this comparison as they do not play a role in interrupting the diffusion. Results are shown in figure 4.31. While the comparison between 1D and 2D models along section 2 is substantially the same as before, the comparison along section 1 shows that the 2D model profile with toroidal gaps is closer to the 1D model than before with a difference of 300 °C in terms of surface temperature. This difference is deemed to be enough to choose the 2D model as the most representative, despite the higher computational cost (as reported in figure 4.32). Therefore, the 1D approximation is deemed not to be valid and a 2D model is necessary. In particular, the 2D model with both toroidal gaps and bolts is deemed to be the most representative model for modelling heat transfer phenomena in TFW panel's fingers.

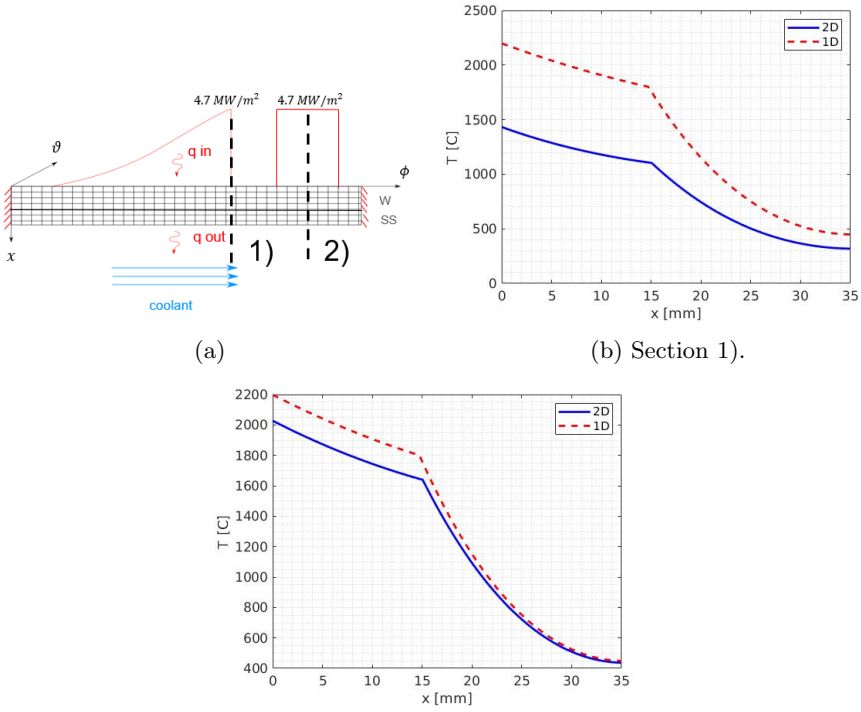

(a) (b) Section 1).

(c) Section 2).

Figure 4.30: Comparison between 1D and 2D models in terms of accuracy in two different sections at the final time step of the simulation. (a) sections of interest; temperature distribution along sections 1 (b) and 2 (c).

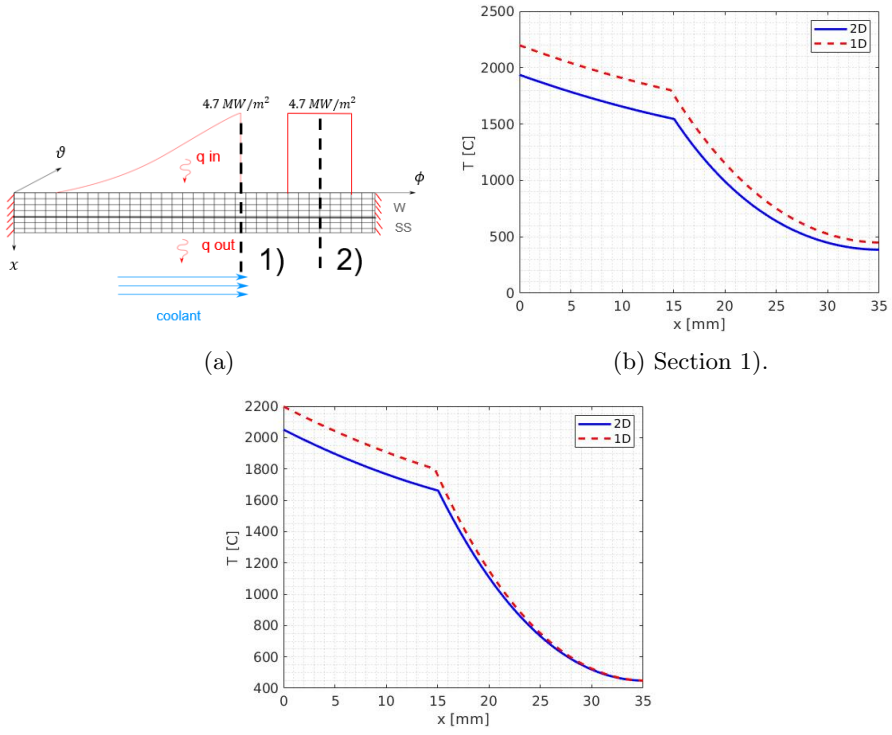

(a) (b) Section 1).

(c) Section 2).

Figure 4.31: Comparison between 1D model and 2D model with toroidal gaps in terms of accuracy in two different sections at the final time step of the simulation. (a) sections of interest; temperature distribution along sections 1 (b) and 2 (c).

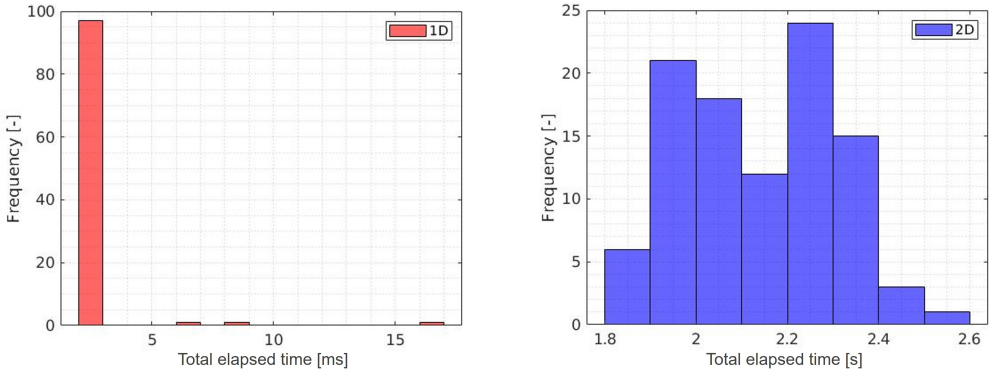

(a) (b)

Figure 4.32: Comparison between 1D and 2D models in terms of computational cost, measured as simulations' elapsed time: (a) computational time distribution for the 1D model; (b) computational time distribution for the 2D model. Note the different time scales, ms for the 1D model and s for the 2D model. The statistical distribution is obtained by performing 100 simulations in ITER computing cluster.

Following, the influence of variable properties is investigated. The properties of the model with constant properties are evaluated taking the average value in the temperature range for which the correlation is available. As for the other FWPs Newton's method proved not to have any added value compared with the FC method, only the latter is employed. Results are reported in figure 4.33.

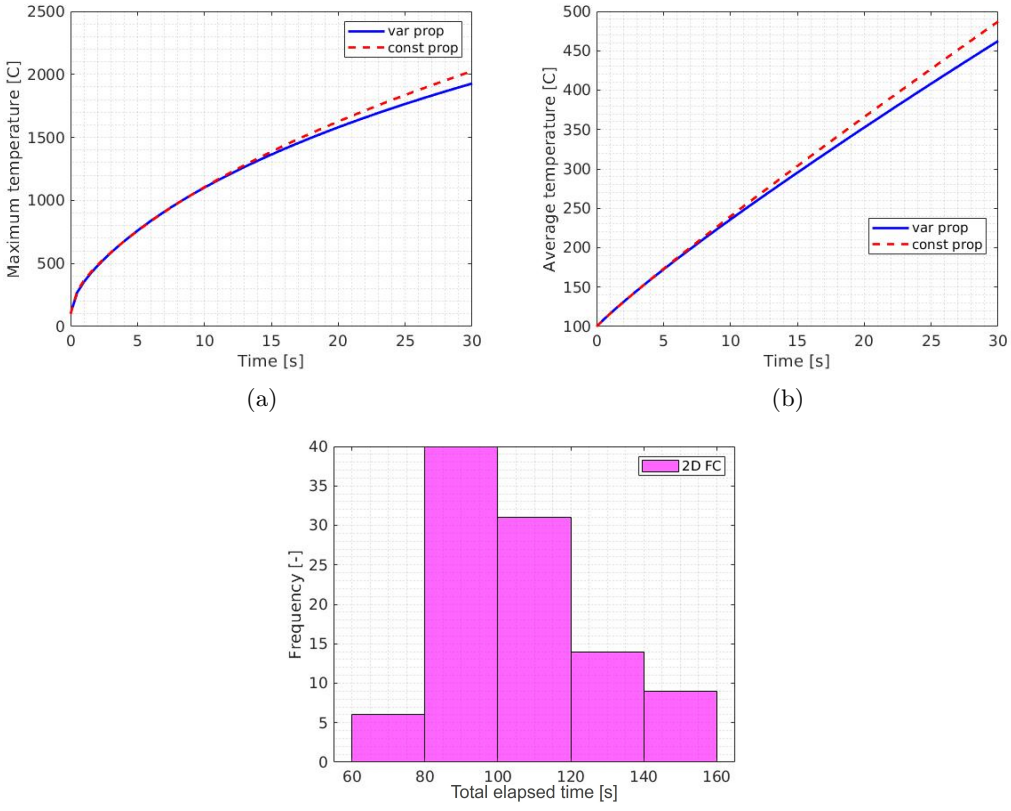

(a) (b)

(c)

Figure 4.33: Comparison between 2D model with constant properties and 2D model with variable properties solved with FC method. (a) Time evolution of the maximum temperature; (b) time evolution of the average temperature; (c) elapsed time for the 2D model with variable properties.

From the above figure, it is evident that accounting for temperature-dependent properties does not add any relevant benefit in terms of accuracy and, on top of that, it implies a high computational cost as it may be observed by comparing figures 4.32b and 4.33c. This analysis confirms the validity of constant properties assumption.

As a consequence of the comparative assessment, the 2D model with constant properties is deemed to be the most representative model for modelling heat transfer phenomena in TFW panels' fingers.

Convergence analysis

The following step towards the definition of a suitable thermal model for TFW panel's fingers in terms of a trade-off between accuracy and computational cost is a convergence analysis. As the grid size in the x direction is already fixed from the analysis on the 1D semi-infinite model, as discussed in section 4.1.2, the convergence analysis is focused on the choice of both the number of nodes in the toroidal direction N_ϕ (space convergence) and the time step of the simulation Δt (time convergence).

Concerning the space convergence, the discretization error is computed in relative terms by comparing the maximum temperature computed for a certain number of grid points in the toroidal direction k with a more accurate reference case (specifically, 129 nodes), namely $e_{space}(k) = \frac{|T_{max,ref} - T_{max,k}|}{|T_{max,ref} - T_{water}|}$. T_{water} is included in the denominator in order to make the error independent from the temperature unit used (°C or K). The maximum temperatures are evaluated at the final time of the simulation, which is 30 s. Additionally, also the marginal error is computed as $e_{space\ marginal}(k) = \frac{|T_{max,k} - T_{max,k-1}|}{|T_{max,k-1} - T_{water}|}$, together with the computational cost for each grid size computed as elapsed simulation time. Results are reported in figure 4.34. As shown in the above figure, the discretization error decreases for higher nodes in the toroidal direction at the expense of the computational cost. As a trade-off between accuracy and computational cost, it is chosen to employ $N_\phi = 34$ nodes in the toroidal direction, which determines a relative error of 15 % (in absolute terms).

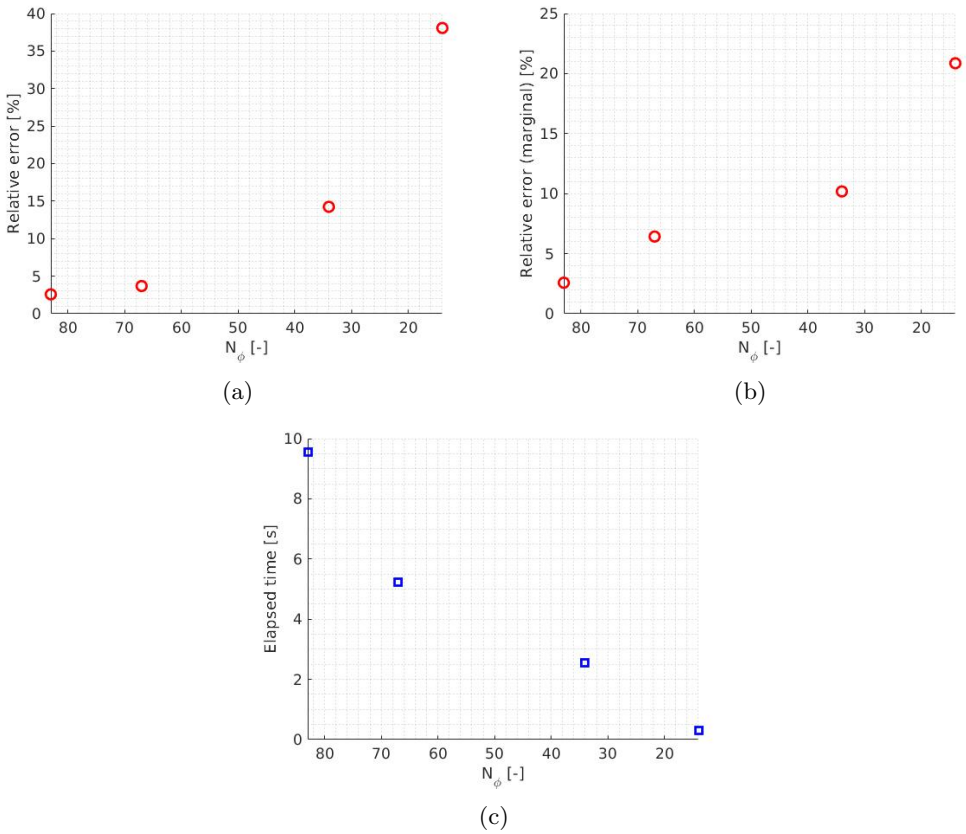

Figure 4.34: Convergence analysis for TFW panel's finger : (a) relative error for different nodes in the toroidal direction; (b) relative error for different nodes in the toroidal direction in marginal terms; (c) elapsed time for different nodes in the toroidal direction.

Concerning the time convergence, the discretization error is computed in relative terms by comparing the maximum temperature computed for a certain time step k with a more accurate reference case (specifically, $\Delta t = 1e-4$ s), namely $e_{time}(k) = \frac{|T_{max,ref} - T_{max,k}|}{|T_{max,ref} - T_{water}|}$. The maximum temperatures are evaluated at the final time of the simulation, which is 30 s. Additionally, also the marginal error is computed as $e_{timemarginal}(k) = \frac{|T_{max,k} - T_{max,k-1}|}{|T_{max,k-1} - T_{water}|}$, together with the computational cost for each Δt computed as elapsed simulation time. Results are reported in figure 4.35. As shown in the figure below, the discretization error decreases for smaller Δt at the expense of the computational cost. As a trade-off between accuracy and computational cost, it is chosen to employ $\Delta t = 0.1$ s, which determines a relative error of $4e-4$. It is important to underline that the convergence analysis itself should be replicated several times as the number of computations in the ITER cluster is not deterministic. This is left for further studies, therefore the number of computations in the figure is to be considered indicative of the computational cost.

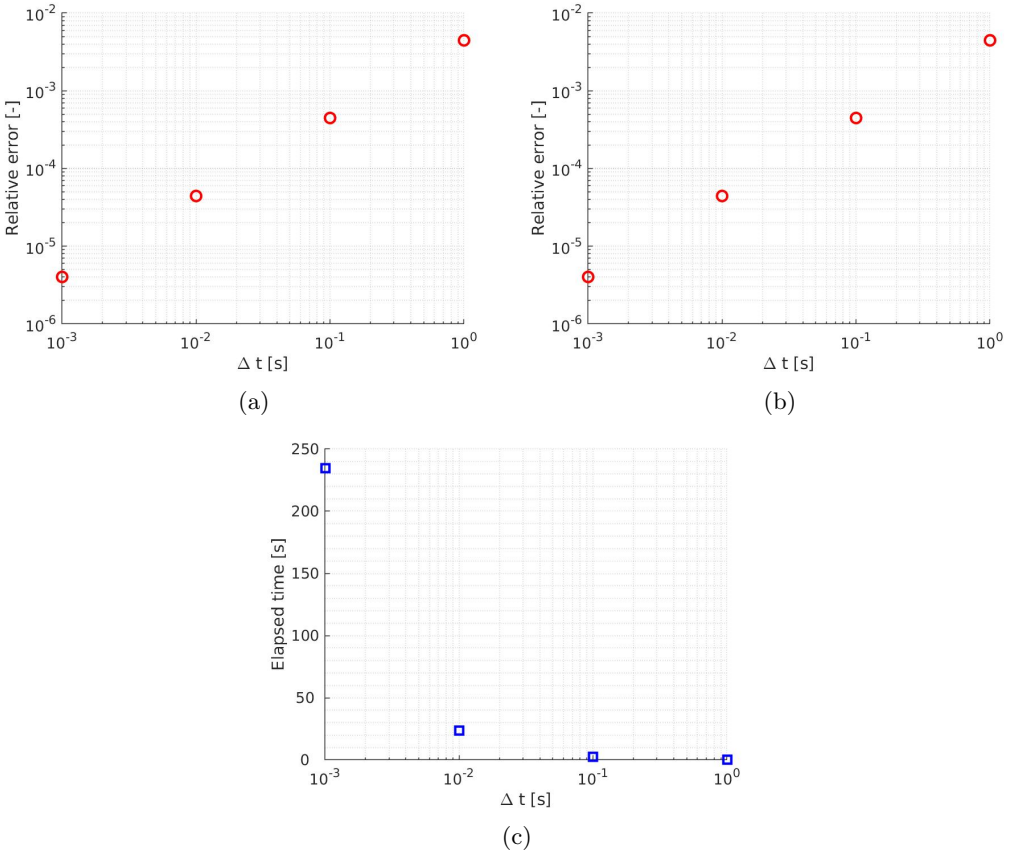

Figure 4.35: Time convergence analysis for TFW panel's finger : (a) relative error for different Δt; (b) relative error for different Δt in marginal terms; (c) elapsed time for different Δt.

At this point, having carried out a comparative assessment and a convergence analysis, it is possible to conclude that the 2D thermal model with constant properties with $N_x = 108$ nodes in the x direction, $N_\phi = 34$ nodes in the toroidal direction, and with a $\Delta t = 0.1$ s represents the most suitable control-oriented model in terms of a trade-off between accuracy and computational cost for modelling heat transfer phenomena occurring in TFW panel's fingers.

4.1.6 Sum-up of the main results

The following table sums up the main results of the thermal modelling for FWHLC in RT in the AFP phase. In particular, concerning the results of convergence analyses, the models developed have proved to be computationally efficient as elapsed simulation times are lower than the time steps used in the models. This demonstrates the suitability of the models for controller design and RT application.

Analysis carried out	Main assumptions	Main results
Definition of an equivalent HTC for TFW panel's fingers cooling phase	- 0D approximation - artificial heat load used for design purposes - HTC defined in such a way as to accurately estimate the final temperature of a discharge phase rather than the temperature during the transient	- TFW panel's fingers cooling phase modeled in a simple way - HTC valid in the case of high temperatures - definition of a HTC similar as for EHF and NHF panels, so increased model flexibility
Comparison between 1D semi-infinite and 1D simplified models	- constant thermal flux of 4.7 MW/m^2 - slab length of 100 mm - simulation final time: 1 s	- $\Delta x = 1e-4$ m for EHF panels, corresponding to $N_x = 108$ nodes. Error of 2 °C (infinity norm) - $N_x = 108$ nodes also for NHF and TFW panels, leading to an error of 10 °c (infinity norm)
Comparative assessment for EHF panels	- heat flux constant in time and having 4.7 MW/m^2 as maximum value - validation of the 2D model with a rectangular grid with 2D simulation with toroidal curvature solved with the FV method	- 1D model is optimal, despite a difference of around 30 °C with respect to the 2D model - constant properties approximation is optimal, having no significant difference compared to the results with models considering variable properties (both FC and Newton's method)
Convergence analysis for EHF panels	- two types of heat fluxes: step signal and exponential, both having 4.7 MW/m^2 as maximum value	- $\Delta t = 1e-2$ s leads to an error of 25 °C in the case of a step signal - with $\Delta t = 1e-2$ s = 10 ms the elapsed time of a single time step is 0.2 ms
Comparative assessment for NHF panels	- heat flux constant in time and having 4.7 MW/m^2 as maximum value	- 1D model is optimal, despite a difference of around 45 °C with respect to the 2D model - constant properties approximation is optimal, having no significant difference compared to the results with models considering variable properties (both FC and Newton's method)
Convergence analysis for NHF panels	- two types of heat fluxes: step signal and exponential, both having 2 MW/m^2 as a maximum value	- $\Delta t = 1e-2$ s leads to an error of 10 °C in the case of a step signal - with $\Delta t = 1e-2$ s = 10 ms the elapsed time of a single time step is 0.2 ms
Comparative assessment for TFW panels	- heat flux constant in time and having 4.7 MW/m^2 as maximum value - validation of the 2D model with a rectangular grid with a 3D simulation having a periodic heat load in time	- 2D model is optimal, as the 1D model excessively overestimates the temperature - if TFW panel's fingers are characterized by toroidal gaps and/or bolts, they should be taken into account for higher accuracy - the influence of variable properties is negligible
Convergence analysis for TFW panels	- heat flux constant in time and having 4.7 MW/m^2 as maximum value	- $N_\phi = 34$ leads to a relative error of 15 % - $\Delta t = 0.1$s = 100 ms leads to a relative error of 1e-3 % - the elapsed time of a single time step is 10 ms

Table 4.1: Sum-up of the main analyses and results for FWHLC in RT in the AFP phase.

4.1.7 PCS integration and FW thermal response

Comparative assessments and convergence analyses carried out so far for each type of FWP constitute a systematic approach to identifying the most suitable control-oriented model in terms of a trade-off between accuracy and computational cost for the design and RT operation of the FWHLC in the AFP phase. At this point, the thermal models developed can be integrated into the PCS and the FW thermal response can be investigated under realistic time-dependent heat loads coming from simulations including plasma dynamics.

Concerning the integration in the PCS, it is fundamental to respect the formalism of the PCSSP in Simulink, in which the matrices containing the discretization of the heat transfer process are characterized by a state-space representation. The thermal models integrated into the PCSSP look qualitatively like in figure 4.36. With reference to this figure, uu_{sim} contains the time series of the model input (i.e., the heat flux and the coolant temperature), while *out.simout* contains the desired output of the model, namely the fingers' surface temperature at each time step. It is also possible to observe that the Simulink block in the middle of the figure contains the state-space representation of the matrices.

As said before, with the models developed within this work is possible to evaluate the surface temperature distribution in RT with time-dependent heat fluxes for selected fingers of any FWP. As an example, figure 4.37 provides the maximum temperature time evolution for selected fingers belonging to FWP 3 given some realistic time-dependent heat loads. It is assumed FWP 3 to be a TFW panel. In the figure, the plasma state is distinguished into the limited, diverted in L mode, and diverted in H mode phases. As stated in section 2.4, when the plasma is limited FWPs are subjected to a higher heat flux due to the vicinity of the plasma to the FW, while when the plasma is diverted in L mode the heat flux is considerably low as it is mostly directed to the divertor, indeed the temperature drops in this

phase. When the plasma is diverted in H mode, the FW receives the heat flux coming from ELMs, which causes a temperature increase.

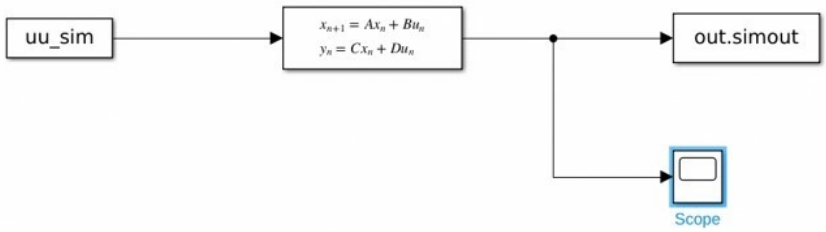

Figure 4.36: State-space qualitative representation in Simulink of the thermal models developed and integrated in the PCSSP.

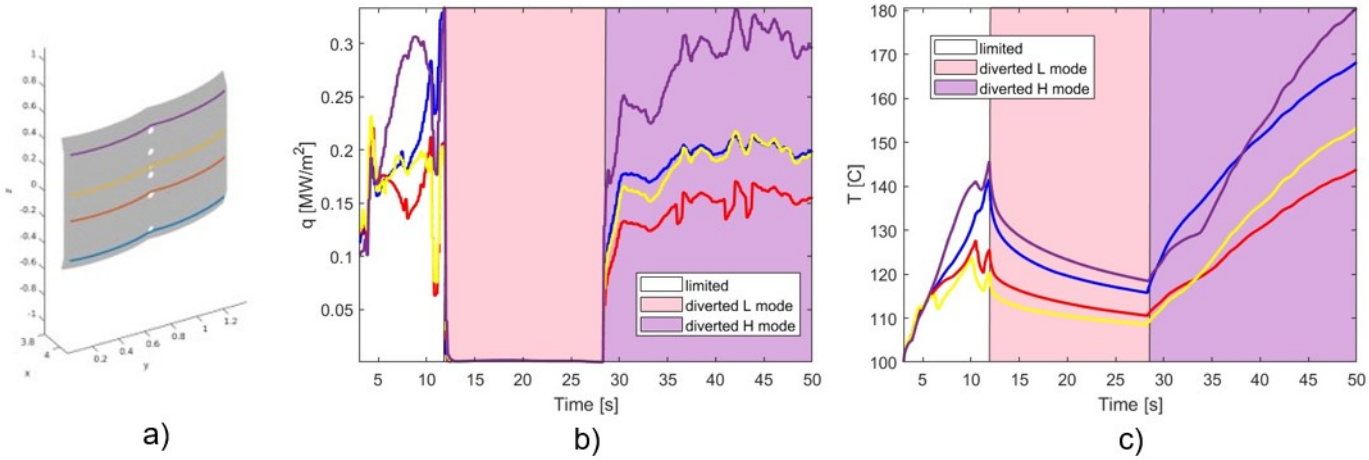

Figure 4.37: Results of the thermal models developed in this work applied to FWP 3, assumed to be a TFW panel: (a) selected fingers on FWP 3; (b) thermal flux time evolution (maximum value) on the selected fingers; (c) temperature time evolution (maximum value) on the selected fingers. Note that thermal flux and temperature time evolution on selected fingers are marked by a color corresponding to the specific finger.

An important conclusion that is possible to draw from the above picture is that the characteristic time of heat transfer, essential for the controller design, is of the order of seconds. This is consistent with the thermal models developed in the case of constant artificial heat flux, indeed the time steps employed are $\Delta t = 1e-2$ s for EHF and NHF panels and $\Delta t = 0.1$ s for TFW panels. Therefore, is it possible to conclude that the thermal models developed within this work are suitable to be applied in the case of realistic heat loads, as the heat transfer dynamic is correctly modelled.

Additionally, the application of thermal models developed is not restricted to the fingers of a FWP only, but it can be extended to selected fingers belonging to the entire FW as shown in figure 4.38. This is consistent with one of the requirements of the model of being general, i.e., being applicable to any finger in the FW, as stated in section 1.2. From the figure, it is evident that the maximum temperatures reached are significantly lower than the temperature ranges shown in section 4.1.5. The reason is that heat fluxes profiles used in section 4.1.5 are artificial and correspond to panels' design limit, while realistic heat fluxes do not approach these limit values.

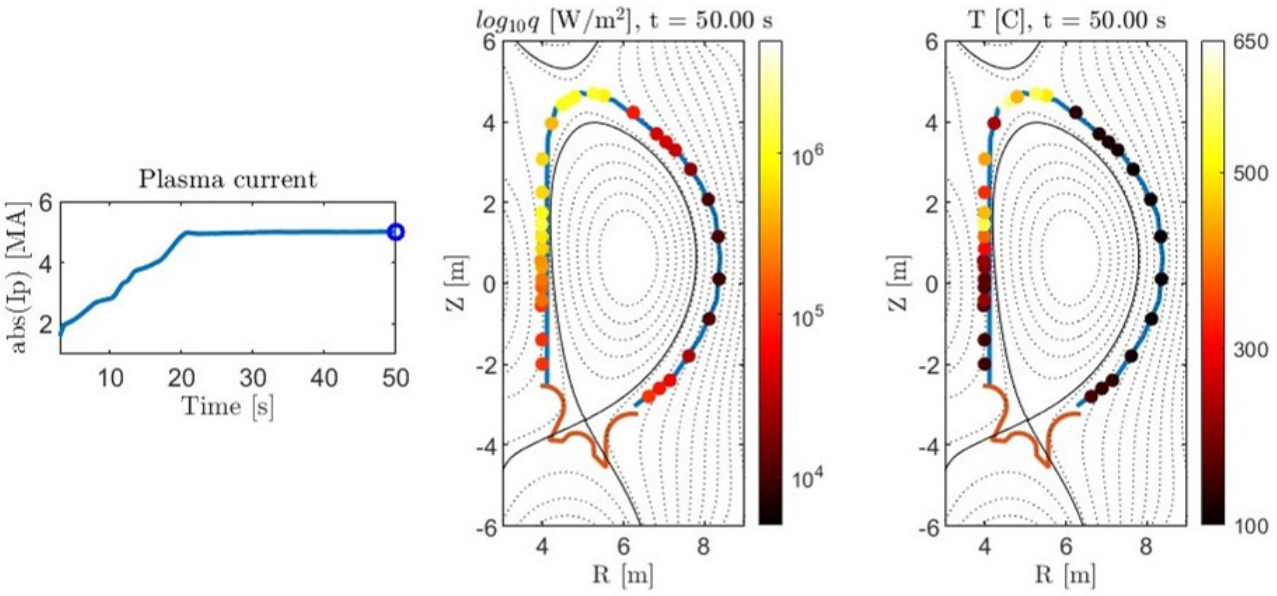

Figure 4.38: Application of the thermal models developed in this work to selected fingers (represented with dots) spread around the FW. All the FWP are assumed to be TFW panels. The figure on the left shows the time evolution of the electric current, in which ramp-up and flat-top are clearly visible, while the other two figures show a snapshot of the maximum heat flux and maximum temperature on selected fingers (figure in the middle and on the right respectively) at the end of the simulation (corresponding to the plasma current identified by the blue circle in the left figure).

It is worthwhile to underline that in figure 4.38 only one single value of the temperature for each finger is provided (specifically, the maximum value), but fingers are characterized by a temperature distribution in space. In particular, as FWPs are assumed to be TFW panels, the underlying thermal model is the representative one for these panels, namely a 2D model with a rectangular grid, toroidal gaps, and bolts. Therefore, for the sake of clarity, figure 4.39 shows the space distribution of the incident heat flux at the end of the simulation (which is the same simulation as in figure 4.38) and the resulting 2D temperature distribution at the end of the simulation for one of the fingers of FWP 8, which is the one characterized by the maximum temperature.

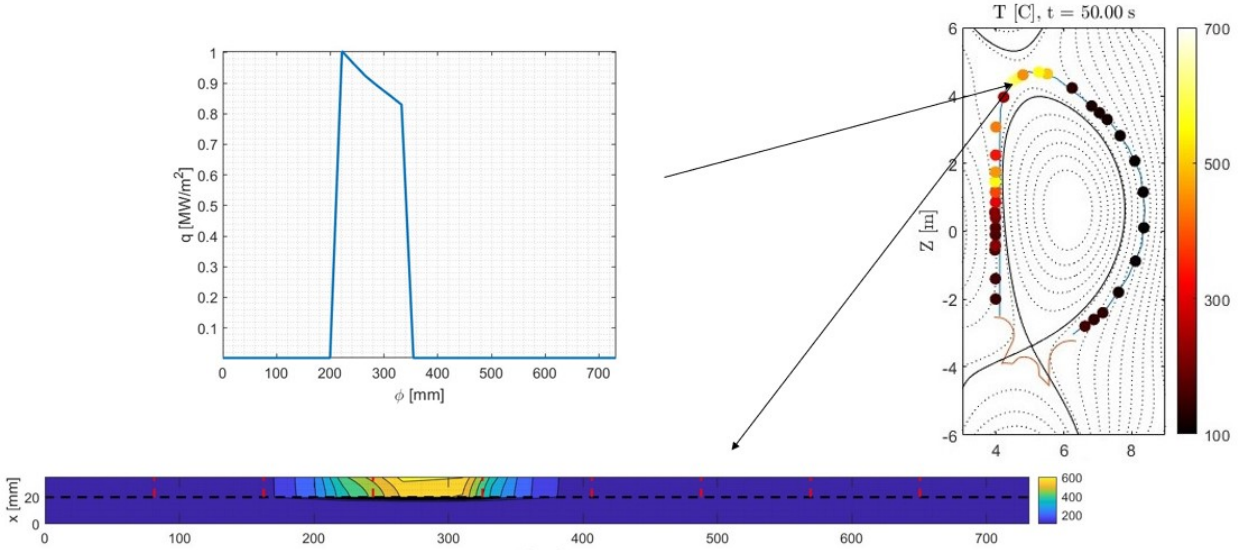

Figure 4.39: Heat flux distribution in space and 2D temperature distribution for one of the fingers of FWP 8. The distributions are relative to the final time of the simulation, which is the same as in figure 4.38.

4.1.8 Model reduction techniques

The computational performance of the models, which is summed up in table 4.1, can be improved through model reduction techniques, which are methods used to simplify complex mathematical models while preserving their essential behavior [Alla, 2022]. Among the several methods available in the literature, [Alla, 2022] employed a Proper Orthogonal Decomposition (POD) method, which consists of reducing the dimensionality by extracting the dominant modes only through orthogonal projections. [Skopec et al., 2021] applied a Balanced Truncation method to solve a 1D heat diffusion equation. This method is based on neglecting states that have a relatively low effect on the overall model response. [Gerardin et al., 2016] developed reduced thermal models to evaluate the surface temperature of PFCs based on the concept of thermal quadrupole, which consists of representing the heat flow using equations similar to those in electrical circuits through Laplace transforms. [Bhikkaji and Söderström, 2001] applied the method of singular perturbations for the heat diffusion process in a homogeneous wall. This method is effective when the system is characterized by components having significant differences in terms of time scales and involves approximating the dynamics of the fast and slow components separately. [Tadjeran and Meerschaert, 2007] applied the Alternating Direction Implicit (ADI) method to a 2D heat diffusion equation. This method consists of solving the heat diffusion equation in one direction, calculating an intermediate temperature distribution, and finally solving the diffusion in the other direction.

In order to understand the working principle of the ADI method, a simple model has been developed. In particular, by considering a squared domain of unitary length having an initial temperature of 100 °C and boundary conditions of a constant temperature of 0 °C, the time-dependent 2D heat diffusion equation has been solved with an ADI method and with a Crank-Nicolson discretization scheme. In particular, to evaluate the temperature distribution at the time step $m+1$, this method consists of solving the following system of equations at each time step:

$$\begin{cases} T^* = \underline{\underline{A_x}}^{-1} \cdot \left(\underline{\underline{A_y}} \cdot T^m \right) \\ T^{m+1} = \left(2\underline{\underline{I}} - \underline{\underline{A_y}} \right)^{-1} \cdot \left[\left(2\underline{\underline{I}} - \underline{\underline{A_x}} \right) \cdot T^* \right] \end{cases} \tag{4.9}$$

where T^m is the temperature distribution at the previous time m, T^* is the intermediate temperature distribution, $\underline{\underline{A_x}}$ the matrix containing the heat diffusion along the x direction, $\underline{\underline{A_y}}$ the matrix containing the heat diffusion along the y direction, and $\underline{\underline{I}}$ the identity matrix. Further details about the definition of the matrices and the boundary conditions are provided in Appendix E. In particular, $\underline{\underline{A_x}}$ is a tridiagonal matrix and $\underline{\underline{A_y}}$ a block-tridiagonal matrix. The advantage of the ADI method is that inverting a tridiagonal matrix $\underline{\underline{A_x}}$ and a block-tridiagonal matrix $\underline{\underline{A_y}}$ should be computationally faster than inverting the matrix $\underline{\underline{A_{tot}}} = \underline{\underline{A_x}} - \underline{\underline{A_y}}$ which corresponds to the penta-diagonal matrix that should be inverted without applying the ADI method. The performance in terms of the computational cost of this simple model has been tested on MATLAB in the ITER computing cluster. The results are the following:

- by assuming a total number of 10201 nodes, the elapsed time for inverting the matrix $\underline{\underline{A_x}}$ (which is 10201 X 10201) is around 1 ms, evaluated by using the command "backslash" in MATLAB, which applied Thomas algorithm for matrix inversion
- by assuming the same number of nodes as before, the elapsed time for inverting the matrix $\underline{\underline{A_y}}$ is around 7000 ms, evaluated by using the command "backslash" in MATLAB as well
- by assuming the same number of nodes as before, the elapsed time for inverting the matrix $\underline{\underline{A_{tot}}}$ is around 5000 ms

From these results, it is possible to conclude that the application of this ADI method is limited by the computational cost of inverting $\underline{\underline{A_y}}$, which is unexpectedly of the same order of magnitude as that of $\underline{\underline{A_{tot}}}$ inversion. This is probably due to the "backslash" command used in MATLAB, as it is possible that Thomas's algorithm is not optimized for block-tridiagonal matrices. In order to check the validity of this statement, another algorithm optimized for block-tridiagonal matrices has been employed to invert $\underline{\underline{A_y}}$ [von Winckel G., 2024]. The elapsed time with this algorithm is around 80 ms, about two orders of magnitude lower than with the "backslash" command in MATLAB. Therefore, before applying this method to the diffusion processes investigated in this thesis work, it is fundamental to deeply investigate how these algorithms work and possibly find suitable ones in order to efficiently invert block-tridiagonal matrices. In this way, the ADI method can constitute an advantage from the computational cost standpoint. This is left for further studies.

4.1.9 Comparison between implicit and explicit schemes

As previously stated in section 4.1.2 regarding the 1D semi-infinite model, due to the stringent stability requirement for the FE scheme, both 1D and 2D models have been developed using a BE scheme to achieve lower computational times. However, this choice has been based on the results of the 1D semi-infinite model only, therefore to check its validity a comparison between the computational times required with a FE scheme and with a BE scheme is carried out. Indeed, on the one hand, the FE scheme is limited by the stability requirement, but on the other hand the resulting $\underline{\underline{A}}$ matrix is sparse, and for sparse matrices multiplication algorithms are faster with respect to the ones of non-sparse matrices resulting from a BE scheme. Results reported in table 4.2 for the 2D model of TFW panel's fingers show that the model solved with a FE scheme is quite slow as the model time step is lower than the clock time. However, in the case of smaller matrices, which can be the case if a non-uniform grid is employed, the FE method could be faster than the BE method.

Method	Model time step [ms]	Clock time [ms]
BE 2D	100	10
FE 2D	1	23

Table 4.2: Comparison between the computational times for the 2D model with a rectangular grid of TFW panel's fingers solved with a BE method or with a FE method.

4.2 DT phase - IR cameras' synthetic diagnostics

As presented in the methodology chapter 3, for the sake of generating temperature maps for IR cameras' synthetic diagnostics in the DT phase, thermal flux data of a specific FWP evaluated through the SMITER code together with the geometric measures of the specific FWP and its cooling parameters, are used as input values for a thermal model in order to evaluate the surface temperature. This thermal model is developed for the flat-top phase, therefore in steady-state conditions, for which it has been demonstrated in section 4.1.4 that a 1D model with constant properties is the most representative model for actively cooled panels, the only ones envisaged to be installed in the DT phase.

For a given plasma equilibrium and FWP design, through SMITER code it is possible to evaluate the heat flux crossing the separatrix parallel to magnetic flux lines $q_{//}$ and identify FWPs' wetted areas. Consequently, the perpendicular heat flux $q_{\perp}$ to a given FWP can be evaluated. Figure 4.40 depicts the SMITER environment.

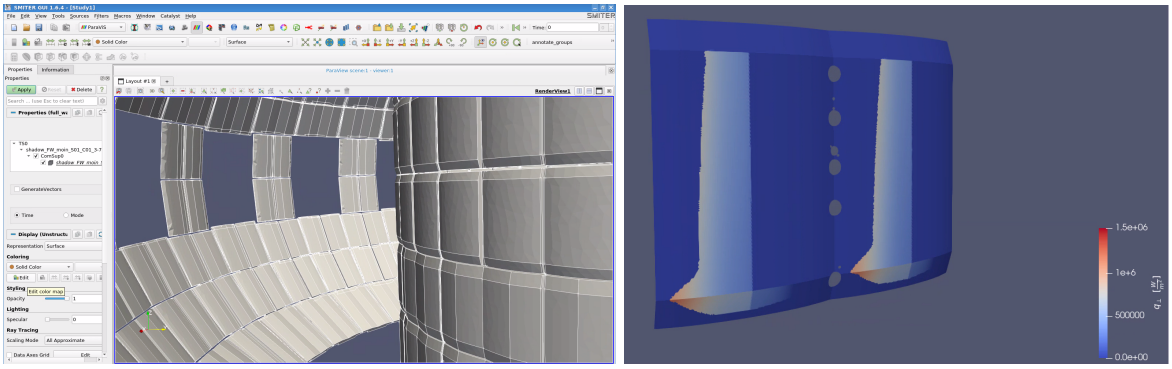

(a) (b)

Figure 4.40: SMITER environment: (a) User-interface showing the FWPs covering ITER FW; (b) particular of an example of the computed $q_{\perp}$ on FWP 3.

After having computed the perpendicular heat flux on a given FWP for each grid point defined in SMITER, thermal flux and geometric coordinates data (both defined for each grid point) are downloaded. In particular, every grid point of each FWP is uniquely defined in SMITER in cylindrical coordinates. For each grid point, the thermal model described in section 3.2 is run to evaluate the surface temperature in each grid point, taking into account how EHF and NHF panels are distributed along the FW (see figure 2.15). Figure 4.42 shows the temperature distribution on the FWP 3 as an example, which reflects the heat flux distribution depicted in figure 4.40b. Figure 4.42 shows the extension of the model to the entire FW by showing an ITER sector. As it is possible to observe, almost all the panels

do not exceed 200 °C therefore IR cameras, whose threshold for temperature measurement is indeed 200 °C, should be able to detect only the temperatures on FWPs 4 and 8 according to this simple model.

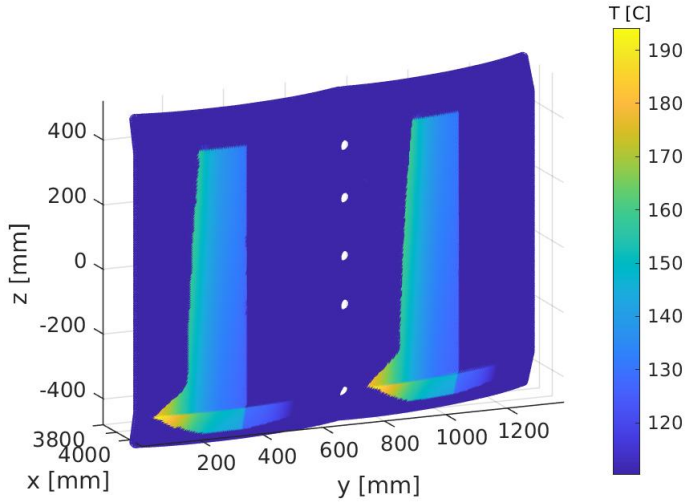

Figure 4.41: Steady-state surface temperature distribution on FWP 3 during the flat-top phase.

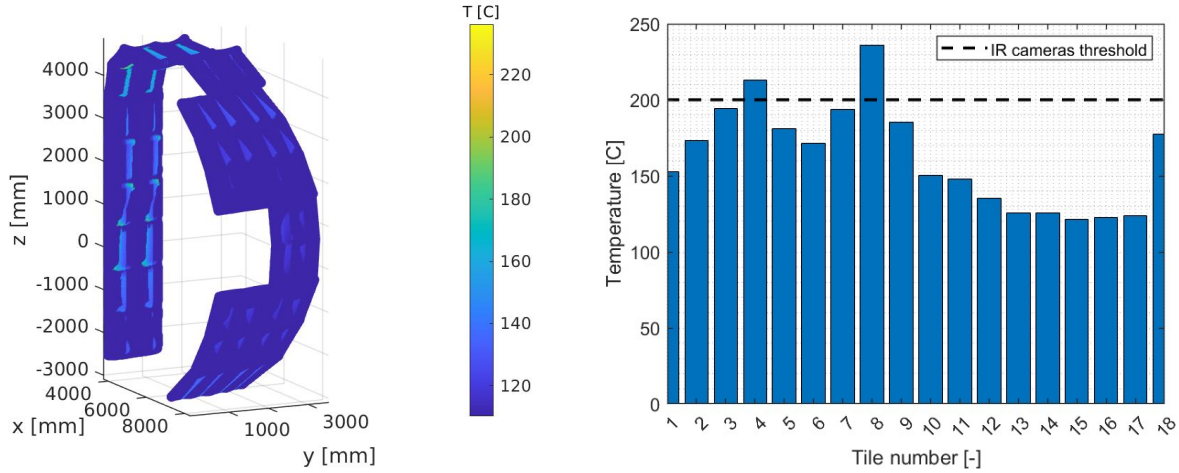

(a) (b)

Figure 4.42: Steady-state surface temperature distribution on ITER entire FW during flat-top phase: (a) ITER sector; (b) maximum temperature on each FWP.

One of the assumptions of this model, as mentioned in section 3.2, is relative to the calculation of volumetric heat generation, especially in the tungsten layer. Figure 4.43 shows the comparison in terms of maximum temperature reached in the case of volumetric heat generation (calculated as mentioned in section 3.2) and in the case of absence of volumetric heat generation. It is possible to observe that the difference is around 10 °C for EHF panels and around 40 °C for NHF panels. As the geometric values of these panels are comparable, probably the difference in terms of the maximum temperature reached for the two types of panels is due to the different HTC employed. In any case, the influence of the volumetric heat generation can be considered to be negligible with respect to the incident heat flux on FWPs, despite the volumetric heat generation being of the order of magnitude of tens of MW/m^3. The reason is probably that, even if volumetric heat generation is relatively high, the volume available for heat deposition is quite small, ending up in a relatively low heat deposited by neutrons compared to the incident heat flux. This justifies the conservative calculation of ϕ_W.

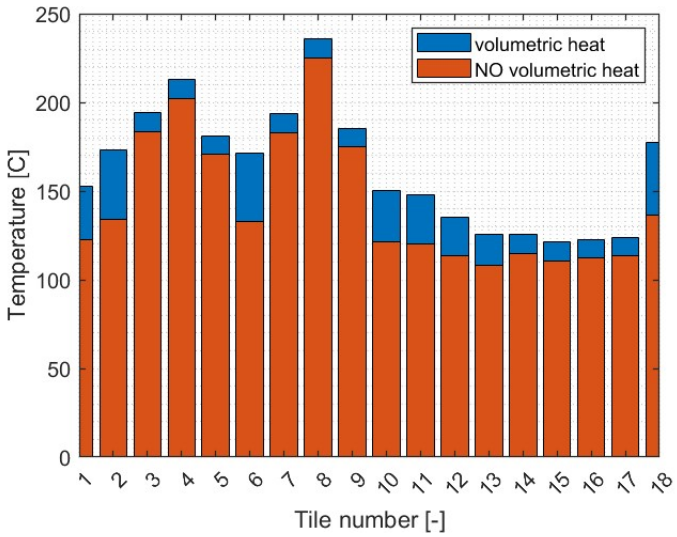

Figure 4.43: Comparison between models with and without volumetric heat generation in terms of surface temperature for every FWP.

At this point, the calculation method of volumetric heat fluxes is justified, and the surface temperature distribution computed for the entire FW is loaded on SMITER.

Chapter 5

Conclusions

This thesis work is inserted in the framework of the FWHLC, which provides a first line of defense for ITER FW in the case of undesired heat fluxes during nominal and off-nominal transients potentially leading to accidental events, with a particular focus on the thermal model for the FW. Research gaps, addressed in section 1.1, have been filled by fulfilling the goal of developing two types of thermal models, a control-oriented model for the design and RT operation of the FWHLC in AFP phase and a steady-state model for IR cameras' synthetic diagnostic in DT phase.

Concerning the first one, consistently with the requirements stated in section 1.2, a thermal model having the characteristics of being control-oriented and general has been developed for FWP's fingers in MATLAB. Fingers have been considered to be thermally independent, but this assumption has not been justified, therefore further studies are needed to investigate its validity, possibly in combination with high-fidelity CAD-based thermal models. Due to the ITER re-baseline, this work has been at the center of a research and development process, which has implied a continuous evolution of FW design. For this reason, an additional feature of this model, absent in the thermal models available in the literature, has been its flexibility in terms of FWPs type, geometry, and materials. Indeed, the model developed can be applied to any finger of any FWP depending on its type (EHF, NHF, TFW). The analyses have been carried out by employing the latest available design of FWPs shown in section 2.2.1 and assuming tungsten as plasma-facing material, with the possibility to easily modify these model inputs in the codes thus following the design evolution. The modelling approach has been divided into a part of comparative assessment and convergence analysis, both characterized by an artificial constant heat flux corresponding to panels' design limit, followed by a second part of integration into the PCS and investigation of FW thermal response with realistic time-dependent heat fluxes. In particular, the comparative assessment has allowed to find the most representative model for simulating the heat transfer phenomena of the specific FWP type in an accurate yet simple way, highlighting that:

- a 1D semi-infinite approximation is not suitable given the heat transfer dynamics involved
- the 1D approximation along fingers' depth is suitable for actively-cooled FWPs, namely for EHF and NHF panels. The 2D approximation, albeit more accurate, has proven not to yield significant benefits. The 1D approximation is conversely not suitable for TFW panels, in which a 2D approximation with a rectangular grid has instead been proposed. It has also been shown that toroidal gaps and bolts play a relevant role in the heat transfer process, therefore it is important to include them in the model
- the assumption of neglecting fingers' toroidal curvature has been justified both for EHF and TFW panels through the benchmarking with higher fidelity simulations. As a more accurate simulation of NHF fingers has not been retrieved, a benchmark with the 2D model developed is suggested for further studies both to prove the assumption of neglecting toroidal curvature for this type of panels and to more precisely evaluate the coefficient f_{2D} accounting for 2D effects
- in the range of temperatures relevant for this work, the dependency of thermal properties with the temperature is negligible, therefore the assumption of constant properties is justified

Furthermore, the sensitivity analysis on the HTC for EHF and NHF panels has shown that the assumption of employing a constant HTC is quite reasonable for EHF panels but less for NHF panels. In both cases, more accurate models, whose development is left for further studies, are needed to assess the coupling between the FWP and the coolant through appropriate correlations, especially to include nucleate boiling and avoid reaching the boiling crisis. Regarding TFW panels, an equivalent HTC has been defined through a 0D approximation. This approach provides a first-guess

HTC which, despite being valid only for high temperatures, is useful to model TFW panels' discharge phase in a simple way, without developing more complex non-linear thermal models capable of handling radiation heat transfer. Once a representative thermal model for each FWP type has been identified, a convergence analysis has been performed for each FWP type in sections 4.1.3, 4.1.4, and 4.1.5 with the objective of finding a reasonable grid size and time step for the models to be compliant with RT requirements. Comparative assessment and convergence analysis together provide a systematic approach, absent in the literature, in order to identify a trade-off between accuracy and computational cost for the design and RT operation of the FWHLC in the AFP phase, thus answering the first research question. The selected models for each type of FWP are:

- EHF/NHF: 1D model with constant properties having $N_x = 108$ nodes along fingers' depth direction and $\Delta t = 1e-2$ s
- TFW: 2D model with a rectangular grid (including toroidal gaps and bolts) and constant properties having $N_x = 108$ nodes along fingers' depth direction, $N_\phi = 34$ nodes along the toroidal direction, and $\Delta t = 0.1$ s

Simulations have been performed in the ITER computing cluster, whose computational load is not deterministic. Therefore, convergence analyses should be repeated in a dedicated RT framework to have more accurate results. Additionally, the computational cost can be improved through model reduction techniques as stated in section 4.1.8. Among the others, the ADI method has been tested in this work, but this method turned out not to be computationally efficient because of the Thomas algorithm implemented in MATLAB. Therefore, further studies concerning the optimization of the solving algorithm are needed. On top of that, the computational cost can be further reduced by lowering the number of nodes in the x direction N_x, which has been chosen, as explained in section 3.1.4, with the objective of not losing information about the thermal gradient. However, as major thermal gradients occur close to the finger's surfaces, one can think of employing a non-uniform grid, finer close to the surface and progressively coarser moving further from it. Furthermore, this work presents the novelty of having employed a BE method for 1D and 2D models (both with constant and variable properties), also demonstrating its advantage over a FE method in terms of computational cost given the sizes of the matrices employed. However, in the case of lower matrices' sizes, which is the case if a non-uniform grid is employed, the FE method could be more advantageous, so the final choice of the method to employ depends on the matrices' sizes. After a trade-off between accuracy and computational cost has been identified, the models developed have been integrated into Simulink to investigate FW thermal response through realistic time-dependent heat loads. For this reason, throughout this work, a strong emphasis has been placed on maintaining a state-space formulation that facilitates the integration in the Simulink-based PCS. Results, presented in section 4.1.7, show that heat transfer's time scales are of the order of seconds, consistently with the models developed in the case of constant artificial heat flux. The definition of the typical dynamics of heat transfer, which answers the second research question, is essential for the controller design.

Concerning the steady-state model for IR cameras' synthetic diagnostic in DT phase, a thermal model applied to EHF and NHF panels, the only ones envisaged to be installed in the DT phase, has been proposed by analytically solving the steady-state 1D heat conduction equation along panels' depth with volumetric heat generation. This approach allows to use thermal flux data from the SMITER code, evaluate the surface temperature map for every FWP, and load temperature data back to SMITER, so that temperature map data can be used as a benchmark with the measurements of the IR cameras during the flat-top phase (as this model is limited to steady-state conditions) in DT operation. This approach is complementary and at the same time structurally simpler than coupling magnetic field line tracing codes (SMITER) with finite-difference, time-evolving software and than employing rather complex 3D FEM simulations for several FWP's fingers, thus answering the third research question. Results show that:

- with the exception of FWPs 4 and 8, FWP's surface temperature is generally lower than 200 °C, which corresponds to IR cameras' threshold for temperature measurement
- volumetric heat generation does not significantly influence the surface temperature. This justifies the assumption of employing a constant volumetric heat flux and the conservative value of the calculated ϕ_W

This model has the limitation of being restricted to the DT phase and to the flat-top phase, for which a simple analytical solution can be employed. Further studies are needed to extend the evaluation of temperature maps to other phases for IR cameras' synthetic diagnostics, reasonably by numerically solving the heat diffusion equation.

In conclusion, this thesis contributes to the progress in nuclear fusion research by providing a control-oriented thermal model useful for developing a controller and designing protection functions for the ITER first wall in real-time. Furthermore, it provides a steady-state model for generating temperature maps in the ITER DT phase useful for IR cameras' synthetic diagnostic.

Appendix A

Material properties

This Appendix reports the correlations of material properties with the temperature employed in this work.

Tungsten (W)			
Symbol	Physical property	Unit	Temperature dependence
k	heat conductivity	[W/m/K]	$k(T) = 174.9274 - 0.1067 \cdot T + 5.0067e-5 \cdot T^2 - 7.8349e-9 \cdot T^3$
cp	specific heat	[J/kg/K]	$cp(T) = 128.308 + 3.2797e-2 \cdot T - 3.4097e-6 \cdot T^2$
ρ	density	[kg/mˆ3]	$\rho(T) = 1000 * (19.3027 - 2.3786e-4 \cdot T - 2.2448e-8 \cdot T^2)$
c^*	"corrected" specific heat	[J/kg/K]	$c^*(T) = 128.308 + 2 \cdot 3.2797e-2 \cdot T - 3 * 3.4097e-6 \cdot T^2$

Table A.1: Thermal properties of W as a function of the temperature. Range of validity: 20 °C to 1000 °C. From [ITER, 2013].

CuCrZr			
Symbol	Physical property	Unit	Temperature dependence
k	heat conductivity	[W/m/K]	$k(T) = 2.11e-7 \cdot T^3 - 2.83e-4 \cdot T^2 - 1.38e-1 \cdot T + 323$
cp	specific heat	[J/kg/K]	$cp(T) = 6.32e-6 \cdot T^2 + 9.49e-2 \cdot T + 3.88e2$
ρ	density	[kg/mˆ3]	$\rho(T) = 8900 \cdot (1 - 3e-6 \cdot (7.20e-9 \cdot T^3 - 9.05e-6 \cdot T^2 + 6.24e-3 \cdot T + 16.6) \cdot (T - 20))$
c^*	"corrected" specific heat	[J/kg/K]	$c^*(T) = 3.88e2 + 2 \cdot 9.49e-2 \cdot T + 3 \cdot 6.32e-6 \cdot T^2$

Table A.2: Thermal properties of CuCrZr as a function of the temperature. Range of validity: 20 °C to 700 °C. From [ITER, 2013].

Stainless steel (SS)			
Symbol	Physical property	Unit	Temperature dependence
k	heat conductivity	[W/m/K]	$k(T) = 1.502e-2 \cdot T + 13.98$
cp	specific heat	[J/kg/K]	$cp(T) = 462.69 + 0.520265 \cdot T - 1.7117 \cdot 1e-3 \cdot T^2 + 3.3658 \cdot 1e-6 \cdot T^3 - 2.1958 \cdot 1e-9 \cdot T^4$
ρ	density	[kg/mˆ3]	$\rho(T) = -6 \cdot 1e-5 \cdot T^2 - 0.3977 \cdot T + 7939.3$
c^*	"corrected" specific heat	[J/kg/K]	$c^*(T) = 462.69 + 2 \cdot 0.520265 \cdot T - 3 \cdot 1.7117 \cdot 1e-3 \cdot T^2 + 4 \cdot 3.3658 \cdot 1e-6 \cdot T^3 - 5 \cdot 2.1958 \cdot 1e-9 \cdot T^4$

Table A.3: Thermal properties of stainless steel 316L(N)-IG as a function of the temperature. Range of validity: 20 °C to 800 °C. From [ITER, 2013].

Appendix B

Derivations of matrix formulations for 1D models

This part is dedicated to the derivations of matrix formulations of the discretized energy balance equation depending on the specific model considered and the numerical scheme employed for 1D models.

B.1 1D Forward Euler with constant properties

The discretized equation $\rho c \frac{T_i^{m+1} - T_i^m}{\Delta t} = k \cdot \frac{T_{i-1}^m - 2T_i^m + T_{i+1}^m}{\Delta x^2}$ is applied to the domain shown in figure 3.6 to the inner nodes:

$$\begin{pmatrix} T_1 \\ T_2 \\ \vdots \\ \\ \\ \\ T_{end} \end{pmatrix}^{m+1} = \begin{pmatrix} BC & BC & 0 & \cdots & \cdots & \cdots & 0 \\ a & 1-2a & a & 0 & \cdots & \cdots & 0 \\ 0 & \ddots & \ddots & \ddots & 0 & \cdots & 0 \\ \vdots & 0 & \ddots & \ddots & \ddots & \vdots & \\ \vdots & & & & & & \\ & & & & & & \\ 0 & \cdots & & & & BC & BC \end{pmatrix} \cdot \begin{pmatrix} T_1 \\ T_2 \\ \vdots \\ \\ \\ \\ T_{end} \end{pmatrix}^m \tag{B.1}$$

where $a = \frac{\alpha \Delta t}{\Delta x^2}$.

The boundary condition (BC in the equation above) on the first node takes into account the incident heat flux:

$$\rho c \frac{\partial T_1}{\partial t} = k \frac{\partial^2 T_1}{\partial x^2} + \frac{q_s dA}{dV} \tag{B.2}$$

where dA and dV are an infinitesimal area and volume respectively, which can be defined as $dA = d\phi \cdot d\theta$ and $dV = d\phi \cdot d\theta \cdot dx$. This equation is discretized as follows:

$$\rho c \frac{T_1^{m+1} - T_1^m}{\Delta t} = k \cdot \frac{T_2^m - T_1^m}{\Delta x^2} + \frac{q_s}{\Delta x}$$

$$\iff T_1^{m+1} = T_1^m + a \cdot T_2^m - a \cdot T_1^m + \frac{q_s \Delta t}{\rho c \Delta x} = (1-a) T_1^m + a \cdot T_2^m + \frac{q_s \Delta t}{\rho c \Delta x} \tag{B.3}$$

The boundary condition on the last node is the adiabatic condition:

$$\rho c \frac{\partial T_{end}}{\partial t} = k \frac{\partial^2 T_{end}}{\partial x^2} \tag{B.4}$$

which is discretized as follows:

$$\rho c \frac{T_{end}^{m+1} - T_{end}^{m}}{\Delta t} = k \cdot \frac{T_{end-1}^{m} - T_{end}^{m}}{\Delta x^2}$$

$$\iff T_{end}^{m+1} = T_{end}^{m} - a \cdot T_{end}^{m} + a \cdot T_{end-1}^{m} = (1-a) T_{end}^{m} + a \cdot T_{end-1}^{m} \tag{B.5}$$

Therefore, equation B.1 can be written in state-space formulation:

$$\underbrace{\begin{pmatrix} T_1 \\ T_2 \\ \vdots \\ \\ \\ \\ T_{end} \end{pmatrix}^{m+1}}_{\underline{T}^{m+1}} = \underbrace{\begin{pmatrix} 1-a & a & 0 & \cdots & \cdots & \cdots & 0 \\ a & 1-2a & a & 0 & \cdots & \cdots & 0 \\ 0 & \ddots & \ddots & \ddots & 0 & \cdots & 0 \\ \vdots & 0 & \ddots & \ddots & \ddots & \vdots & \\ \vdots & & & & & & \\ & & & & & & \\ 0 & \cdots & & & & a & 1-a \end{pmatrix}}_{\underline{\underline{A}}} \cdot \underbrace{\begin{pmatrix} T_1 \\ T_2 \\ \vdots \\ \\ \\ T_{end-1} \\ T_{end} \end{pmatrix}^{m}}_{\underline{T}^{m}} + \underbrace{\begin{pmatrix} \frac{\Delta t}{\rho c \Delta x} \\ 0 \\ \vdots \\ \\ \\ \\ 0 \end{pmatrix}}_{\underline{\underline{B}}} \cdot q_s$$

$$\underline{u}^m = [q_s]_{1X1} \qquad \underline{\underline{C}} = [1, 0, ..., 0]_{1Xn} \qquad \underline{\underline{D}} = [0]_{1X1} \tag{B.6}$$

B.2 1D Backward Euler with constant properties

The discretized equation $\rho c \frac{T_i^{m+1} - T_i^m}{\Delta t} = k \cdot \frac{T_{i-1}^{m+1} - 2T_i^{m+1} + T_{i+1}^{m+1}}{\Delta x^2}$ is applied to the domain shown in figure 3.7 to the inner nodes:

$$\begin{pmatrix} BC & BC & 0 & \cdots & \cdots & \cdots & & 0 \\ -a_W & 1+2a_W & -a_W & 0 & \cdots & \cdots & & 0 \\ 0 & \ddots & \ddots & \ddots & 0 & \cdots & & 0 \\ \vdots & 0 & BC & BC & BC & 0 & \cdots & 0 \\ \vdots & 0 & \cdots & -a & 1+2a & -a & & \\ 0 & \cdots & & & \ddots & \ddots & \ddots & \\ 0 & \cdots & & & & 0 & BC & BC \end{pmatrix} \cdot \begin{pmatrix} T_1 \\ T_2 \\ \vdots \\ T_{int} \\ \\ \\ T_{end} \end{pmatrix}^{m+1} = \begin{pmatrix} T_1 \\ T_2 \\ \vdots \\ T_{int} \\ \\ \\ T_{end} \end{pmatrix}^{m} \tag{B.7}$$

where $a_W = \frac{\alpha_w \Delta t}{\Delta x^2}$ for tungsten and $a = \frac{\alpha \Delta t}{\Delta x^2}$ for CuCrZr/SS. The boundary condition on the first node is a Neumann boundary condition:

$$-k_W \cdot \left.\frac{\partial T}{\partial x}\right|_{x=0} = q_s \tag{B.8}$$

which is discretized as follows:

$$-k_W \cdot \frac{T_2^{m+1} - T_1^{m+1}}{\Delta x} = q_s \iff T_1^{m+1} - T_2^{m+1} = \frac{q_s^{m+1} \cdot \Delta x}{k_W} \tag{B.9}$$

The boundary condition on the last node is a Robin boundary condition:

$$-k \cdot \left.\frac{\partial T}{\partial x}\right|_{x=L_{tot}} = h(T(x = L_{tot}) - T_{water}) \iff T_{end}^{m+1} \cdot \left(1 + \frac{h\Delta x}{k}\right) - T_{end-1}^{m+1} = \frac{h \Delta x T_{water}}{k} \tag{B.10}$$

The interface between the materials requires a boundary condition as well, namely a heat flux equivalence:

$$-k_W \frac{\partial T}{\partial x}\bigg|_{x=int} = -k \frac{\partial T}{\partial x}\bigg|_{x=int} \tag{B.11}$$

Its discretization is:

$$-\frac{k_W}{k} T_{int-1}^{m+1} + \left(1 + \frac{k_W}{k}\right) T_{int}^{m+1} - T_{int+1}^{m+1} = 0 \tag{B.12}$$

Equation B.7 therefore becomes:

$$\begin{pmatrix} T_1 \\ T_2 \\ \vdots \\ T_{int} \\ \\ \\ T_{end} \end{pmatrix}^{m+1} = \begin{pmatrix} 1 & -1 & 0 & \cdots & \cdots & \cdots & & 0 \\ -a_W & 1+2a_W & -a_W & 0 & \cdots & \cdots & & 0 \\ 0 & \ddots & \ddots & \ddots & 0 & \cdots & & 0 \\ \vdots & 0 & -\frac{k_W}{k} & 1+\frac{k_W}{k} & -1 & 0 & \cdots & 0 \\ \vdots & 0 & \cdots & -a & 1+2a & -a & & \\ 0 & \cdots & & & \ddots & \ddots & \ddots & \\ 0 & \cdots & & & & 0 & -1 & 1+\frac{h\Delta x}{k} \end{pmatrix}^{-1} \cdot \begin{pmatrix} \frac{q_s^{m+1}\cdot\Delta x}{k_W} \\ T_2^m \\ \vdots \\ 0 \\ \\ \\ T_{end-1}^m \\ \frac{h\Delta x T_{water}}{k} \end{pmatrix} \tag{B.13}$$

The above expression can be written in the state-space formulation. In order to do that, the above expression is arranged as:

$$\begin{pmatrix} 1 & 1 & 0 & \cdots & \cdots & \cdots & & 0 \\ -a_W & 1+2a_W & -a_W & 0 & \cdots & \cdots & & 0 \\ 0 & \ddots & \ddots & \ddots & 0 & \cdots & & 0 \\ \vdots & 0 & -\frac{k_W}{k} & 1+\frac{k_W}{k} & -1 & 0 & \cdots & 0 \\ \vdots & 0 & \cdots & -a & 1+2a & -a & & \\ 0 & \cdots & & & \ddots & \ddots & \ddots & \\ 0 & \cdots & & & & 0 & -1 & \frac{h\Delta x}{k} \end{pmatrix} \cdot \begin{pmatrix} T_1^{m+1} \\ T_2^{m+1} \\ \vdots \\ T_{int}^{m+1} \\ \\ \\ T_{end} \end{pmatrix} = \underbrace{\begin{pmatrix} T_1^m \\ T_2^m \\ \vdots \\ T_{int}^m \\ \\ \\ T_{end}^m \end{pmatrix} + \begin{pmatrix} -T_1^m \\ 0 \\ \vdots \\ -T_{int}^m \\ 0 \\ \vdots \\ -T_{end}^m \end{pmatrix}}_{*} + \begin{pmatrix} \frac{\Delta x}{k_W} & 0 \\ 0 & 0 \\ \vdots & \vdots \\ \vdots & \vdots \\ \vdots & \vdots \\ \vdots & \vdots \\ 0 & \frac{h\Delta x}{k} \end{pmatrix} \cdot \begin{pmatrix} q_s^{m+1} \\ T_{water} \end{pmatrix} \tag{B.14}$$

The term * is equivalent to setting to zero elements at those positions corresponding to boundary conditions nodes:

$$\begin{pmatrix} 0 & 0 & 0 & \dots & & 0 \\ 0 & 1 & 0 & \dots & & 0 \\ \vdots & \ddots & \ddots & \ddots & \dots & 0 \\ 0 & 0 & 0 & \dots & & 0 \\ 0 & \dots & \dots & 1 & 0 & 0 \\ \vdots & \dots & & & \ddots & 0 \\ 0 & 0 & 0 & \dots & & 0 \end{pmatrix} \cdot \begin{pmatrix} T_1 \\ T_2 \\ \vdots \\ T_{int} \\ \\ \\ T_{end} \end{pmatrix}^m$$

By defining:

$$\underline{\underline{A}} = \begin{pmatrix} 1 & -1 & 0 & \cdots & \cdots & \cdots & & 0 \\ -a_W & 1+2a_W & -a_W & 0 & \cdots & \cdots & & 0 \\ 0 & \ddots & \ddots & \ddots & 0 & \cdots & & 0 \\ \vdots & 0 & -\frac{k_W}{k} & 1+\frac{k_W}{k} & -1 & 0 & \cdots & 0 \\ \vdots & 0 & \cdots & -a & 1+2a & -a & & \\ 0 & \cdots & & & \ddots & \ddots & \ddots & \\ 0 & \cdots & & & & 0 & -1 & 1+\frac{h\Delta x}{k} \end{pmatrix}^{-1} \cdot \begin{pmatrix} 0 & 0 & 0 & \ldots & & 0 \\ 0 & 1 & 0 & \ldots & & 0 \\ \vdots & \ddots & \ddots & \ddots & \ldots & 0 \\ & & & & & \\ 0 & 0 & 0 & \ldots & & 0 \\ 0 & \ldots & \ldots & 1 & 0 & 0 \\ \vdots & \ldots & & & \ddots & 0 \\ 0 & 0 & 0 & \ldots & & 0 \end{pmatrix}$$

$$\underline{\underline{B}} = \begin{pmatrix} 1 & -1 & 0 & \cdots & \cdots & \cdots & & 0 \\ -a_W & 1+2a_W & -a_W & 0 & \cdots & \cdots & & 0 \\ 0 & \ddots & \ddots & \ddots & 0 & \cdots & & 0 \\ \vdots & 0 & -\frac{k_W}{k} & 1+\frac{k_W}{k} & -1 & 0 & \cdots & 0 \\ \vdots & 0 & \cdots & -a & 1+2a & -a & & \\ 0 & \cdots & & & \ddots & \ddots & \ddots & \\ 0 & \cdots & & & & 0 & -1 & 1+\frac{h\Delta x}{k} \end{pmatrix}^{-1} \cdot \begin{pmatrix} \frac{\Delta x}{k_W} & 0 \\ 0 & 0 \\ \vdots & \vdots \\ \vdots & \vdots \\ \vdots & \vdots \\ \vdots & \vdots \\ 0 & \frac{h\Delta x}{k} \end{pmatrix}$$

then expression B.14 can be finally written in state space formulation:

$$\underline{T}^{m+1} = \underline{\underline{A}} \cdot \underline{T}^m + \underline{B} \cdot \underbrace{\begin{pmatrix} q_s^{m+1} \\ T_{water} \end{pmatrix}}_{u^{m+1}} \tag{B.15}$$

For completeness, $\underline{\underline{C}} = [1, 0, ..., 0]_{1Xn}$, $\underline{\underline{D}} = [0, 0]_{1X2}$.

B.3 1D Backward Euler with variable properties

Frozen coefficients method

The term $\frac{\partial k(T)}{\partial T} \cdot \left(\frac{\partial T}{\partial x}\right)^2$ equation 2.14 is discretized as follows:

$$\frac{k_{i+1} - k_{i-1}}{T_{i+1} - T_{i-1}} \cdot \left(\frac{T_{i+1} - T_{i-1}}{2\Delta x}\right)^2 = \frac{(k_{i+1} - k_{i-1}) \cdot (T_{i+1} - T_{i-1})}{4\Delta x^2} \tag{B.16}$$

Therefore the entire energy equation is discretized as follows:

$$\rho(T^m) \cdot c^*(T^m) \cdot \frac{T^{m+1} - T^m}{\Delta t} = \left(\frac{k_i}{\Delta x^2} - \frac{k_{i+1} - k_{i-1}}{4\Delta x^2}\right) \cdot T_{i-1}^{m+1} - 2\frac{k_i}{\Delta x^2} T_i^{m+1} + \left(\frac{k_i}{\Delta x^2} + \frac{k_{i+1} - k_{i-1}}{4\Delta x^2}\right) \cdot T_{i+1}^{m+1} \tag{B.17}$$

where $k_i = k(T_i^m)$, $k_{i+1} = k(T_{i+1}^m)$, and $k_{i-1} = k(T_{i-1}^m)$. This expression can be written more compactly by defining the following quantities:

$$k_- = \left(\frac{k_i}{\Delta x^2} - \frac{k_{i+1} - k_{i-1}}{4\Delta x^2}\right)$$
$$k_+ = \left(\frac{k_i}{\Delta x^2} + \frac{k_{i+1} - k_{i-1}}{4\Delta x^2}\right)$$
$$k_{ave} = \frac{k_- + k_+}{2} = \frac{k_i}{\Delta x^2}$$

$$aa_- = \frac{k_-}{\rho(T_i^m)c^*(T_i^m)} \cdot \Delta t$$
$$aa_+ = \frac{k_+}{\rho(T_i^m)c^*(T_i^m)} \cdot \Delta t$$
$$aa_{ave} = \frac{k_{ave}}{\rho(T_i^m)c^*(T_i^m)} \cdot \Delta t \tag{B.18}$$

Therefore, similarly to the previous section, the discretized equation is applied to the domain shown in figure 3.7 and the same boundary conditions are applied obtaining:

$$\begin{pmatrix} T_1 \\ T_2 \\ \vdots \\ T_{int} \\ \\ \\ T_{end} \end{pmatrix}^{m+1} = \begin{pmatrix} 1 & -1 & 0 & \cdots & \cdots & \cdots & & 0 \\ -a_{-,W} & 1+2a_{ave,W} & -a_{+,W} & 0 & \cdots & \cdots & & 0 \\ 0 & \ddots & \ddots & \ddots & 0 & \cdots & & 0 \\ \vdots & 0 & -\frac{k_W(T_{int}^m)}{k(T_{int}^m)} & 1+\frac{k_W(T_{int}^m)}{k(T_{int}^m)} & -1 & 0 & \cdots & 0 \\ \vdots & 0 & \cdots & -a_- & 1+2a_{ave} & -a_+ & & \\ 0 & \cdots & & & \ddots & \ddots & \ddots & \\ 0 & \cdots & & & & 0 & -1 & 1+\frac{h\Delta x}{k(T_{end}^m)} \end{pmatrix}^{-1} \cdot \begin{pmatrix} \frac{q_s \cdot \Delta x}{k_W(T_1^m)} \\ T_2^m \\ \vdots \\ 0 \\ \\ \\ T_{end-1}^m \\ \frac{h\Delta x T_{water}}{k(T_{end}^m)} \end{pmatrix} \tag{B.19}$$

Similarly to the previous section, the above expression can be written in state-space formulation by defining the matrices in the following way:

$$\underline{\underline{A}}^m = \begin{pmatrix} 1 & -1 & 0 & \cdots & \cdots & \cdots & & 0 \\ -a_{-,W} & 1+2a_{ave,W} & -a_{+,W} & 0 & \cdots & \cdots & & 0 \\ 0 & \ddots & \ddots & \ddots & 0 & \cdots & & 0 \\ \vdots & 0 & -\frac{k_W(T_{int}^m)}{k(T_{int}^m)} & 1+\frac{k_W(T_{int}^m)}{k(T_{int}^m)} & -1 & 0 & \cdots & 0 \\ \vdots & 0 & \cdots & -a_- & 1+2a_{ave} & -a_+ & & \\ 0 & \cdots & & & \ddots & \ddots & \ddots & \\ 0 & \cdots & & & & 0 & -1 & 1+\frac{h\Delta x}{k(T_{end}^m)} \end{pmatrix}^{-1} \cdot \begin{pmatrix} 0 & 0 & 0 & \ldots & & 0 \\ 0 & 1 & 0 & \ldots & & 0 \\ \vdots & \ddots & \ddots & \ddots & \ldots & 0 \\ 0 & 0 & 0 & \ldots & & 0 \\ 0 & \ldots & \ldots & 1 & 0 & 0 \\ \vdots & \ldots & & & \ddots & 0 \\ 0 & 0 & 0 & \ldots & & 0 \end{pmatrix}$$

$$\underline{\underline{B}}^m = \begin{pmatrix} 1 & -1 & 0 & \cdots & \cdots & \cdots & & 0 \\ -a_{-,W} & 1+2a_{ave,W} & -a_{+,W} & 0 & \cdots & \cdots & & 0 \\ 0 & \ddots & \ddots & \ddots & 0 & \cdots & & 0 \\ \vdots & 0 & -\frac{k_W(T_{int}^m)}{k(T_{int}^m)} & 1+\frac{k_W(T_{int}^m)}{k(T_{int}^m)} & -1 & 0 & \cdots & 0 \\ \vdots & 0 & \cdots & -a_- & 1+2a_{ave} & -a_+ & & \\ 0 & \cdots & & & \ddots & \ddots & \ddots & \\ 0 & \cdots & & & & 0 & -1 & 1+\frac{h\Delta x}{k(T_{end}^m)} \end{pmatrix}^{-1} \cdot \begin{pmatrix} \frac{\Delta x}{k_W(T_1^m)} & 0 \\ 0 & 0 \\ \vdots & \vdots \\ \vdots & \vdots \\ \vdots & \vdots \\ \vdots & \vdots \\ 0 & \frac{h\Delta x}{k(T_{end}^m)} \end{pmatrix}$$

For completeness, $\underline{\underline{C}} = [1, 0, ..., 0]_{1Xn}$, $\underline{\underline{D}} = [0, 0]_{1X2}$. The difference with respect to the BE method with constant properties is that matrices $\underline{\underline{A}}$ and $\underline{\underline{B}}$ need to be computed at each time step.

Newton's method

Equation 2.14 is discretized in time only and written as:

$$T^{m+1} = T^m + \frac{\Delta t}{\rho(T^{m+1})c^*(T^{m+1})} \cdot \left[k\frac{\partial^2 T}{\partial x^2} + \frac{\partial k}{\partial T} \cdot \left(\frac{\partial T}{\partial x}\right)^2 \right] \tag{B.20}$$

For a given time step $m+1$, the following quantities are renamed: $T^{m+1} = T_{new}$ and $T^m = T_{old}$. At each time step, a system of N non-linear equations is solved, where N is the number of nodes. In particular, Newton's method consists of performing a certain number of iterations until a set tolerance is reached. At each iteration k, the following equation is solved:

$$T_{new}^{k+1} = T_{new}^k - \underline{\underline{J}}(T_{new}^k)^{-1} \cdot \underline{f}(T_{new}^k) \tag{B.21}$$

where $\underline{f}(T_{new}^k)$ is a vector containing the non-linear equations to solve (and the boundary conditions), and $J(T_{new}^k)$ is the Jacobian matrix.

$\underline{f}(T_{new}^k)$ is defined as follows:

$$\underline{f}(T_{new}^k) = \begin{cases} f_1(T_{new,1}, T_{new,2}, ..., T_{new,N}) = 0 \\ \vdots \\ f_N(T_{new,1}, T_{new,2}, ..., T_{new,N}) = 0 \end{cases}$$

$$f_1 : T_{new,1} - T_{new,2} - \frac{q_s \cdot \Delta x}{k(T_{new,1})} = 0$$

$$f_i : T_{new,i} - T_{old,i} - \frac{\Delta t}{\rho(T_{new,i})c^*(T_{new,i})} \cdot \left[k(T_{new,i}) \cdot \frac{T_{new,i-1} - 2T_{new,i} + T_{new,i+1}}{\Delta x^2} + \left(\frac{\partial k}{\partial T}\right)_{T_{new,i}} \cdot \frac{(T_{new,i+1} - T_{new,i-1})^2}{4\Delta x^2} \right] = 0 \quad with\ i = 2, ..., int-1, int+1, ..., end-1$$

$$f_{int} : -T_{new,int-1} + T_{new,int} \cdot \left(1 + \frac{k(T_{new,int})}{k_W(T_{new,int})}\right) - \frac{k(T_{new,int})}{k_W(T_{new,int})} \cdot T_{new,int+1} = 0$$

$$f_{end} : T_{new,end} \cdot \left(1 + \frac{k(T_{new,end})}{h\Delta x}\right) - \frac{k(T_{new,end})T_{new,end-1}}{h\Delta x} - T_{water} = 0 \tag{B.22}$$

The Jacobian matrix is defined as:

$$J_f(1,1) = \frac{\partial f_1}{\partial T_1} = 1 + \frac{q\Delta x}{k^2(T_1)} \cdot \left.\frac{dk}{dT}\right|_{T_1}$$

$$J_f(1,2) = \frac{\partial f_1}{\partial T_2} = -1$$

$$J_f(i,i-1) = \frac{\partial f_i}{\partial T_{i-1}} = -\frac{\beta(T_i) \cdot \Delta t}{\Delta x^2} + \frac{\Delta t}{4\Delta x^2} \cdot \frac{1}{\rho(T_i) \cdot c^*(T_i)} \cdot 2 \cdot (T_{i+1} - T_{i-1}) \cdot \left.\frac{\partial k}{\partial T}\right|_{T_i}$$

$$J_f(i,i) = \frac{\partial f_i}{\partial T_i} = 1 - \left.\frac{d\beta}{dT}\right|_{T_i} \cdot \frac{\Delta t}{\Delta x^2} \cdot T_{i-1} + \left.\frac{d\beta}{dT}\right|_{T_i} \cdot \frac{2\Delta t}{\Delta x^2} \cdot T_i + \frac{2\beta(T_i)\Delta t}{\Delta x^2} - \left.\frac{d\beta}{dT}\right|_{T_i} \cdot \frac{\Delta t}{\Delta x^2} \cdot T_{i+1} -$$
$$\frac{\Delta t}{4\Delta x^2} \cdot (T_{i+1} - T_{i-1})^2 \cdot \frac{d}{dT}\left[\left.\frac{\partial k}{\partial T}\right|_{T_i} \cdot \frac{1}{\rho(T_i) \cdot c^*(T_i)}\right] \qquad with\ i = 2, ..., int-1, int+1, ..., end-1$$

$$J_f(i,i+1) = \frac{\partial f_i}{\partial T_{i-1}} = -\frac{\beta(T_i) \cdot \Delta t}{\Delta x^2} - \frac{\Delta t}{4\Delta x^2} \cdot \frac{1}{\rho(T_i) \cdot c^*(T_i)} \cdot 2 \cdot (T_{i+1} - T_{i-1}) \cdot \left.\frac{\partial k}{\partial T}\right|_{T_i}$$

$$J_f(int, int-1) = \frac{\partial f_{int}}{\partial T_{int-1}} = -1$$

$$J_f(int, int) = \frac{\partial f_{int}}{\partial T_{int}} = 1 + \frac{k(T_{int})}{k_W(T_{int})} + (T_{int} - T_{int+1}) \cdot \left[\frac{1}{k_W(T_{int})} \cdot \left.\frac{dk}{dT}\right|_{T_{int}} - \frac{k(T_{int})}{(k_W(T_{int}))^2} \cdot \left.\frac{dk_W}{dT}\right|_{T_{int}}\right]$$

$$J_f(int, int+1) = \frac{\partial f_{int}}{\partial T_{int+1}} = -\frac{k(T_{int})}{k_W(T_{int})}$$

where $\beta(T_i) = \frac{k(T_i)}{\rho(T_i) \cdot c^*(T_i)}$.

Appendix C

Derivations of matrix formulations for 2D models

This Appendix contains the derivations of matrix formulations in state-space for 2D models and the definition of the boundary conditions.

C.1 2D Backward Euler with constant properties

As discussed in section 3.1.6, the 2D energy equation discretized with a BE method can be written as:

$$\rho c \frac{T_k^{m+1} - T_k^m}{\Delta t} = k \left[\frac{T_{k-1}^{m+1} - 2T_k^{m+1} + T_{k+1}^{m+1}}{\Delta \phi^2} + \frac{T_{k-n_\phi}^{m+1} - 2T_k^{m+1} + T_{k+n_\phi}^{m+1}}{\Delta x^2} \right] \tag{C.1}$$

with $k = 1, ..., n_\phi \cdot n_x$. As already stated, by applying the equation to the inner nodes of the domain in figure 3.8, a pentadiagonal matrix of dimensions $n_\phi \cdot n_x \times n_\phi \cdot n_x$ is obtained, thus leading to the expression:

$$\begin{aligned} \underline{T}^{m+1} &= \underline{T}^m + \frac{\Delta t k}{\rho c} \cdot \underline{\underline{P}} \cdot \underline{T}^{m+1} \\ \iff & \left(\underline{\underline{I}} - \frac{\Delta t k}{\rho c} \cdot \underline{\underline{P}} \right) \cdot \underline{T}^{m+1} = \underline{T}^m \end{aligned} \tag{C.2}$$

where $\underline{\underline{P}}$ is the pentadiagonal matrix, and $\underline{\underline{I}}$ the identity matrix. Basically, the matrix $\underline{\underline{P}}$ contains the discretization of the diffusion process in the inner nodes. The above expression can be written by defining the matrix $\underline{\underline{L}} = \left(\underline{\underline{I}} - \frac{\Delta t k}{\rho c} \cdot \underline{\underline{P}} \right)$:

$$\underline{\underline{L}} \cdot \underline{T}^{m+1} = \underline{T}^m \tag{C.3}$$

The following step is defining the boundary conditions, which are formulated for the matrix $\underline{\underline{L}}$ through the *energy balance method*, which consists of applying the conservation of energy to a control volume that includes the node of interest [Bergman et al., 2011]. The conservation of energy accounts for the energy flows exchanged with the neighboring nodes. Figure C.1 provides a graphical representation.

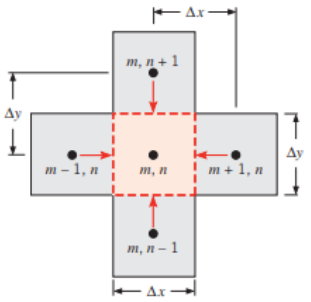

Figure C.1: Conduction to an interior generic node m, n (equivalent to the nomenclature i, j) from its neighboring nodes. For the sake of convenience, it is assumed that the energy flows are directed into the interior node [Bergman et al., 2011].

With a reference to figure 3.8, the *energy balance method* is applied to:

- interface between the materials ($(i = 2, ..., n_\phi - 1;\ j = n_{int})$). Note that the node n_{int} identifies the interface itself
- south border $(i = 2, ..., n_\phi - 1;\ j = 1)$, where there is a convective boundary condition
- north border $(i = 2, ..., n_\phi - 1;\ j = n_x)$, where there is an incoming heat flux
- west border $(i = 1; j = 2, ..., n_{int-1}, n_{int+1}, ..., n_x - 1)$, where there is an adiabatic condition (a consequence of considering the fingers to be thermally isolated)
- east border $(i = n_\phi; j = 2, ..., n_{int-1}, n_{int+1}, ..., n_x - 1)$, where there is an adiabatic condition (a consequence of considering the fingers to be thermally isolated)
- corner north-east $(i = n_\phi; j = n_x)$, having an incoming thermal flux from the north side and adiabatic condition on the east side
- corner north-west $(i = 1; j = n_x)$, having an incoming thermal flux from the north side and adiabatic condition on the west side
- corner south-east $(i = n_\phi; j = 1)$, having convective heat transfer from the south side and adiabatic condition on the east side
- corner south-west $(i = 1; j = 1)$, having convective heat transfer from the south side and adiabatic condition on the west side
- interface between the materials on the west side $(i = 1; j = n_{int})$, having an adiabatic boundary condition on the west side
- interface between the materials on the east side $(i = n_\phi; j = n_{int})$, having an adiabatic boundary condition on the east side

Hereafter, the formulation of the energy balance method for each boundary condition is presented. Note that in the following expressions indexes m, n and i, j are used interchangeably.

C.1.1 Boundary conditions

Interface between the materials

With a reference to figure C.2, the energy balance can be written as follows for a generic node m, n belonging to the interface:

$$k_W \left(\frac{T^{m+1}_{m,n+1} - T^{m+1}_{m,n}}{\Delta x} \right) \cdot \Delta\phi + k_W \left(\frac{T^{m+1}_{m-1,n} - T^{m+1}_{m,n}}{\Delta\phi} \right) \cdot \frac{\Delta x}{2} + k_W \left(\frac{T^{m+1}_{m+1,n} - T^{m+1}_{m,n}}{\Delta\phi} \right) \cdot \frac{\Delta x}{2} +$$
$$k \left(\frac{T^{m+1}_{m,n-1} - T^{m+1}_{m,n}}{\Delta x} \right) \cdot \Delta\phi + k \left(\frac{T^{m+1}_{m-1,n} - T^{m+1}_{m,n}}{\Delta\phi} \right) \cdot \frac{\Delta x}{2} + k \left(\frac{T^{m+1}_{m+1,n} - T^{m+1}_{m,n}}{\Delta\phi} \right) \cdot \frac{\Delta x}{2} = 0$$

$$\iff T^{m+1}_{m,n+1}\cdot\frac{2}{\Delta x^2}+T^{m+1}_{m,n-1}\cdot\frac{2}{\Delta x^2}\cdot\frac{k}{k_W}+T^{m+1}_{m-1,n}\cdot\left(\frac{1}{\Delta x^2}+\frac{1}{\Delta x^2}\cdot\frac{k}{k_W}\right)+T^{m+1}_{m+1,n}\cdot\left(\frac{1}{\Delta x^2}+\frac{1}{\Delta x^2}\cdot\frac{k}{k_W}\right)-$$
$$-T^{m+1}_{m,n}\cdot 2\cdot\left[\left(\frac{1}{\Delta\phi^2}+\frac{1}{\Delta\phi^2}\cdot\frac{k}{k_W}\right)+\left(\frac{1}{\Delta x^2}+\frac{1}{\Delta x^2}\cdot\frac{k}{k_W}\right)\right]=0$$

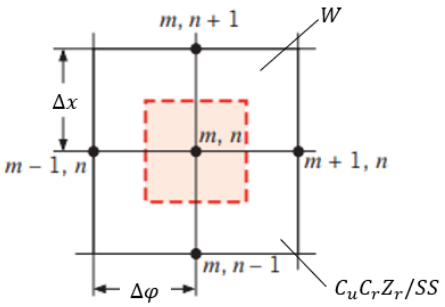

Figure C.2: Schematic representation of the nodes on the interface between the materials. Figure adapted from [Bergman et al., 2011].

Considering equation C.3, the coefficients reported in the above expression can be inserted in the matrix $\underline{\underline{L}}$ for all the nodes m, n (corresponding to the index $k = m + (n-1)\cdot n_x$) belonging to the interface. Furthermore, equation C.3 can be written in the following way to account for the right-hand side value of the above expression:

$$\underline{\underline{L}}\cdot\underbrace{\begin{pmatrix}\vdots\\ T^{m+1}_k\\ \vdots\end{pmatrix}}_{n_\phi\cdot n_x\ \text{X}\ 1}=\underbrace{\begin{pmatrix}\vdots\\ T^{m}_k\\ \vdots\end{pmatrix}}_{n_\phi\cdot n_x\ \text{X}\ 1}+\underbrace{\begin{pmatrix}\vdots\\ -T^{m}_k\\ \vdots\end{pmatrix}}_{n_\phi\cdot n_x\ \text{X}\ 1}+\underbrace{\begin{pmatrix}\vdots & \dots & \\ & & \\ \vdots & & \\ 0 & \dots & \dots\\ \vdots & & \\ & & \\ \vdots & & \end{pmatrix}}_{=\underline{\underline{E}}\ [n_\phi\cdot n_x\ \text{X}\ n_\phi\cdot n_x]}\cdot\underbrace{\underline{q}_s(\phi,t)}_{n_\phi\cdot n_x\ \text{X}\ 1}+\underbrace{\begin{pmatrix}\vdots & \dots & \\ & & \\ \vdots & & \\ 0 & \dots & \dots\\ \vdots & & \\ & & \\ \vdots & & \end{pmatrix}}_{=\underline{\underline{F}}\ [n_\phi\cdot n_x\ \text{X}\ n_\phi\cdot n_x]}\cdot\underbrace{\underline{T}_{water}}_{n_\phi\cdot n_x\ \text{X}\ 1}\qquad\text{(C.4)}$$

where $\underline{q}_s$ is the vector containing the heat flux space distribution changing in time (therefore it is only defined on the north border), $\underline{T}_{water}$ is the vector containing the value T_{water} which is constant in time (therefore it is defined on the south border only), and matrices $\underline{\underline{E}}$ and $\underline{\underline{F}}$ are needed to assign the values of thermal flux and coolant temperature respectively to the correct nodes. These matrices are defined in such a way as to have always zero entries, except for diagonal elements in which there are non-zero coefficients (unless the right-hand side of the energy balance equation for the BC, as in this case, is zero).

South border

With a reference to figure C.3, the energy balance can be written as:

$$\frac{2}{\Delta x^2}\cdot T^{m+1}_{i,2}+\frac{1}{\Delta\phi^2}\cdot T^{m+1}_{i-1,1}+\frac{1}{\Delta\phi^2}\cdot T^{m+1}_{i+1,1}-2\cdot\left(\frac{1}{\Delta x^2}+\frac{1}{\Delta\phi^2}+\frac{h}{k\Delta x}\right)\cdot T^{m+1}_{i,1}=-\frac{2hT_{water}}{k\Delta x}$$

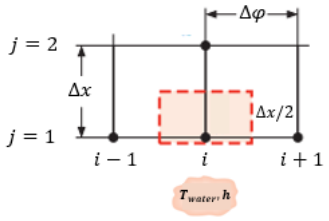

Figure C.3: Schematic representation of the nodes on the south border. Adapted from [Bergman et al., 2011].

Considering equation C.3, the coefficients reported in the above expression can be inserted in the matrix $\underline{\underline{L}}$ for all the nodes m, n (corresponding to the index $k = m + (n-1) \cdot n_x$) belonging to the south border. Furthermore, equation C.3 can be written in the following way to account for the right-hand side value of the above expression:

$$\underline{\underline{L}} \cdot \underbrace{\begin{pmatrix} \vdots \\ T_k^{m+1} \\ \vdots \end{pmatrix}}_{n_\phi \cdot n_x \text{ X } 1} = \underbrace{\begin{pmatrix} \vdots \\ T_k^{m} \\ \vdots \end{pmatrix}}_{n_\phi \cdot n_x \text{ X } 1} + \underbrace{\begin{pmatrix} \vdots \\ -T_k^{m} \\ \vdots \end{pmatrix}}_{n_\phi \cdot n_x \text{ X } 1} + \underbrace{\begin{pmatrix} \vdots & \dots & \\ & & \\ \vdots & & \\ 0 & \dots & \dots \\ \vdots & & \\ & & \\ \vdots & & \end{pmatrix}}_{= \underline{\underline{E}} \ [n_\phi \cdot n_x \text{ X } n_\phi \cdot n_x]} \cdot \underbrace{q_s(\phi, t)}_{n_\phi \cdot n_x \text{ X } 1} + \underbrace{\begin{pmatrix} \vdots & \dots & & & \\ & & & & \\ \vdots & & & & \\ 0 & \dots & -\frac{2h}{k\Delta x} & 0 & \dots \\ \vdots & & & & \\ & & & & \\ \vdots & & & & \end{pmatrix}}_{= \underline{\underline{F}} \ [n_\phi \cdot n_x \text{ X } n_\phi \cdot n_x]} \cdot \underbrace{T_{water}}_{n_\phi \cdot n_x \text{ X } 1} \quad \text{(C.5)}$$

North border

With a reference to figure C.4, the energy balance can be written as:

$$\frac{2}{\Delta x^2} \cdot T_{i,n_x-1}^{m+1} + \frac{1}{\Delta \phi^2} \cdot T_{i-1,n_x}^{m+1} + \frac{1}{\Delta \phi^2} \cdot T_{i+1,n_x}^{m+1} - 2 \cdot \left(\frac{1}{\Delta x^2} + \frac{1}{\Delta \phi^2} \right) \cdot T_{i,n_x}^{m+1} = -\frac{2 q_s(\phi, t)}{k \Delta x}$$

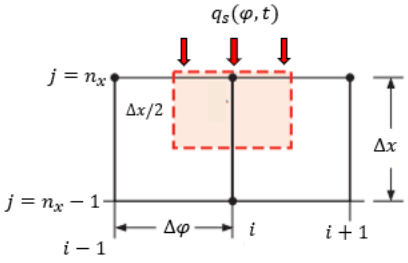

Figure C.4: Schematic representation of the nodes on the north border. Adapted from [Bergman et al., 2011].

Considering equation C.3, the coefficients reported in the above expression can be inserted in the matrix $\underline{\underline{L}}$ for all the nodes m, n (corresponding to the index $k = m + (n-1) \cdot n_x$) belonging to the north border. Furthermore, equation C.3 can be written in the following way to account for the right-hand side value of the above expression:

$$\underline{\underline{L}} \cdot \underbrace{\begin{pmatrix} \vdots \\ T_k^{m+1} \\ \vdots \end{pmatrix}}_{n_\phi \cdot n_x \text{ X } 1} = \underbrace{\begin{pmatrix} \vdots \\ T_k^{m} \\ \vdots \end{pmatrix}}_{n_\phi \cdot n_x \text{ X } 1} + \underbrace{\begin{pmatrix} \vdots \\ -T_k^{m} \\ \vdots \end{pmatrix}}_{n_\phi \cdot n_x \text{ X } 1} + \underbrace{\begin{pmatrix} \vdots & \dots & & & \\ & & & & \\ \vdots & & & & \\ 0 & \dots & -\frac{2}{k\Delta x} & 0 & \dots \\ \vdots & & & & \\ & & & & \\ \vdots & & & & \end{pmatrix}}_{= \underline{\underline{E}} \ [n_\phi \cdot n_x \text{ X } n_\phi \cdot n_x]} \cdot \underbrace{\underline{q_s}(\phi, t)}_{n_\phi \cdot n_x \text{ X } 1} + \underbrace{\begin{pmatrix} \vdots & \dots & \\ & & \\ \vdots & & \\ 0 & \dots & \dots \\ \vdots & & \\ & & \\ \vdots & & \end{pmatrix}}_{= \underline{\underline{F}} \ [n_\phi \cdot n_x \text{ X } n_\phi \cdot n_x]} \cdot \underbrace{\underline{T}_{water}}_{n_\phi \cdot n_x \text{ X } 1} \quad \text{(C.6)}$$

West border

With a reference to figure C.5, the energy balance can be written as:

$$\frac{2}{\Delta\phi^2} \cdot T_{2,j}^{m+1} + \frac{1}{\Delta x^2} \cdot T_{1,j-1}^{m+1} + \frac{1}{\Delta x^2} \cdot T_{1,j+1}^{m+1} - 2 \cdot \left(\frac{1}{\Delta\phi^2} + \frac{1}{\Delta x^2} \right) \cdot T_{1,j}^{m+1} = 0$$

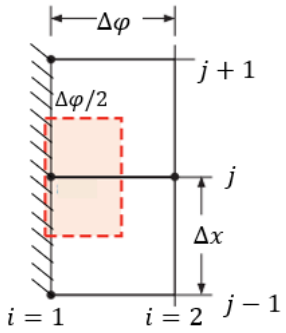

Figure C.5: Schematic representation of the nodes on the west border. Adapted from [Bergman et al., 2011].

Considering equation C.3, the coefficients reported in the above expression can be inserted in the matrix $\underline{\underline{L}}$ for all the nodes m, n (corresponding to the index $k = m + (n-1) \cdot n_x$) belonging to the west border. Furthermore, equation C.3 can be written in the following way to account for the right-hand side value of the above expression:

$$\underline{\underline{L}} \cdot \underbrace{\begin{pmatrix} \vdots \\ T_k^{m+1} \\ \vdots \end{pmatrix}}_{n_\phi \cdot n_x \text{ X } 1} = \underbrace{\begin{pmatrix} \vdots \\ T_k^{m} \\ \vdots \end{pmatrix}}_{n_\phi \cdot n_x \text{ X } 1} + \underbrace{\begin{pmatrix} \vdots \\ -T_k^{m} \\ \vdots \end{pmatrix}}_{n_\phi \cdot n_x \text{ X } 1} + \underbrace{\begin{pmatrix} \vdots & \dots & \\ & & \\ \vdots & & \\ 0 & \dots & \dots \\ \vdots & & \\ & & \\ \vdots & & \end{pmatrix}}_{= \underline{\underline{E}} \ [n_\phi \cdot n_x \text{ X } n_\phi \cdot n_x]} \cdot \underbrace{\underline{q_s}(\phi, t)}_{n_\phi \cdot n_x \text{ X } 1} + \underbrace{\begin{pmatrix} \vdots & \dots & \\ & & \\ \vdots & & \\ 0 & \dots & \dots \\ \vdots & & \\ & & \\ \vdots & & \end{pmatrix}}_{= \underline{\underline{F}} \ [n_\phi \cdot n_x \text{ X } n_\phi \cdot n_x]} \cdot \underbrace{\underline{T}_{water}}_{n_\phi \cdot n_x \text{ X } 1} \quad \text{(C.7)}$$

East border

For the east border, the energy balance equation is very similar to that of the west border:

$$\frac{2}{\Delta\phi^2}\cdot T^{m+1}_{n_{\phi-1},j}+\frac{1}{\Delta x^2}\cdot T^{m+1}_{n_\phi,j-1}+\frac{1}{\Delta x^2}\cdot T^{m+1}_{n_\phi,j+1}-2\cdot\left(\frac{1}{\Delta\phi^2}+\frac{1}{\Delta x^2}\right)\cdot T^{m+1}_{n_\phi,j}=0$$

The matrix expression written for the west border is similar for the east border as well.

Corner north-east

With a reference to figure C.6, the energy balance can be written as:

$$\frac{1}{\Delta\phi^2}\cdot T^{m+1}_{n_\phi-1,n_x}+\frac{1}{\Delta x^2}\cdot T^{m+1}_{n_\phi,n_x-1}-\left(\frac{1}{\Delta\phi^2}+\frac{1}{\Delta x^2}\right)\cdot T^{m+1}_{n_\phi,n_x}=-\frac{q_s(\phi,t)}{\Delta x k_W}$$

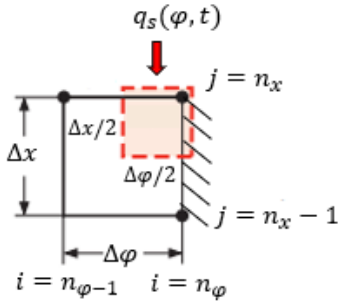

Figure C.6: Schematic representation of the nodes on the north-east corner. Adapted from [Bergman et al., 2011].

Considering equation C.3, the coefficients reported in the above expression can be inserted in the matrix $\underline{\underline{L}}$ for the single node m,n (corresponding to the index $k=m+(n-1)\cdot n_x$) belonging to the north-east corner. Furthermore, equation C.3 can be written in the following way to account for the right-hand side value of the above expression:

$$\underline{\underline{L}}\cdot\underbrace{\begin{pmatrix}\vdots\\ T^{m+1}_k\\ \vdots\end{pmatrix}}_{n_\phi\cdot n_x\ \mathrm{X}\ 1}=\underbrace{\begin{pmatrix}\vdots\\ T^{m}_k\\ \vdots\end{pmatrix}}_{n_\phi\cdot n_x\ \mathrm{X}\ 1}+\underbrace{\begin{pmatrix}\vdots\\ -T^{m}_k\\ \vdots\end{pmatrix}}_{n_\phi\cdot n_x\ \mathrm{X}\ 1}+\underbrace{\begin{pmatrix}\vdots & \cdots & & & & & \\ & & & & & & \\ \vdots & & & & & & \\ 0 & \cdots & -\frac{1}{k_W\Delta x} & 0 & \cdots & & \\ \vdots & & & & & & \\ & & & & & & \\ \vdots & & & & & & \end{pmatrix}}_{=\underline{\underline{E}}\ [n_\phi\cdot n_x\ \mathrm{X}\ n_\phi\cdot n_x]}\cdot\underbrace{\underline{q_s}(\phi,t)}_{n_\phi\cdot n_x\ \mathrm{X}\ 1}+\underbrace{\begin{pmatrix}\vdots & \cdots & & & \\ & & & & \\ \vdots & & & & \\ 0 & \cdots & \cdots & & \\ \vdots & & & & \\ & & & & \\ \vdots & & & & \end{pmatrix}}_{=\underline{\underline{F}}\ [n_\phi\cdot n_x\ \mathrm{X}\ n_\phi\cdot n_x]}\cdot\underbrace{\underline{T_{water}}}_{n_\phi\cdot n_x\ \mathrm{X}\ 1}\tag{C.8}$$

Corner north-west

For the north-west corner, the energy balance equation is very similar to that of the north-east one:

$$\frac{1}{\Delta\phi^2}\cdot T^{m+1}_{2,n_x}+\frac{1}{\Delta x^2}\cdot T^{m+1}_{1,n_x-1}-\left(\frac{1}{\Delta\phi^2}+\frac{1}{\Delta x^2}\right)\cdot T^{m+1}_{1,n_x}=-\frac{q_s(\phi,t)}{\Delta x k_W}$$

The matrix expression written for the northeast border is similar for the northwest border as well.

Corner south-east

With a reference to figure C.7, the energy balance can be written as:

$$\frac{1}{\Delta\phi^2}\cdot T^{m+1}_{n_{\phi-1},1}+\frac{1}{\Delta x^2}\cdot T^{m+1}_{n_\phi,2}-\left(\frac{1}{\Delta\phi^2}+\frac{1}{\Delta x^2}+\frac{h}{k\Delta x}\right)\cdot T^{m+1}_{n_\phi,1}=-\frac{hT_{water}}{\Delta x k}$$

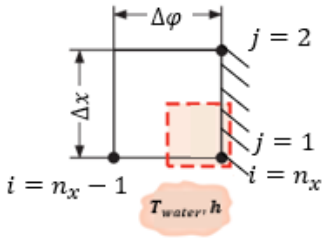

Figure C.7: Schematic representation of the nodes on the southeast corner. Adapted from [Bergman et al., 2011].

Considering equation C.3, the coefficients reported in the above expression can be inserted in the matrix $\underline{\underline{L}}$ for the single node m,n (corresponding to the index $k=m+(n-1)\cdot n_x$) belonging to the south-east corner. Furthermore, equation C.3 can be written in the following way to account for the right-hand side value of the above expression:

$$\underline{\underline{L}}\cdot\underbrace{\begin{pmatrix}\vdots\\ T_k^{m+1}\\ \vdots\end{pmatrix}}_{n_\phi\cdot n_x\ \mathrm{X}\ 1}=\underbrace{\begin{pmatrix}\vdots\\ T_k^{m}\\ \vdots\end{pmatrix}}_{n_\phi\cdot n_x\ \mathrm{X}\ 1}+\underbrace{\begin{pmatrix}\vdots\\ -T_k^{m}\\ \vdots\end{pmatrix}}_{n_\phi\cdot n_x\ \mathrm{X}\ 1}+\underbrace{\begin{pmatrix}\vdots & \dots & \\ & & \\ \vdots & & \\ 0 & \dots & \dots\\ \vdots & & \\ & & \\ \vdots & & \end{pmatrix}}_{=\underline{\underline{E}}\ [n_\phi\cdot n_x\ \mathrm{X}\ n_\phi\cdot n_x]}\cdot\underbrace{\underline{q_s}(\phi,t)}_{n_\phi\cdot n_x\ \mathrm{X}\ 1}+\underbrace{\begin{pmatrix}\vdots & \dots & & & & \\ & & & & & \\ \vdots & & & & & \\ 0 & \dots & -\frac{h}{k\Delta x} & 0 & \dots & \\ \vdots & & & & & \\ & & & & & \\ \vdots & & & & & \end{pmatrix}}_{=\underline{\underline{F}}\ [n_\phi\cdot n_x\ \mathrm{X}\ n_\phi\cdot n_x]}\cdot\underbrace{\underline{T}_{water}}_{n_\phi\cdot n_x\ \mathrm{X}\ 1}\quad(\mathrm{C.9})$$

Corner south-west

For the south-west corner, the energy balance equation is very similar to that of the south-east one:

$$\frac{1}{\Delta\phi^2}\cdot T^{m+1}_{1,2}+\frac{1}{\Delta x^2}\cdot T^{m+1}_{2,1}-\left(\frac{1}{\Delta\phi^2}+\frac{1}{\Delta x^2}+\frac{h}{k\Delta x}\right)\cdot T^{m+1}_{1,1}=-\frac{hT_{water}}{\Delta x k}$$

The matrix expression written for the southwest border is similar for the southeast border as well.

Interface between the materials on the west side

With a reference to figure C.8, the energy balance can be written as:

$$\frac{1}{\Delta x^2}\cdot T^{m+1}_{1,n_{int}+n_\phi}+\frac{k}{k_W}\cdot\frac{1}{\Delta x^2}\cdot T^{m+1}_{1,n_{int}-n_\phi}+\frac{1}{\Delta\phi^2}\cdot\left(1+\frac{k}{k_W}\right)\cdot T^{m+1}_{2,n_{int}}-$$
$$-T^{m+1}_{1,n_{int}}\cdot\left[\frac{1}{\Delta\phi^2}\cdot\left(1+\frac{k}{k_W}\right)+\frac{1}{\Delta x^2}\cdot\left(1+\frac{k}{k_W}\right)\right]=0$$

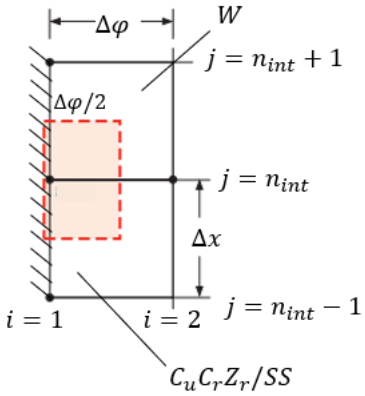

Figure C.8: Schematic representation of the nodes on the interface between the materials on the west side. Adapted from [Bergman et al., 2011].

The matrix expression written for the nodes belonging to the interface between the materials on the west side is similar to the one written for the interface.

Interface between the materials on the east side

For the interface between the materials on the east side, the energy balance equation is very similar to that of the west side:

$$\frac{1}{\Delta x^2}\cdot T^{m+1}_{n_\phi,n_{int}+n_\phi}+\frac{k}{k_W}\cdot\frac{1}{\Delta x^2}\cdot T^{m+1}_{n_\phi,n_{int}-n_\phi}+\frac{1}{\Delta\phi^2}\cdot\left(1+\frac{k}{k_W}\right)\cdot T^{m+1}_{n_\phi-1,n_{int}}- \\ -T^{m+1}_{n_\phi,n_{int}}\cdot\left[\frac{1}{\Delta\phi^2}\cdot\left(1+\frac{k}{k_W}\right)+\frac{1}{\Delta x^2}\cdot\left(1+\frac{k}{k_W}\right)\right]=0$$

The matrix expression written for the nodes belonging to the interface between the materials on the east side is similar to the one written for the interface.

C.1.2 State-space representation

After having defined the boundary conditions, thus after having filled the matrices $\underline{\underline{L}}, \underline{\underline{E}}$, and $\underline{\underline{F}}$, starting from the following equation:

$$\underline{\underline{L}}\cdot\underbrace{\begin{pmatrix}\vdots\\ T_k^{m+1}\\ \vdots\end{pmatrix}}_{n_\phi\cdot n_x\ \mathrm{X}\ 1}=\underbrace{\begin{pmatrix}\vdots\\ T_k^{m}\\ \vdots\end{pmatrix}}_{n_\phi\cdot n_x\ \mathrm{X}\ 1}+\underbrace{\begin{pmatrix}\vdots\\ -T_k^{m}\\ \vdots\end{pmatrix}}_{n_\phi\cdot n_x\ \mathrm{X}\ 1}+\underbrace{\underline{\underline{E}}}_{n_\phi\cdot n_x\ \mathrm{X}\ n_\phi\cdot n_x}\cdot\underbrace{\underline{q_s}(\phi,t)}_{n_\phi\cdot n_x\ \mathrm{X}\ 1}+\underbrace{\underline{\underline{F}}}_{n_\phi\cdot n_x\ \mathrm{X}\ n_\phi\cdot n_x}\cdot\underbrace{\underline{T_{water}}}_{n_\phi\cdot n_x\ \mathrm{X}\ 1} \tag{C.10}$$

this can be written as:

$$\underline{\underline{L}} \cdot \underbrace{\begin{pmatrix} \vdots \\ T_k^{m+1} \\ \vdots \end{pmatrix}}_{n_\phi \cdot n_x \text{ X } 1} = \underline{\underline{I^*}} \cdot \underbrace{\begin{pmatrix} \vdots \\ T_k^{m} \\ \vdots \end{pmatrix}}_{n_\phi \cdot n_x \text{ X } 1} + \underbrace{[\underline{\underline{E}}|\underline{\underline{F}}]}_{n_\phi \cdot n_x \text{ X } 2n_\phi \cdot n_x} \cdot \underbrace{\begin{pmatrix} \\ \underline{q}_s(\phi,t) \\ \\ \underline{T}_{water} \\ \\ \end{pmatrix}}_{2n_\phi \cdot n_x \text{ X } 1} \tag{C.11}$$

where $\underline{\underline{I^*}}$ is a matrix having zero entries everywhere except for diagonal elements whose index corresponds to an inner node in the domain. The state-space representation is then:

$$\underbrace{\begin{pmatrix} \vdots \\ T_k^{m+1} \\ \vdots \end{pmatrix}}_{n_\phi \cdot n_x \text{ X } 1} = \underbrace{\underline{\underline{A}}}_{n_\phi \cdot n_x \text{ X } n_\phi \cdot n_x} \cdot \underbrace{\begin{pmatrix} \vdots \\ T_k^{m} \\ \vdots \end{pmatrix}}_{n_\phi \cdot n_x \text{ X } 1} + \underbrace{\underline{\underline{B}}}_{n_\phi \cdot n_x \text{ X } 2n_\phi \cdot n_x} \cdot \underbrace{\begin{pmatrix} \\ \underline{q}_s(\phi,t) \\ \\ \underline{T}_{water} \\ \\ \end{pmatrix}}_{\underline{u}\ [2n_\phi \cdot n_x \text{ X } 1]} \tag{C.12}$$

where $\underline{\underline{A}} = \underline{\underline{L}}^{-1} \cdot \underline{\underline{I^*}}$ and $\underline{\underline{B}} = \underline{\underline{L^{-1}}} \cdot [\underline{\underline{E}}|\underline{\underline{F}}]$.

C.2 2D Backward Euler with variable properties (FC method)

The energy balance 2.17 equation can be discretized as follows with the FC method with the hypothesis of the absence of volumetric heat generation:

$$\begin{aligned} \rho(T^m)c^*(T^m)\frac{\partial T}{\partial t} = k(T^m) \cdot \left[\frac{T_{i-1,j}^{m+1} - 2T_{i,j}^{m+1} + T_{i+1,j}^{m+1}}{\Delta x^2} + \frac{T_{i,j-1}^{m+1} - 2T_{i,j}^{m+1} + T_{i,j+1}^{m+1}}{\Delta y^2} \right] + \\ + \frac{k_{i+1,j} - k_{i-1,j}}{T_{i+1,j} - T_{i-1,j}} \cdot \left(\frac{T_{i+1,j}^{m+1} - T_{i-1,j}^{m+1}}{2\Delta x} \right)^2 + \frac{k_{i,j+1} - k_{i,j-1}}{T_{i,j+1} - T_{i,j-1}} \cdot \left(\frac{T_{i,j+1}^{m+1} - T_{i,j-1}^{m+1}}{2\Delta y} \right)^2 \end{aligned} \tag{C.13}$$

where $k_{i\pm1,j} = k(T_{i\pm1,j}^m)$ and $k_{i,j\pm1} = k(T_{i,j\pm1}^m)$. The above expression can be written as:

$$\begin{aligned} \rho(T^m)c^*(T^m)\frac{\partial T}{\partial t} = k(T^m) \cdot \left[\frac{T_{i-1,j}^{m+1} - 2T_{i,j}^{m+1} + T_{i+1,j}^{m+1}}{\Delta x^2} + \frac{T_{i,j-1}^{m+1} - 2T_{i,j}^{m+1} + T_{i,j+1}^{m+1}}{\Delta y^2} \right] + \\ \frac{(k_{i+1,j} - k_{i-1,j}) \cdot (T_{i+1,j}^{m+1} - T_{i-1,j}^{m+1})}{4\Delta x^2} + \frac{(k_{i,j+1} - k_{i,j-1}) \cdot (T_{i,j+1}^{m+1} - T_{i,j-1}^{m+1})}{4\Delta y^2} \end{aligned} \tag{C.14}$$

Subsequently, the following quantities can be defined:

$$
\begin{aligned}
k_{west} &= \left(\frac{k_{i,j}}{\Delta x^2} - \frac{k_{i+1,j} - k_{i-1,j}}{4\Delta x^2} \right) \\
k_{east} &= \left(\frac{k_{i,j}}{\Delta x^2} + \frac{k_{i+1,j} - k_{i-1,j}}{4\Delta x^2} \right) \\
k_{south} &= \left(\frac{k_{i,j}}{\Delta y^2} - \frac{k_{i,j+1} - k_{i,j-1}}{4\Delta y^2} \right) \\
k_{north} &= \left(\frac{k_{i,j}}{\Delta y^2} + \frac{k_{i,j+1} - k_{i,j-1}}{4\Delta y^2} \right) \\
k_{ave} &= \frac{k_{west} + k_{east} + k_{south} + k_{north}}{2} = \\
&= k_{i,j} \cdot \left(\frac{1}{\Delta x^2} + \frac{1}{\Delta y^2} \right)
\end{aligned} \tag{C.15}
$$

Equation C.14 can be expressed as:

$$
\rho(T^m) c^*(T^m) \frac{T_{i,j}^{m+1} - T_{i,j}^m}{\Delta t} = k_{west} \cdot T_{i-1,j}^{m+1} + k_{east} \cdot T_{i+1,j}^{m+1} + k_{south} \cdot T_{i,j-1}^{m+1} + k_{north} \cdot T_{i,j+1}^{m+1} - 2k_{ave} T_{i,j}^{m+1} \tag{C.16}
$$

If the right-hand side of the above equation is written as $\underline{\underline{P}} \cdot \underline{T}^{m+1}$, then:

$$
\begin{aligned}
\underline{T}^{m+1} &= \underline{T}^m + \frac{\Delta t}{\rho(T^m) c(T^m)} \cdot \underline{\underline{P}}(T^m) \cdot \underline{T}^{m+1} \\
\iff & \left(\underline{\underline{I}} - \frac{\Delta t}{\rho(T^m) c(T^m)} \cdot \underline{\underline{P}}(T^m) \right) \cdot \underline{T}^{m+1} = \underline{T}^m
\end{aligned} \tag{C.17}
$$

Finally, if $\underline{\underline{L}}(T^m) = \left(\underline{\underline{I}} - \frac{\Delta t}{\rho(T^m) c(T^m)} \cdot \underline{\underline{P}}(T^m) \right)$, the temperature distribution at the time step $m+1$ is:

$$
\underline{\underline{L}}(T^m) \cdot \underline{T}^{m+1} = \underline{T}^m \tag{C.18}
$$

The definition of the $\underline{\underline{L}}$ is therefore quite similar to the one in the previous section (case with constant properties). Boundary conditions are implemented similarly and also the state-space formulation is similar. The difference is that the coefficients of the matrix depend on the temperature, therefore the matrix inversion must be performed at each time step.

Appendix D

Derivation of the analytical solution for the 1D steady-state model

The energy balance equation 2.15 in steady state conditions can be written as:

$$\frac{\partial^2 T}{\partial x^2} = -\frac{\phi}{k} \tag{D.1}$$

which, with a reference to figure 3.9 has the general solution:

$$\begin{aligned} T(x) &= -\frac{\phi_W}{2k_W}x^2 + c_{1,W}x + c_{2,W},\ for\, 0 \leq x \leq L_W \\ T(x) &= -\frac{\phi_{CuCrZr}}{2k_{CuCrZr}}x^2 + c_{1,CuCrZr}x + c_{2,CuCrZr},\ for\, L_W \leq x \leq L_{tot} \end{aligned} \tag{D.2}$$

At this point, boundary conditions can be applied to evaluate the unknown constants. For $x = 0$ a Neumann boundary condition is applied:

$$\begin{aligned} -k_W \cdot \left.\frac{dT}{dx}\right|_{x=0} &= q_s \\ \iff c_{1,W} &= -\frac{q_s}{k_W} \end{aligned} \tag{D.3}$$

At the interface, the continuity of the thermal flux is applied:

$$k_W \cdot \frac{dT}{dx} = k_{CuCrZr} \cdot \frac{dT}{dx}$$

$$\iff k_W \left[-\frac{\phi_W}{k_w}x - \frac{q_s}{k_w}\right]_{x=L_W} = k_{CuCrZr}\left[-\frac{\phi_{CuCrZr}}{k_{CuCrZr}}(x - L_W) + c_{1,CuCrZr}\right]_{x=L_W}$$

$$c_{1,CuCrZr} = -\frac{\phi_W \cdot L_W}{k_{CuCrZr}} - \frac{q_s}{k_{CuCrZr}} \tag{D.4}$$

For $x = L_{tot}$, a Robin boundary condition is applied:

$$-k_{CuCrZr}\left.\frac{dT}{dx}\right|_{x=L_{tot}} = h \cdot (T - T_{water})$$

$$\iff -k_{CuCrZr}\left[-\frac{\phi_{CuCrZr}}{k_{CuCrZr}}(x-L_W)+c_{1,CuCrZr}\right]_{x=L_{tot}} =$$
$$= h\left(\frac{-\phi_{CuCrZr}}{2k_{CuCrZr}}(x-L_W)^2+c_{1,CuCrZr}(x-L_W)+c_{2,CuCrZr}-T_{water}\right)_{x=L_{tot}}$$

$$\iff c_{2,CuCrZr}=\frac{\phi_{CuCrZr}L_{CuCrZr}-k_{CuCrZr}c_{1,CuCrZr}}{h}+\frac{\phi_{CuCrZr}L_{CuCrZr}^2}{2k_{CuCrZr}}-c_{1,CuCrZr}L_{CuCrZr}+T_{water} \quad \text{(D.5)}$$

Finally, the continuity of the temperature is applied at the interface:

$$T_w(x=L_W)=T_{CuCrZr}(x=L_W)$$

$$\iff \left[-\frac{\phi_W}{2k_W}x^2+c_{1,W}x+c_{2,W}\right]_{x=L_W}=\left[-\frac{\phi_{CuCrZr}}{2k_{CuCrZr}}(x-L_W)^2+c_{1,CuCrZr}(x-L_W)+c_{2,CuCrZr}\right]_{x=L_W}$$

$$\iff c_{2,W}=\frac{\phi_W L_W^2}{2k_W}-c_{1,W}L_W+c_{2,CuCrZr} \quad \text{(D.6)}$$

The surface temperature is:

$$T(x=0)=c_{2,W}=\frac{\phi_W L_W^2}{2k_W}+\frac{q_s}{k_W}L_W+\frac{\phi_{CuCrZr}L_{CuCrZr}-k_{CuCrZr}\cdot\left(-\frac{\phi_W\cdot L_W}{k_{CuCrZr}}-\frac{q_s}{k_{CuCrZr}}\right)}{h}+$$
$$\frac{\phi_{CuCrZr}L_{CuCrZr}^2}{2k_{CuCrZr}}-L_{CuCrZr}\cdot\left(-\frac{\phi_W\cdot L_W}{k_{CuCrZr}}-\frac{q_s}{k_{CuCrZr}}\right)+T_{water} \quad \text{(D.7)}$$

Appendix E

ADI method

This section deals with the definition of the matrices containing the heat diffusion process in the case of an ADI method with a Crank-Nicolson discretization following the content of the paper [Tadjeran and Meerschaert, 2007]. This method is applied to a domain of unitary length characterized by an initial condition of 100 °C and boundary conditions of a constant temperature of 0 °C.

Starting with the time-dependent 2D heat diffusion equation with constant properties:

$$\rho c \frac{\partial T}{\partial t} = k \cdot \left(\frac{\partial^2 T}{\partial x^2} + \frac{\partial^2 T}{\partial y^2} \right) \tag{E.1}$$

this equation can be discretized using a Crank-Nicolson method around generic nodes i and j as follows:

$$\rho c \left(\frac{T_{i,j}^{m+1} - T_{i,j}^{m}}{\Delta t} \right) = \frac{k}{2} \left[\frac{T_{i+1,j}^{m+1} - 2T_{i,j}^{m+1} + T_{i-1,j}^{m+1}}{\Delta x^2} + \frac{T_{i+1,j}^{m} - 2T_{i,j}^{m} + T_{i-1,j}^{m}}{\Delta x^2} + \right. \tag{E.2}$$

$$\left. + \frac{T_{i,j+1}^{m+1} - 2T_{i,j}^{m+1} + T_{i,j-1}^{m+1}}{\Delta y^2} + \frac{T_{i,j+1}^{m} - 2T_{i,j}^{m} + T_{i,j-1}^{m}}{\Delta y^2} \right] \tag{E.3}$$

which can written as:

$$T_{i,j}^{m+1} - T_{i,j}^{m} = \frac{\alpha \Delta t}{2 \Delta x^2} \cdot \left[T_{i+1,j}^{m+1} - 2T_{i,j}^{m+1} + T_{i-1,j}^{m+1} + T_{i+1,j}^{m} - 2T_{i,j}^{m} + T_{i-1,j}^{m} \right] + \tag{E.4}$$

$$+ \frac{\alpha \Delta t}{2 \Delta y^2} \cdot \left[T_{i+1,j}^{m+1} - 2T_{i,j}^{m+1} + T_{i-1,j}^{m+1} + T_{i+1,j}^{m} - 2T_{i,j}^{m} + T_{i-1,j}^{m} \right] \tag{E.5}$$

By introducing the quantities $a_x = \frac{\alpha \Delta t}{2 \Delta x^2}$ and $a_y = \frac{\alpha \Delta t}{2 \Delta y^2}$, the above expression can be written as:

$$T_{i,j}^{m+1} - \frac{a_x}{2} \cdot T_{i+1,j}^{m+1} + a_x \cdot T_{i,j}^{m+1} - \frac{a_x}{2} \cdot T_{i-1,j}^{m+1} - \frac{a_y}{2} \cdot T_{i,j+1}^{m+1} + a_y \cdot T_{i,j}^{m+1} - \frac{a_y}{2} \cdot T_{i,j-1}^{m+1} = \tag{E.6}$$

$$T_{i,j}^{m} + \frac{a_x}{2} \cdot T_{i+1,j}^{m} - a_x \cdot T_{i,j}^{m} + \frac{a_x}{2} \cdot T_{i-1,j}^{m} + \frac{a_y}{2} \cdot T_{i,j+1}^{m} - a_y \cdot T_{i,j}^{m} + \frac{a_y}{2} \cdot T_{i,j-1}^{m} \tag{E.7}$$

The above expression can be written in a compact way by using the operators δ_x and δ_y, whose definitions are $\delta_x T_{i,j}^{m+1} = T_{i+1,j}^{m+1} - 2T_{i,j}^{m+1} + T_{i-1,j}^{m+1}$ and $\delta_y T_{i,j}^{m+1} = T_{i,j+1}^{m+1} - 2T_{i,j}^{m+1} + T_{i,j-1}^{m+1}$ respectively as follows:

$$T_{i,j}^{m+1} \cdot \left(1 - \frac{a_x}{2} \delta_x - \frac{a_y}{2} \delta_y \right) = T_{i,j}^{m} \cdot \left(1 + \frac{a_x}{2} \delta_x + \frac{a_y}{2} \delta_y \right) \tag{E.8}$$

It is worthwhile to underline that, up to this point, the scheme is exact. The following step is applying a Peaceman-Rachford decomposition, which introduces a simplification in the scheme by defining the intermediate quantity $T_{i,j}^{*}$. In particular:

$$\begin{cases} \left(1 - \frac{a_x}{2}\delta_x\right) \cdot T^*_{i,j} = \left(1 + \frac{a_y}{2}\delta_y\right) \cdot T^m_{i,j} \\ \left(1 - \frac{a_y}{2}\delta_y\right) \cdot T^{m+1}_{i,j} = \left(1 + \frac{a_x}{2}\delta_x\right) \cdot T^*_{i,j} \end{cases} \tag{E.9}$$

The above system of equations, when extended to all the nodes i, j belonging to a domain, can be written in matrix form. Indeed:

$$\left(1 - \frac{a_x}{2}\delta_x\right) \cdot T^*_{i,j} = -\frac{a_x}{2}T^*_{i+1,j} + (1 + a_x)T^*_{i,j} - \frac{a_x}{2}T^*_{i-1,j} \rightarrow \underline{\underline{A_x}} \cdot T^*, \ for\ i = 1, ..., N \tag{E.10}$$

where $\underline{\underline{A_x}}$ is a tridiagonal matrix whose non-zero diagonals are the main, the upper, and the lower ones. Similarly:

$$\left(1 + \frac{a_y}{2}\delta_y\right) \cdot T^m_{i,j} = \frac{a_y}{2}T^m_{i,j+1} + (1 - a_y)T^m_{i,j} + \frac{a_y}{2}T^m_{i,j-1} \rightarrow \underline{\underline{A_y}} \cdot T^m, \ for\ j = 1, ..., N \tag{E.11}$$

where $\underline{\underline{A_y}}$ is a block-tridiagonal matrix whose non-zero diagonals are the main, the upper N, and the lower N ones. Therefore, equation E.9 can be written as:

$$\begin{cases} T^* = \underline{\underline{A_x^{-1}}} \cdot \left(\underline{\underline{A_y}} \cdot T^m\right) \\ T^{m+1} = \underline{\underline{B_y^{-1}}} \cdot \left(\underline{\underline{B_x}} \cdot T^*\right) \end{cases} \tag{E.12}$$

with $\underline{\underline{B_x}} = 2\underline{\underline{I}} - \underline{\underline{A_x}}$ and $\underline{\underline{B_y}} = 2\underline{\underline{I}} - \underline{\underline{A_y}}$ with $\underline{\underline{I}}$ being the identity matrix. Basically, the solution T^{m+1} is found following a two-step process, in which an intermediate temperature distribution T^* is evaluated by solving the diffusion along x only, and then the T^{m+1} is evaluated by solving the diffusion along y.

Concerning the boundary conditions, for the intermediate temperature distribution T^* it is necessary to apply the following consistency condition:

$$2T^*_{i,j} = \left(1 - \frac{a_y}{2}\delta_y\right) \cdot T^{m+1}_{i,j} + \left(1 + \frac{a_y}{2}\delta_y\right) \cdot T^m_{i,j} \tag{E.13}$$

which corresponds to set $T^*_{i,j} = 0$ on all the nodes belonging to the boundary, as $T^{m+1}_{i,j} = T^m_{i,j} = 0$ on the boundaries as well. Therefore, it is sufficient to impose homogeneous Dirichlet boundary conditions both on $\underline{\underline{A_x}}$ and $\underline{\underline{B_y}}$.

References

[Alla, 2022] Alla, A. (2022). First steps into model order reduction.

[Anand et al., 2021] Anand, H., Eldon, D., Humphreys, D., Lasnier, C., Stangeby, P., Barr, J., and Sammuli, B. (2021). Model-based real-time surface heat flux and temperature estimation for the diii-d tokamak. *Nuclear Fusion*, 61(3):036012.

[Anderson and Wendt, 1995] Anderson, J. D. and Wendt, J. (1995). *Computational fluid dynamics*, volume 206. Springer.

[Arnoux et al., 2013] Arnoux, G., Farley, T., Silva, C., Devaux, S., Firdaouss, M., Frigione, D., Goldston, R. J., Gunn, J., Horacek, J., Jachmich, S., et al. (2013). Scrape-off layer properties of iter-like limiter start-up plasmas in jet. *Nuclear Fusion*, 53(7):073016.

[Aumeunier et al., 2017] Aumeunier, M.-H., Kočan, M., Reichle, R., and Gauthier, E. (2017). Impact of reflections on the divertor and first wall temperature measurements from the iter infrared imaging system. *Nuclear Materials and Energy*, 12:1265–1269.

[Bergman et al., 2011] Bergman, T. L., Lavine, A. S., Incropera, F. P., and DeWitt, D. P. (2011). *Introduction to heat transfer*. John Wiley & Sons.

[Bhikkaji and Söderström, 2001] Bhikkaji, B. and Söderström, T. (2001). Reduced order models for diffusion systems using singular perturbations. *Energy and buildings*, 33(8):769–781.

[Brank, 2024] Brank, M. (2024). *Physics and engineering studies of heat fluxes to ITER plasma-facing components (submitted)*. PhD thesis, University of Ljubljana.

[Brank et al., 2019] Brank, M., Kos, L., Pitts, R. A., and Simic, G. (2019). Thermal modelling of iter first wall. *International Conference Nuclear Energy for New Europe*.

[Capellán-Pérez et al., 2017] Capellán-Pérez, I., De Castro, C., and Arto, I. (2017). Assessing vulnerabilities and limits in the transition to renewable energies: Land requirements under 100% solar energy scenarios. *Renewable and Sustainable Energy Reviews*, 77:760–782.

[Çengel and Ghajar, 2020] Çengel, Y. A. and Ghajar, A. J. (2020). *Heat and Mass Transfer: Fundamentals [and] Applications*. McGraw-Hill Education.

[Creely et al., 2020] Creely, A., Greenwald, M. J., Ballinger, S. B., Brunner, D., Canik, J., Doody, J., Fülöp, T., Garnier, D., Granetz, R., Gray, T., et al. (2020). Overview of the sparc tokamak. *Journal of Plasma Physics*, 86(5):865860502.

[De Vicente et al., 2022] De Vicente, S. M. G., Smith, N. A., El-Guebaly, L., Ciattaglia, S., Di Pace, L., Gilbert, M., Mandoki, R., Rosanvallon, S., Someya, Y., Tobita, K., et al. (2022). Overview on the management of radioactive waste from fusion facilities: Iter, demonstration machines and power plants. *Nuclear Fusion*, 62(8):085001.

[Deliege, 2024] Deliege, Q. (2024). Thermal analysis of temporary first wall (tfw) design v20 with transient loading. In *ITER Organization, Internal communication*.

[Dziejarski et al., 2023] Dziejarski, B., Krzyżyńska, R., and Andersson, K. (2023). Current status of carbon capture, utilization, and storage technologies in the global economy: A survey of technical assessment. *Fuel*, 342:127776.

[European Commission, n.d.] European Commission (n.d.). Consequences of climate change. `https://climate.ec.europa.eu/climate-change/consequences-climate-change_en`. Visited on 28-12-2023.

[Federici et al., 2019] Federici, G., Siccinio, M., and Kembleton, R. (2019). Overview of the demo design-staged approach in europe. *Fusion Engineering and Design, vol. to be published in*.

[Freidberg, 2008] Freidberg, J. P. (2008). *Plasma physics and fusion energy*. Cambridge university press.

[Gerardin et al., 2016] Gerardin, J., Aumeunier, M., Firdaouss, M., Gardarein, J., and Rigollet, F. (2016). Investigation on reduced thermal models for simulating infrared images in fusion devices. In *Journal of Physics: Conference Series*, volume 745, page 032019. IOP Publishing.

[Hirsch, 1988] Hirsch, C. (1988). *Numerical computation of internal & external flows: fundamentals of numerical discretization*. John Wiley & Sons, Inc.

[Hristov, 2023] Hristov, J. (2023). Transient heat conduction with variable thermophysical properties power-law temperature-depenent heat capacity and thermal conductivity. *Thermal Science*, 27(Spec. issue 1):411–422.

[Hunt, 2023] Hunt, R. (2023). Status of the iter first wall. In *ITPA Coordination Committee, Internal Communication*.

[IEA, n.d.a] IEA (n.d.a). Carbon capture, utilisation and storage. `https://www.iea.org/energy-system/carbon-capture-utilisation-and-storage`. Visited on 04-01-2024.

[IEA, n.d.b] IEA (n.d.b). Energy security. `https://www.iea.org/topics/energy-security`. Visited on 29-12-2023.

[IEA, n.d.c] IEA (n.d.c). Nuclear power. `https://www.iea.org/energy-system/electricity/nuclear-power`. Visited on 04-01-2024.

[ITER, 2007] ITER (2007). Nuclear analysis report. *ITER IDM internal document*.

[ITER, 2013] ITER (2013). Appendix a: Materials design limit data. *ITER IDM internal document*.

[ITER Computing Cluster, n.d.] ITER Computing Cluster (n.d.). Iter. `https://confluence.iter.org/display/IMP/ITER+Computing+Cluster`. Visited on 30-01-2024.

[ITER Organization, n.d.a] ITER Organization (n.d.a). Advantages of fusion. `https://www.iter.org/sci/Fusion`. Visited on 29-12-2023.

[ITER Organization, n.d.b] ITER Organization (n.d.b). Iter. `https://www.iter.org/`. Visited on 08-01-2024.

[ITER Organization, n.d.c] ITER Organization (n.d.c). What is iter. `https://www.iter.org/proj/inafewlines#1`. Visited on 05-01-2024.

[Kachanov, 1959] Kachanov, L. M. (1959). Variational methods of solution of plasticity problems. *Journal of applied mathematics and mechanics*, 23(3):880–883.

[Kembleton, 2023] Kembleton, R. (2023). Technological features of a commercial fusion power plant, and the gap from demo. *Fusion Eng. Des*, 190:113544.

[Kocan et al., 2015] Kocan, M., Pitts, R., Arnoux, G., Balboa, I., De Vries, P., Dejarnac, R., Furno, I., Goldston, R. J., Gribov, Y., Horacek, J., et al. (2015). Impact of a narrow limiter sol heat flux channel on the iter first wall panel shaping. *Nuclear Fusion*, 55(3):033019.

[Kos et al., 2019] Kos, L., Pitts, R., Simič, G., Brank, M., Anand, H., and Arter, W. (2019). Smiter: A field-line tracing environment for iter. *Fusion Engineering and Design*, 146:1796–1800.

[Kumar, 2021] Kumar, N. (2021). *Analysis of turbulent transport in the central part of high-confinement tokamak plasmas*. PhD thesis, Aix-Marseille.

[Lawson, 1957] Lawson, J. D. (1957). Some criteria for a power producing thermonuclear reactor. *Proceedings of the physical society. Section B*, 70(1):6.

[Lee and Saw, 2011] Lee, S. and Saw, S. H. (2011). Nuclear fusion energy—mankind's giant step forward. *Journal of fusion energy*, 30(5):398–403.

[Lerede et al., 2023] Lerede, D., Nicoli, M., Savoldi, L., and Trotta, A. (2023). Analysis of the possible contribution of different nuclear fusion technologies to the global energy transition. *Energy Strategy Reviews*, 49:101144.

[Li et al., 2019] Li, L., Liu, Y., Loarte, A., Pinches, S., Polevoi, A., and Zhong, F. (2019). Toroidal modeling of resonant magnetic perturbations in preparation for the initial phase of iter operation. *Nuclear Fusion*, 60(1):016013.

[Litnovsky et al., 2009] Litnovsky, A., Wienhold, P., Philipps, V., Krieger, K., Kirschner, A., Matveev, D., Borodin, D., Sergienko, G., Schmitz, O., Kreter, A., et al. (2009). Investigations of castellated structures for iter: The effect of castellation shaping and alignment on fuel retention and impurity deposition in gaps. *Journal of nuclear materials*, 390:556–559.

[Loarte A., 2023] Loarte A. (2023). Stac reviews new proposals for the construction and operation phases. `https://www.iter.org/fr/actualites/3935`. Visited on 08-01-2024.

[Maurizio, 2020] Maurizio, R. (2020). Investigating scrape-off layer transport in alternative divertor geometries on the tcv tokamak. Technical report, EPFL.

[Mazul et al., 2012] Mazul, I., Alekseev, A., Belyakov, V., Bondarchuk, D., Eaton, R., Escourbiac, F., Gervash, A., Glazunov, D., Kuznetsov, V., Merola, M., et al. (2012). Russian development of enhanced heat flux technologies for iter first wall. *Fusion Engineering and Design*, 87(5-6):437–442.

[Merola et al., 2010] Merola, M., Loesser, D., Martin, A., Chappuis, P., Mitteau, R., Komarov, V., Pitts, R., Gicquel, S., Barabash, V., Giancarli, L., et al. (2010). Iter plasma-facing components. *Fusion Engineering and Design*, 85(10-12):2312–2322.

[Meschini et al., 2023] Meschini, S., Laviano, F., Ledda, F., Pettinari, D., Testoni, R., Torsello, D., and Panella, B. (2023). Review of commercial nuclear fusion projects. *Frontiers in Energy Research*, 11:1157394.

[Mitteau et al., 2013] Mitteau, R., Calcagno, B., Chappuis, P., Eaton, R., Gicquel, S., Chen, J., Labusov, A., Martin, A., Merola, M., Raffray, R., et al. (2013). The design of the iter first wall panels. *Fusion Engineering and Design*, 88(6-8):568–570.

[Mitteau et al., 2017] Mitteau, R., Eaton, R., Gervash, A., Kuznetcov, V., Davydov, V., and Rulev, R. (2017). Allowable heat load on the edge of the iter first wall panel beryllium flat tiles. *Nuclear Materials and Energy*, 12:1067–1070.

[Mitteau et al., 2010] Mitteau, R., Stangeby, P., Lowry, C., Merola, M., et al. (2010). Heat loads and shape design of the iter first wall. *Fusion Engineering and design*, 85(10-12):2049–2053.

[Moran et al., 2010] Moran, M. J., Shapiro, H. N., Boettner, D. D., and Bailey, M. B. (2010). *Fundamentals of engineering thermodynamics*. John Wiley & Sons.

[Munson et al., 2013] Munson, B. R., Okiishi, T. H., Huebsch, W. W., and Rothmayer, A. P. (2013). *Fluid mechanics*. Wiley Singapore.

[National Nuclear Data Center, 2024] National Nuclear Data Center (2024). Neutrons scattering. `https://www.nndc.bnl.gov/`. Visited on 07-02-2024.

[Ongena, 2016] Ongena, J. (2016). Nuclear fusion and its large potential for the future world energy supply. *Nukleonika*, 61(4):425–432.

[Perez-Pichel et al., 2017] Perez-Pichel, G., Porton, M., Kirk, S., Vizvary, Z., and Eaton, G. (2017). Analysis of a tile repair technique based on brazing process for iter first wall. *Fusion Engineering and Design*, 122:186–195.

[Pesamosca, 2023] Pesamosca, F. (2023). Development of a control-oriented model for iter first wall protection. In *ITER Organization, Internal Communication*.

[Pesamosca et al., 2023] Pesamosca, F., Ravensbergen, T., Pitts, R., Vries, P. d., Zabeo, L., Pangione, L., Carvalho, I., Aumeunier, M.-H., and Brank, M. (2023). First wall heat load control design for iter with a model-based approach. In *30th IEEE Symposium on Fusion Engineering (SOFE)*.

[Pironti and Walker, 2005] Pironti, A. and Walker, M. (2005). Control of tokamak plasmas: introduction to a special section. *IEEE Control Systems Magazine*, 25(5):24–29.

[Pitts, 2019] Pitts, R. (2019). 10th iter international school, kaist, daejeon, south korea. In *ITER Organization*.

[Pitts et al., 2011] Pitts, R., Carpentier, S., Escourbiac, F., Hirai, T., Komarov, V., Kukushkin, A., Lisgo, S., Loarte, A., Merola, M., Mitteau, R., et al. (2011). Physics basis and design of the iter plasma-facing components. *Journal of Nuclear Materials*, 415(1):S957–S964.

[Pitts R., 2024] Pitts R. (2024). Joint iter-east experiments - a wealth of data harvested. `https://www.iter.org/newsline/-/3990?utm_campaign=whatsnew_weekly&utm_medium=email&utm_source=05%20Feb%202024&utm_content=featured`. Visited on 07-02-2024.

[Raffray and Federici, 1997] Raffray, A. R. and Federici, G. (1997). Raclette: a model for evaluating the thermal response of plasma facing components to slow high power plasma transients. part i: Theory and description of model capabilities. *Journal of Nuclear Materials*, 244(2):85–100.

[Ravensbergen et al., 2021] Ravensbergen, T., van Berkel, M., Perek, A., Galperti, C., Duval, B., Février, O., van Kampen, R., Felici, F., Lammers, J., Theiler, C., et al. (2021). Real-time feedback control of the impurity emission front in tokamak divertor plasmas. *Nature communications*, 12(1):1105.

[Ravensbergen et al., 2023] Ravensbergen, T., Zabeo, L., de Vries, P., Pangione, L., Treutterer, W., De Tommasi, G., Lee, W.-r., Tak, T., and Zagar, A. (2023). Strategy towards model-based design and testing of the iter plasma control system. *Fusion Engineering and Design*, 188:113440.

[Ritchie et al., 2020] Ritchie, H., Rosado, P., and Roser, M. (2020). Energy production and consumption. *Our World in Data*. https://ourworldindata.org/energy-production-consumption.

[Sahu and Behera, 2012] Sahu, S. K. and Behera, P. (2012). An improved lumped analysis for transient heat conduction in different geometries with heat generation. *Comptes Rendus Mécanique*, 340(7):477–484.

[Schleisner et al., 2001] Schleisner, L., Hamacher, T., Cabal, H., Hallberg, B., Lechón, Y., Korhonen, R., and Sáez, R. (2001). Energy, material and land requirement of a fusion plant. *Fusion engineering and design*, 58:1081–1085.

[Shimada et al., 2007] Shimada, M., Campbell, D., Mukhovatov, V., Fujiwara, M., Kirneva, N., Lackner, K., Nagami, M., Pustovitov, V., Uckan, N., Wesley, J., et al. (2007). Overview and summary. *Nuclear Fusion*, 47(6):S1.

[Skopec et al., 2021] Skopec, P., Vyhlidal, T., and Knobloch, J. (2021). Reduced model of boundary value dynamics of 1d diffusion-application to heat conduction. In *2021 23rd International Conference on Process Control (PC)*, pages 90–95. IEEE.

[Stangeby et al., 2000] Stangeby, P. C. et al. (2000). *The plasma boundary of magnetic fusion devices*, volume 224. Institute of Physics Pub. Philadelphia, Pennsylvania.

[Tadjeran and Meerschaert, 2007] Tadjeran, C. and Meerschaert, M. M. (2007). A second-order accurate numerical method for the two-dimensional fractional diffusion equation. *Journal of Computational Physics*, 220(2):813–823.

[United Nations, n.d.] United Nations (n.d.). Causes and effects of climate change. `https://www.un.org/en/climatechange/science/causes-effects-climate-change`. Visited on 28-12-2023.

[Valcárcel et al., 2014] Valcárcel, D., Alves, D., Card, P., Carvalho, B., Devaux, S., Felton, R., Goodyear, A., Lomas, P., Maviglia, F., McCullen, P., et al. (2014). The jet real-time plasma-wall load monitoring system. *Fusion Engineering and Design*, 89(3):243–258.

[von Winckel G., 2024] von Winckel G. (2024). Block tridiagonal solver, matlab central file exchange. `https://www.mathworks.com/matlabcentral/fileexchange/4695-block-tridiagonal-solver`. Visited on 07-02-2024.

[Walker et al., 2015] Walker, M., Ambrosino, G., De Tommasi, G., Humphreys, D., Mattei, M., Neu, G., Rapson, C., Raupp, G., Treutterer, W., Welander, A., et al. (2015). The iter plasma control system simulation platform. *Fusion Engineering and Design*, 96:716–719.

[Wikipedia, n.d.] Wikipedia (n.d.). Nuclear binding energy. `https://en.wikipedia.org/wiki/Nuclear_binding_energy`. Visited on 05-01-2024.

[Wurzel and Hsu, 2022] Wurzel, S. E. and Hsu, S. C. (2022). Progress toward fusion energy breakeven and gain as measured against the lawson criterion. *Physics of Plasmas*, 29(6).

[Zhang et al., 2011] Zhang, P., Zhao, J., Qin, Y., and Wen, B. (2011). Numerical simulation of the combined effects of plasma heating and neutron heating loads on the iter first wall. *Fusion engineering and design*, 86(1):45–50.